LIPID AND PROTEIN ORGANIZATIONS IN MODEL MEMBRANE SYSTEMS- MEMBRANE CURVATURE, LIPID STRUCTURE, DOMAIN FORMATION, AND MEMBRANE BINDING KINETICS

Wan-Ting Hsieh

A DISSERTATION

in

Chemistry

Presented to the Faculties of the University of Pennsylvania

in Partial Fulfillment of the Requirements for the Degree of Doctor of Philosophy

2013

_____

Dr. Tobias Baumgart, Associate Professor of Chemistry

Supervisor of Dissertation

_____

Dr. Gary A. Molander, Professor of Chemistry

Graduate Group Chairperson

Dissertation Committee

Dr. Feng Gai, Professor of Chemistry

Dr. Jeffery Saven, Associate Professor of Chemistry

Dr. Paul Janmey, Professor of Physiology and Bioengineering

ACKNOWLEDGEMENT

First of all, I would like to thank my dissertation advisor Professor Tobias Baumgart. I appreciate his giving me the opportunities in working with many interesting projects. He is always available for discussions and willing to help. His thorough and critical thinking and inspiring creativity have brought me to learn how solid science develops. He also encouraged me to have a big picture in designing and directing projects.

I am grateful for the time and guidance from Professors Feng Gai, Jeffery Saven, and Paul Janmey. As my thesis committee members, they evaluated my work such that it could move along and stand up to scrutiny. I also thank for their advices in polishing my presentation skills.

My research projects got a lot of help from other coworkers. Dr. Daniel Chinnapen and Professor Wayne Lencer at Boston Children's Hospital guided me in ganglioside/cholera toxin project and showed me the beauty of biology. Professor Shu Yang and her talented graduate student, Chi-Mon Chen, at Material Science and Engineering Department at Penn helped me a lot in the wavy membrane project. The collaboration with them brought me to appreciate how material science comes into play in solving biological problems. Professor Ivan Dmochowski and his intelligent graduate student, Zhengzheng Liao, greatly facilitated my research projects in the last two years. I really enjoyed those discussions and brainstorms with them!

Particularly, I would like to thank all the former and current labmates. It has been my pleasure to work with these smart, nice, and diligent scientists. Drs. Aiwei Tian and Cinzia Esposito instructed me in working with GUVs. Dr. Mike Heinrich trained me in monolayer systems and exposed me how Matlab coding facilitates data analysis. Dr. Chih-Jung Hsu worked with me in the wavy membranes project and provided me important training and advices in the lab. Dr. Ben Capraro improved my biochemistry knowledge and instructed me in mutagenesis and protein purifications. I also appreciated the enjoyable and fruitful interactions with Zheng Shi, Tingting Wu, Dr. Sanghamitra Deb, Ningwei Li, Chen Zhu, Zhiming Chen, and Dr. Katarzyna Jankowska, who were awesome colleagues and generous with their help and time for me.

For some personal acknowledgments, I would like to thank all the great friends I have made during my graduate career at Penn. Without naming anyone in particular due to the limited space, I sincerely thank them for making my research life joyful and those enjoyable moments with them have become priceless memories in my life.

Finally, many thanks go to Yu-Hsiu Wang, who is always around and shares the happiness and sadness with me. I also thank him for encouragement at my self-doubt.

Most importantly, I want to show my deepest gratitude to my parents and brothers for their love, guidance, and encouragement. Without the supports from my family, I would have never made to this end.

ABSTRACT

LIPID AND PROTEIN ORGANIZATIONS IN MODEL MEMBRANE SYSTEMS-MEMBRANE CURVATURE, LIPID STRUCTURE, DOMAIN FORMATION AND MEMBRANE BINDING KINETICS

Wan-Ting Hsieh

Dr. Tobias Baumgart

The composition and morphology of cellular membranes are highly dynamic. Potential parameters modulating protein and lipid distributions in different organelles include membrane shapes and the structures of lipids and proteins. Moreover, the concept of "lipid rafts" provides a prevailing view where nanodomains serve as centers for signal transduction, membrane trafficking, and cytoskeletal organization. In this contribution, we first investigated the lipid and protein organizations as a function of membrane curvature. To this end, a system consisting of solid-supported wavy membranes that exhibits a continuous curvature distribution with positive and negative curvature ranges was fabricated. Spatial distributions of ENTH (epsin N-terminal homology) domain and N-BAR (Bin-Amphiphysin-Rvs) domains derived from the proteins Endophilin and BIN-1 were found to vary approximately linearly with membrane curvature. In contrast, streptavidin and fluorescent lipid analogues exhibited homogenous distributions on wavy

membranes. Fluorescence recovery after photobleaching and single-molecule tracking experiments revealed that protein domains remain laterally fluid in the curved regions. We next studied the membrane organization with respect to lipid structures, more specifically, the length and degree of saturation of acyl chains of lipids. The ganglioside GM1 binds cholera toxin (CT) on host cells and carries it retrograde from the plasma membrane (PM) through endosomes, the trans-Golgi network (TGN), and the endoplasmic reticulum (ER) to induce toxicity. To elucidate how a membrane lipid can specify trafficking in these pathways, GM1 isoforms with alternate ceramide domains were synthesized and their partitioning between liquid-ordered (Lo) and liquid-disordered (Ld) phases in GUVs was imaged. GM1 with differing ceramides showed distinct phase-partitioning behaviors. Furthermore, crosslinking of GM1 by cholera toxin subunit B (CTB) was found to drive phase partitioning shift from less preferential phase preference to exclusively Ld or Lo phases. To shed light on the stability of lipid domains, factors qwhich affect line tension were discussed and potential line-active molecules were examined. We found that the presence of cone-shaped diacylglycerol decreases line tension, while the commonly used fluorescent lipid, Texas-Red DHPE tends to increase line tension. Additionally, to bridge the connection between thermodynamics to highly dynamic cellular environments, we developed a single liposome-based kinetics system which allowed us to examine membrane binding kinetics of proteins as a function of membrane curvature. Overall, these measurements help provide an integrated view of

biophysical and structural parameters underlying organizations of lipids and proteins.

TABLE OF CONTENTS

LIST OF FIGURES

CHAPTER 1: Background and Significance

1.1 Curvature Sorting of Peripheral Proteins on Wavy Membranes[a]

Active deformation of cell membranes is an important aspect of their functions. Transitions between different shapes have been postulated to be accompanied by and controlled through the sorting of phospholipids and membrane proteins[1]. Growing support for this notion has been contributed by research on the membrane curvature sensing and generation[2,3] of a myriad of peripheral membrane proteins[4–7]. The malfunctions of curvature-sensing proteins have been implicated in defective cellular functions and diseases[8–11].

For example, the protein Epsin is believed to be involved in clathrin-mediated endocytosis[12], and the distribution of ENTH (Epsin N-terminal homology) domains on membranes has been found to be sensitive to membrane curvature[13]. Furthermore, N-terminal helix containing BIN-Amphiphysin-Rvs (N-BAR) domains, forming crescent-shaped dimers[4,6] consisting of α-helical bundles, have been shown to preferentially

---

[a] Parts of this chapter are reproduced by previously published work: Hsieh, W.-T., Hsu C.-J., Capraro B. R., Wu T., Chen C.-M., Yang S., Baumgart T. (2012). Curvature Sorting of Protein Domains on Solid-Supported Wavy Membranes. *Langmuir*, 28 (35), 12838–12843.

localize on positively curved membranes[14,15]. Electron microscopy (EM) studies have furthermore demonstrated that these proteins can tubulate liposomes[4,16–18].

In addition to positive curvature sensitivity, recent studies have demonstrated the localization of cell divisions protein DivIVA in the negatively curved intracellular leaflets of the poles of Bacillus subtilis cells[19,20]. Furthermore, bacterial toxins, including cholera toxin and Shiga toxin, were reported to induce inward membrane invaginations[21,22] and to segregate away from positive curvature regions in vitro[23,24].

To investigate the mechanisms of membrane curvature sensing and generation, a variety of experimental approaches have been established, including a recently developed biochemical vesiculation assay[25], the single liposome curvature (SLiC) assay[14], and a membrane tether system where cylindrically shaped membranes are pulled from pipette-aspirated giant unilamellar vesicles (GUVs)[26,27]. Shortcomings of all of these systems are that only positively curved outer leaflets can be accessed with ease, these techniques tend to be time consuming and technically challenging, and some of them suffer from low signal-to-noise ratios.

In order to overcome these challenges, we engineered a solid-supported wavy membrane to quantitatively investigate the distribution of several peripheral membrane proteins in a spatially varying membrane curvature field. Two-dimensional solid-supported curved membranes have previously been fabricated on

polydimethylsiloxane[28,29] and quartz surfaces[30] to examine the spatial distributions of liquid ordered and disordered lipid phases. In Chapter 3, we used a related approach to demonstrate that an engineered wavy platform with continuous curvatures bearing positive and negative regions allows evaluation of the curvature sensitivities of a variety of proteins. We compare findings for this wavy surface to the more established tether/ GUV protein sorting system.

1.2 Lipid Sorting by Ceramide Structure for the Cholera Toxin Receptor Ganglioside GM1[b]

Cholera toxin (CT) is a protein secreted by the bacterium *Vibrio cholera* and is responsible for diarrhea in disease cholera[31]. Typifying AB_5-subunit toxin, CT consists of monomeric A subunit and pentameric B subunit. The entry of CT into cells is initiated from binding to plasma membrane by associating with its binding partner, ganglioside GM1, whose structure includes oligosaccharide that binds to CT and ceramide domain that anchors to membrane. The CT-GM1 complex is then transported from plasma membrane (PM), endosomes, to *trans*-Golgi and end in endoplasmic reticulum (ER), in

[b] Parts of this chapter are reproduced from previously published work: Chinnapen, D. J.-F., Hsieh, W.-T., te Welscher, Y. M., Saslowsky, D. E., Kaoutzani, L., Brandsma, E., D'Auria, L., Park, H., Wagner, J. S., Drake, K.R., Kang, M., Benjamin, T., Ullman, M. D., Costello, C.E., Kenworthy, A.K., Baumgart, T., Massol, R.H., Lencer, W. I. (2012) A native lipid-sorting pathway from PM to ER for the unsaturated species of ganglioside GM1. *Developmental Cell*, 23 (3), 573-586.

which CT hijacks the endogenous pathway, ultimately causing imbalance in electrolytes movement in epithelial cells and water secretion.

How CT-GM1 complex sorting in different organelles occurs remains unclear. Previous studies in human intestinal T84 cells[32,33] revealed that not all gangliosides associating with AB_5 toxins travel from PM to ER. It was also found that the predominant GM1 species in T84 cells have ceramide chains with C24:1, C24:0, C16:1, C16:0 fatty acids[34]. This finding implied that sorting pathway might be dictated by the structures of ceramide GM1. Two main mechanisms have been proposed to explain the lipid sorting in mammalian cells. One of them suggests it is the overall lipid structure that drives the partitioning by minimize the free energy in occupying in the membrane bilayer[35]. With respect to the structure of GM1, this mechanism implies that GM1 with kinked unsaturated structures would favor the curved membranes, e.g. sorting tubules and ER, while GM1 with long saturated chains would prefer the flat membranes and remain in the endosomes. The other mechanism states that the sorting process is cooperative, involving the self-assembly of certain lipids into domains based on phase behavior and/or subsequent interactions with other membrane components[26,27].

In Chapter 4, we tested the hypothesis that the ceramide structure of the GM1 dictates the lipid fate in the trafficking pathway. To this end, GM1 species with the same oligosaccharides head group but different chain length and degree of saturation were synthesized. We examined the partitioning of various GM1 derivatives in coexisting

liquid ordered (Lo) and liquid disordered phases in GUVs. Together with the results in GM1 trafficking in vivo, the sorting mechanism in mammalian cells was inferred[34].

1.3 Examining the Mechanisms of Curvature Sensing of N-BAR Domains Using a Single Liposome-Based Kinetic Technique

Clathrin-mediated endocytosis (CME) is a highly dynamic process in which proteins are recruited to the clathrin coated pit (CCP) at different time points to accomplish the entire process[36,37]. Among the proteins involved in CME, BAR domain-containing proteins, e.g. amphiphysin and endophilin, have been found to be able to generate and sense membrane curvature. To understand membrane binding mechanism and bridge between thermodynamics to highly dynamic cellular environments call for studies exploring kinetics aspects of membrane binding [38].

The membrane curvature sensing and generation of endophilin N-BAR domains have been well studied[4,16,39–41]. Motivated by results at equilibrium, we are interested in examining the role of curvatures in membrane binding processes. In order to evaluate membrane binding kinetics with respect to curvatures, in Chapter 4, we combined a flow-based system and recently developed tethered vesicle assay by Stamou et al[14]. We fabricated a microfluidic chamber requiring only 300 nL of proteins. Our system allowed programmable injections of proteins and vesicles. With this approach, we can follow membrane binding kinetics of proteins on single liposomes. Furthermore, membrane

curvature information can be obtained from an analysis of fluorescence from lipid vesicles.

1.4 Line Tension of Domains in Model Biomembrane Systems

Cell membranes provide protection and compartmentation for organelles to execute normal cellular functions. Moreover, the membranes are composed of a variety of phospholipids, as contributes to the membrane heterogeneity[42]. This heterogeneity has received significant interests due to its potential coupling to mechanical function, such as curvature sorting of protein[1], and also involvement in signaling and trafficking[43]. In particular, "lipid raft" hypothesis[44] has stimulated in-depth studies in lateral phase separation in multi-component membranes. Microscopically visible fluid phase coexistence was first demonstrated in artificial lipid bilayers[45,46] and monolayers[47]. The detergent resistant domains from in vivo studies have also provided the evidence for membrane domains. Further, giant plasma membrane vesicle (GPMV) studies from mammalian cells have suggested the protein partitioning between coexisting Lo-like and Ld-like phases[48,49].

Line tension, interfacial tension along the phase boundary, controls membrane fission, budding and also regulates domain size[50–52]. Better understanding and quantification on line tension will shed light on how biomembranes function in vivo. For this purpose, Esposito et al. developed flicker spectroscopy method to study the domain

fluctuations on giant unilamellar vesicles[53] (GUVs). Heinrich et al. further applied this approach and acquired line tension and dipole density difference between fluid phases in Langmuir lipid monolayers[54].

In Chapter 6, we compared line tension and dipole density acquired based on theories by Goldstein and Jackson[55], and Lee and McConnell[56]. We further investigated the photo-effect on line tension in different lipid compositions in GUVs. To enable better control of line tension, factors affecting line tension were reviewed and potential line-active lipids were examined. Chapter 6 revealed that the presence of cone-shaped diacylglycerol decreased line tension, while the commonly used fluorescent lipid, Texas-Red DHPE tended to increase line tension.

1.5 Interactions between Silicone Oil and IgG at Air-Water Interfaces

Poly(dimethysiloxane) (PDMS) has been widely used in lubricants due to its distinctive viscoelasticity, optical clarity, and low water-solubility. These properties also favor PDMS in creating microfluidic devices for demanding biotechnological and industrial applications[57]. For example, PDMS elastomer has been used in fabricating microfluidics for cell culture systems in drug discovery. Related silicone materials find increasing use in medical applications as bioengineered fluids, implant materials and drug delivery vehicles. Silicone oil (SO), which is mostly composed of linear PDMS, has been used as a temporary vitreous substitute in retinal detachment[58]. However, it was

discovered recently that contact with silicone materials inhibited human corneal endothelial cell and mouse mammary fibroblast cell proliferation[59,60], thus raising questions about biocompatibility. Moreover, silicone oil was found to induce aggregation of proteins in aqueous solution. This focuses attention on silicone oil used in pharmaceutical devices such as preloaded syringes for insulin or antibody drugs[61–63]. In Chapter 7, we investigated the interaction of a model protein with silicone oil at the common air-water interface.

CHAPTER 2: Experimental Systems and Methods

2.1 Surface and Chamber Fabrication

2.1.2 Wavy glass surface fabrication[c]

An SU8 2 (MicroChem, Newton, MA, diluted to 50 wt% with gamma-Butyrolactone) thin film on a clean glass substrate was fabricated via spin coating at 3000 rpm for 30 s. The cover slip was then baked at 65 ˚C for 1 min and at 95 ˚C for another 1 min (soft bake). Subsequently, a PDMS mold with the desired spatial features[64] was imprinted onto the cover slip using capillary force lithography[64,65]. The substrate was illuminated with UV (97435 Oriel flood exposure source with 6285 Newport 500W mercury lamp) at 100 mJ/cm2, followed by post exposure bake (PEB) at 65 ˚C for 1 min and 95 ˚C for another 1 min. Next, the substrate was heated at 200 ˚C for 30 min (hard bake). It was then etched with a CF_4 and O_2 gas plasma (Trion Technology, Clearwater, FL) until the glass surface was partially exposed (the remaining SU8 film creates pattern features during wet etch). The substrate was immersed in a buffer oxide etch (BOE, consisting of six parts of 40% NH_4F and one part of 49% HF solutions) for 2-3 min (wet

[c] Parts of this chapter are reproduced by previously published work: Hsieh, W.-T., Hsu C.-J., Capraro B. R., Wu T., Chen C.-M., Yang S., Baumgart T. (2012). Curvature Sorting of Protein Domains on Solid-Supported Wavy Membranes. *Langmuir*, 28 (35), 12838–12843.

etch). The remaining SU8 2 film on the substrate was then removed by plasma etching for 20 min. To smooth any rough edges produced by the anisotropic etch, the cover slip was immersed in BOE for 30 s[66]. Transmitted light images were registered using fluorescent microspheres to assign regions of valleys and hills on the wavy surface[67].

2.1.2 Microfluidic chamber fabrication

Fabrication of silicon wafer master

Designs for master were created using LayoutEditor software. The design was then printed onto a transparency by PHOTOPLOT STORE. For master fabrication, silicon wafer was spin coated with SU-8 2000 at 3000 rpm and then soft baked at 65 ˚C for 1 min. Transparency with design printed was then attached onto the SU-8 coated wafer, followed by UV exposure with energy of 150 mJ/cm2 (Karl Suss MA4 Mask Aligner). After post exposure bake at 65 ˚C and 95 ˚C for 1 min respectively, the wafer was immersed in SU-8 developer and then washed with isopropyl alcohol for 10 s. Finally, the mater was air dried and then hard baked at 200 ˚C for 30 min.

Fabrication of microfluidic chambers by replica molding

PDMS precursor mixed with curing agent (10:1 in weight ratio) was poured onto the master and cured at 65 ˚C for 8 hr. PDMS replica was then peeled off from the master and two holes were drilled by hole punctures for tubing connections. The replica and

cover glasses were then oxidized by oxygen plasma for 45 s. Microfluidic chambers were assembled by placing PDMS replica in contact with cover glass.

2.2 Peripheral Proteins on Wavy Membranes[d]

2.2.1 Supported lipid bilayers on wavy glass substrates

1,2-dioleoyl-sn-glycero-3-phosphocholine (DOPC), L- α -phosphatidylinositol 4,5-bisphosphate (PtdIns(4,5)P_2) (Brain, ammonium salt), 1,2-dioleoyl-sn-glycero-3-phospho-L-serine (DOPS), 1,2-dioleoyl-sn-glycero-3-phosphoethanolamine-N-(cap biotinyl) (Biotinyl Cap PE), brain ganglioside GM1, and extruder accessories were purchased from Avanti Polar Lipids (Alabaster, AL). Texas Red-1,2-dihexadecanoyl-sn-glycero-3-phosphoethanolamine triethylammonium salt (Texas-Red DHPE), streptavidin-FITC, and Alexa Fluor 555-conjugated CTB (CTB-A555) were purchased from Invitrogen (Carlsbad, CA). Calcium- and magnesium-free 150 mM NaCl and 7.5 mM phosphate pH 7.4 buffer was used in the preparation of vesicle solution.

Phospholipids were dissolved in chloroform and spread on the walls of a round bottom flask and evacuated in a desiccator to produce an even lipid film. The lipid film

---

[d] Parts of this chapter are reproduced by previously published work: Hsieh, W.-T., Hsu C.-J., Capraro B. R., Wu T., Chen C.-M., Yang S., Baumgart T. (2012). Curvature Sorting of Protein Domains on Solid-Supported Wavy Membranes. *Langmuir*, 28 (35), 12838–12843

was rehydrated, sonicated for 30 min, extruded 21 times through a polycarbonate filter with 50 nm pores at room temperature. A supported lipid bilayer was formed by small unilamellar vesicle (SUV) fusion onto the hydrophilic wavy glass substrate. Before vesicle fusion, the wavy glass substrate was cleaned by sonicating sequentially in 2% Hellmanex solution (Hellma, Mullheim, Germany) for one hour, and 30 min each for water and ethanol. For the curvatures in our wavy surface (minimum curvature of radius ~500 nm), the adhesion energy between glass substrate and lipid bilayer is large enough to overcome the bilayer's bending energy[68]. Thus, together with the recent finding showing the conformity of membranes to 100 nm silica beads[69], we could infer that lipid bilayers follow the topography of the underlying wavy substrates.

Protein or lipid partitioning on the wavy membrane was visualized by IX81 inverted confocal microscope (Olympus, Center Valley, PA) with Kalman imaging filter. The imaging chambers were produced from MatTek dishes (MatTek, Ashland, MA) by removing the original cover slip of the dish and replacing it with the fabricated wavy glass substrate attached to the dish through a thin layer of grease (Dow Corning, Midland, MI). The liquid volume covering the wavy surface was 200 μL. Fluid wavy membranes were incubated with 50-100 nM ENTH-GFP, 200-300 nM Endophilin N-BAR-Alexa Fluor 488, 200-300 nM BIN1 N-BAR-Alexa Fluor 488, or 150-500 nM CTB-Alexa Fluor 555 for 20 min. Images were normalized to the mean intensity of the frame and analyzed as a function of membrane curvature.

2.2.2 Protein adsorption isotherm on supported lipid bilayers

To determine the coverage fraction of proteins on supported lipid bilayers, adsorption isotherms were determined. Supported lipid bilayers formed by vesicle fusion as mentioned above were incubated with a series of protein concentrations at room temperature. Fluorescence intensity of proteins on the bilayer surface was quantified by confocal microscopy imaging. The data were fitted with the Langmuir isotherm to obtain a dissociation constant (Kd) and maximum surface coverage.

2.2.3 Single-molecule tracking

Dishes and buffer used for single-molecule imaging were illuminated via a 100 W UV lamp (Ultra Violet Products, Upland, CA) for at least 2 hours before fluorescence imaging experiments to reduce background fluorescence levels. Single molecules were imaged via a 60x 1.45NA TIRF lens (Olympus, Center Valley, PA) on an inverted microscope system (IX71, Olympus, Center Valley, PA) equipped with an EM-CCD camera (Hamamatsu, Bridgewater, NJ) using a 488 nm laser (50 mW, Coherent, Santa Clara, CA). Particle localization and tracking were performed with the help of MATLAB to generate single-molecule trajectories.

2.2.4 Fluorescence recovery after photobleaching (FRAP)

FRAP measurements were performed on an inverted IX71 fluorescence microscope (Olympus) equipped with an EM-CCD camera (Hamamatsu) for solid-

supported membrane or on IX81 inverted confocal microscope (Olympus) for the tether-GUV system. Pre- and post- bleach images were acquired with attenuated illumination using an OD1.0 neutral density filter (Thorlabs, Newton, NJ). On the solid-supported membrane, a circular area with diameter of 21.6 μm was bleached for 30-60 sec. The recovery curve was fitted to a two-dimensional diffusion model by Soumpasis[70] to obtain the diffusion coefficient (D). For the tether-GUV system, GUVs were prepared as described[13], except that 50% 1-palmitoyl-2-oleoyl-sn-glycero-3-phosphoethanolamine (Avanti) was included. The membrane tether was photobleached, and the recovery curve was fitted to a one-dimensional diffusion model[40].

2.2.5 Atomic Force Microscopy (AFM) and Membrane Curvature

AFM was performed using an Agilent 5420 microscope (Santa Clara, CA), and all accessories were purchased from Veeco (Plainview, NY). A silicon nitride probe with a spring constant of 3 N/m was used in tapping mode with scanning frequencies from 0.5-1.5 Hz. Surface curvature (C) was determined from the height profile (z) by using the definition of curvature in Eq. 2.1, where z´ and z´´ are first and second derivatives with respect to plane coordinates, respectively.

$$C = \frac{z''}{(1+z'^2)^{3/2}} \tag{2.1}$$

To evaluate the contribution from varying protein (or lipid) density due to the imaging of the surface topography, the area projection of the surface into a plane was calculated with the help of MATLAB (MathWorks, Natick, MA). The resulting spatially varying area density was then convolved with the point spread function of the confocal microscope.

2.3 Derivatives of GM1 on Giant Unilamellar Vesicles[e]

2.3.1 Preparation of GUVs

In uncrosslinking studies, the lipid composition included **1** to **5** as detailed in Figure 4.2A, 1 mole% different derivatives of GM1-A568, and 0.2 mole% Fast DiO (3,3'-dilinoleyloxacarbocyanine perchlorate) (Invitrogen, Carlsbad, CA) as a marker for Ld phase. For CTB crosslinking studies, derivatives of GM1-Alexa568 were replaced with unlabeled GM1 species, and 0.2 mole% TR-DHPE (Invitrogen) was used as a marker for Ld phase. To prepare GUVs, 100 µl of 2 mM lipid solution was spread on ITO glass slides (Delta-Technologies, Stillwater, MN) at 60°C and evacuated in the desiccator for at least 2 h. Two slides were then combined together with two silicon

[e] Parts of this chapter are reproduced from previously published work: Chinnapen, D. J.-F., Hsieh, W.-T., te Welscher, Y. M., Saslowsky, D. E., Kaoutzani, L., Brandsma, E., D'Auria, L., Park, H., Wagner, J. S., Drake, K.R., Kang, M., Benjamin, T., Ullman, M. D., Costello, C.E., Kenworthy, A.K., Baumgart, T., Massol, R.H., Lencer, W. I. (2012) A native lipid-sorting pathway from PM to ER for the unsaturated species of ganglioside GM1. *Developmental Cell*, 23 (3), 573-586.

spacers (Grace Bio-Labs, Bend, OR), one of which enclosed the spreading area of lipid and 100 mM sucrose solution, followed by the incubation at 60°C in the presence of AC field (2 V/mm, 5Hz) for 2 h. After GUV formation, 2.5% v/v Cholera Toxin subunit B-Alexa488 (Invitrogen) stock solution (0.2 mg/ml in phosphate buffer saline) was added to GUVs containing GM1.

2.3.2 Imaging

The GUVs were imaged by fluorescence confocal microscopy (FV300 scanning system integrated with a motorized inverted microscope IX81; Olympus, Center Valley, PA), using a 60x, 1.2 NA water immersion lens, with coverslip correction collar (Olympus).

2.3.3 Quantitative image analysis to determine GM1/CTB complex partition

The phase partition for GM1-CTB-A488 complex was determined by quantitative image analysis through ImageJ (National Institute of Health, Bethesda, MD). For each GUV, based on Ld or Lo phase determined from TR-DHPE (Ld phase preferred dye), green fluorescence intensity from GM1-CTB-A488 complex in each phase at four randomly chosen regions was measured as I_0. Subsequently, the averaged background intensity obtained from eight different regions near the GUV was subtracted from I_0, which gave the net intensity, I_g. The base-10 logarithm of averaged intensity (I_g) ratio for Ld versus Lo phase was then calculated and analyzed: for the value smaller than -0.15,

Lo phase partition was assigned; between -0.15 and 0.15, no phase partition (NPP) was assigned; larger than 0.15, Ld phase partition was assigned.

2.4 Protein Purifications and Fluorophore Labeling

2.4.1 ENTH-GFP, BIN1 and Endophilin N-BAR

ENTH-GFP was purified as previously described[71]. BIN1 and Endophilin N-BAR domains were expressed as GST fusion proteins. In Endophilin N-BAR, the mutation A247C using site-directed mutagenesis allowed fluorophore labeling (in a protein where the natural cysteine was eliminated through a C108S mutation). For protein expression, BL21-Codon Plus (DE3)-RIL cells (Stratagene, La Jolla, CA) were transformed with the plasmid of interest, grown in LB media, induced with isopropyl-β-D-thiogalactoside (IPTG), and harvested via centrifugation. Pellets were resuspended in a pH 7.4 buffer containing 300 mM NaCl, 20 mM Tris, 1 mM dithiothreitol (Fisher, Pittsburgh, PA), and 0.2 mM phenylmethylsulfonyl fluoride (Thermo Scientific, Logan, UT). The cells were lysed by tip-sonication and centrifuged at 4 °C. The supernatant was applied to a GST affinity column (GE, Piscataway, NJ), followed by protease digestion to cleave off the GST moiety. The product was further purified by ion-exchange chromatography. Alexa Fluor 488 fluorophore was conjugated to cysteine residue 247 in Endophilin N-BAR and endogenous cysteine residues at positions 57 and 95 in BIN1 N-BAR via Alexa Fluor 488-C5-maleimide (Invitrogen).

2.4.2 Endophilin mutants

Endophilin H1 helix insertion-deleted mutant (ΔH1i) was generously given by Prof. Naoki Mochizuki (National Cerebral and Cardiovascular Center Research Institute, Osaka, Japan). To examine BAR domain without additional helices present, we removed H0 helix from ΔH1i plasmid using thermal cycler (Biorad, Hercules, CA) (forward primer: 5'- ggggcccctgggatccttcaaagagatggaaa-3'; reverse primer: 5'- tttccatctctttgaaggatcccaggggcccc-3'). This double helices-deleted mutant was termed Ed2 in Chapter 5. Endophilin ΔH1i, ΔH0, and Ed2 constructs were purified in the same way as the aforementioned procedure for Endophilin N-BAR.

2.4.2 PRM and SH3 multivalent proteins

PRM(5) and SH3(5) plasmids were gifts from Prof. Michael Rosen (UT Southwestern Medical Center). SH3 domain was derived from Nck1 (106-168), adaptor protein involved in transducing signals from receptor tyrosine kinase to downstream signal recipient[72]; PRM domain was derived from ABL1 (606-618), a tyrosine kinase; implicated in cell differentiation, cell division, and cell adhesion[73]. Both constructs were in modified pMALc2 vectors (expressed as MBP fusion proteins), where N- and C-terminals have proteolytic sites for Tev protease digestion and C-end has histidine-tag following the proteolytic site. To enhance membrane binding and allow fluorophore conjugation, tyrosine in proteolytic site right before histidine-tag was mutated to cysteine

(ENLYFQ→ENLCFQ) using thermal cycler (Biorad, Hercules, CA) (for PRM(5), forward primer: 5'- cggctcaggatccgaaaacctgagttttgcggcccatcatcatcatcactga-3'; reverse primer: 5'- tcagtgatgatgatgatgggccgcaaaactcaggttttcggatcctgagccg-3'; for SH3(5), forward primer: 5'- ggcggatccgaaaacctgtgttttcaggcccatcatcatc-3'; reverse primer: 5'-gatgatgatgggcctgaaaacacaggttttcggatccgcc-3'). For PRM with different module number, three-step nucleotide deletion from PRM(5) was performed to generate PRM(3) and PRM(1) constructs. (1st step: forward primer: 5'-ccgcctaaacgtgaaaacctgtgtttt-3'; reverse primer: 5'-aaaacacaggttttcacgtttaggcgg-3'; 2nd step: forward primer: 5'-aagaaaaccgcagaaaacctgtgttttcagg-3'; reverse primer: 5'-cctgaaaacacaggttttctgcggttttctt-3'; 3rd step: forward primer: 5'-ggtagcggaggaagtgaaaacctgtgttttc-3'; reverse primer: 5'-gaaaacacaggttttcacttcctccgctacc-3'). PRM proteins without N-terminal histidine-tag were also engineered using site-directed mutagenesis (forward primer: 5'-tgttttcaggcctgaaagcttggcact-3'; reverse primer: 5'- agtgccaagctttcaggcctgaaaaca-3').

PRM and SH3 multivalent proteins were expressed as MBP and/or histidine-tag fusion proteins. For protein expression, BL21(DE3) cells (Invitrogen) were transformed with plasmid of interest, grown in LB media at 37 ºC and induced at OD_{600}~ 0.8 with 0.5 mM isopropyl-β-D-thiogalactoside (IPTG) at 18 ºC for 16 hr (for PRM proteins) or at 20 ºC for 16 hr (for SH3 proteins), followed by centrifugation for cells collection. Cells were then lysed by tip sonication. Lysates were then clarified by centrifuge at 18000 rpm for 40 min, at least two runs before passed through HisTrap affinity column (GE, Pittsburgh,

PA) for proteins with histidine-tag or MBPTrap affinity column (GE) for proteins without histidine-tag, followed by HiLoad Superdex 200 16/60 200 prep grade (GE). The elution was then digested with ProTevPlus (Promega, Madison, WI) overnight at 4 °C to remove MBP moiety overnight. The digested product was further purified by ion-exchange column (GE), either HiTrapQ column (for SH3) or HiTrap SP column (for PRM). Alexa Fluor 594-C5-maleimide (for SH3) or Alexa Fluor 488-C5-maleimide (for PRM) was then conjugated with cysteine in each protein. The final buffer solution for both proteins was 30 mM phosphate and 150 mM NaCl buffer, pH 7.4.

2.5 Examining the Mechanisms of Curvature Sensing of N-BAR Domains Using a Single Liposome-Based Kinetic Technique

2.5.1 Preparation of polydisperse liposomes

Lipid mixture composed of 99% DOPS, 0.5% 1,2-distearoyl-sn-glycero-3-phosphoethanolamine-N-[biotinyl(polyethylene glycol)-2000] (biotin-PEG2000-DSPE), and 0.5% DiD were deposited in a round bottom flask and evacuated in a desiccator for at least 2 hr, followed by rehydration overnight with 300 mM D-sorbitol solution (Fisher) to reach concentration of 1 mg/ml. Five freeze-thaw cycles were then performed to promote unilamellarity of liposomes[74]. Liposomes solution was then extruded through polycarbonate filter with 400 nm pores once at room temperature. The size of liposomes was characterized by Dynamic Light Scattering instrument (Wyatt, Santa Barbara, CA).

2.5.2 Single liposome curvature assay in a flow chamber

To immobilize single liposomes in a flow chamber, 0.1 mg/ml bovine serum albumin (BSA) (Sigma-Aldrich, St. Louis, MO), 1 mg/ml biotinylated-BSA (Fisher, Pittsburgh, PA), and 0.00125 mg/ml streptavidin (Fisher) were injected into a flow chamber consecutively and incubated for 15 min respectively. Before each protein injection, flow chamber was rinsed thoroughly with 138mM NaCl and 4 mM phosphate buffer. Polydisperse liposome solution with concentration of ~ 0.001mg/ml was then infused into the treated chamber. Once the surface was covered with enough liposomes (around hundreds of liposomes per field of view), the buffer was injected to remove unbound liposomes.

2.5.3 Membrane binding kinetics of proteins

The protein of interest labeled with Alexa Fluor 488 (Invitrogen, Carlsbad, CA) was introduced into a chamber via a programmable syringe pump (KD Scientific, Holliston, MA). Protein intensity against time was captured via a 60x 1.45NA TIRF lens (Olympus, Center Valley, PA) on an inverted microscope system (IX71, Olympus, Center Valley, PA) equipped with an EM-CCD camera (Hamamatsu, Bridgewater, NJ) and a shutter (Sutter, Novato, CA).

2.5.4 Algorithm for liposome localization and size conversion

The localization of single liposome was accomplished by implementing MATLAB algorithm. First, any pixel above the intensity threshold T1, the average pixel intensity of one single frame plus four standard deviations of pixel intensity, was selected as a single object. Subsequently, the pixels of the objects selected by T1 must exceed the second threshold T2 (T2=1). T2 was set for removing occasional bright pixels resulting from camera shot noise. To avoid identification of densely distributed liposomes as a single subject, the third threshold T3 was set as a maximum pixel number. The objects which passed all three thresholds were identified as a single liposome and then processed for the determination of spatial coordinates (Figure 2.2).

To determine vesicles size through fluorescence intensity of vesicles, a conversion factor (k) between vesicle size and fluorescence intensity needed to be determined. Assuming fluorescent lipids distributed homogeneously among vesicles and assuming that vesicles were spherical shells, the fluorescence signal from the vesicles (I_v) would be proportional to the surface area of the liposome (A).

$$I_v \propto 4\pi r^2 \tag{2.2}$$

The mean radius (r_{Mean}) was determined by a second approach, e.g. dynamic light scattering or electron microscopy. The conversion factor, k, was then introduced for correlation between r_{Mean} and $(\sqrt{I_v})_{\text{Mean}}$,

$$k = \frac{r_{\text{Mean}}}{(\sqrt{I_v})_{\text{Mean}}} \tag{2.3}$$

With k determined, fluorescence intensity distributions can then be transformed into size distributions (Figure 2.3).

2.5.6 Intensity tracking of protein signal

Protein binding kinetics on single liposomes were determined with the help of single-molecule tracking algorithm implemented in MATLAB. Protein signal in each frame was first localized as mentioned in *2.5.5*. Only particles with colocalized fluorescent lipid signal were analyzed. The rate constant was obtained by fitting protein intensity (I_P) as a function of time (t) with Eq. 2.4.

$$I_P(t) = A(1 - \exp(-kt)) + I_0 \tag{2.4}$$

2.5.7 TIRF-FRAP measurement

The dissociation process was measured by combining total internal reflection fluorescence (TIRF) with fluorescence recovery after photobleaching approach[75] (TIRF-FRAP). To be able to employ this approach, we first adapted the theory of TIRF-FRAP by Thompson et al.[75] to our experimental system, in which we had lipid vesicles tethered to the substrate instead of having supported lipid bilayers[75,76]. We then expressed the reaction kinetics in reaction-limited and diffusion-limited regimes.

A scenario in which protein molecules (P) freely diffuse in bulk solution and react with binding sites on immobilized lipid vesicles (V) to form protein-lipid complexes (PV) is considered. The reaction can be expressed as

$$P+V \leftrightarrow PV \tag{2.4}$$

with k_{on} and k_{off} as forward and reverse rate constants, respectively. According to the theory derived by Thompson et al.[75], the general form of recovery fluorescent signal as a function of time, $G(t)$, is

$$G(t) = G(0)L^{-1}_{\nu \to R_R t} \frac{\int |J'(\xi)|^2 N(\xi,\nu) d^2\xi}{\int |J'(\xi)|^2 d^2\xi} \tag{2.5}$$

where

$$N(\xi,\nu) = \frac{(\nu + \xi^2 R_{BLD}/R_R)^{1/2} + (R_R/R_{BND})^{1/2}}{(1+\nu+\xi^2 R_{SD}/R_R)(\nu+\xi^2 R_{BLD}/R_R)^{1/2} + (\nu+\xi^2 R_{SD}/R_R)(R_R/R_{BND})^{1/2}} \tag{2.6}$$

L^{-1} refers to inverse Laplace transform. J is an intensity profile function with unitless argument. ξ and ν are spatial and frequency variables from Fourier transform, respectively. Four characteristic rates determine the rate and shape of recovery profile. R_R represents the rate for the reaction, which is the reverse rate constant, k_{off}, in eq.2.4. R_{BND} is the normal bulk diffusion rate of protein molecules. R_{SD} is the rate for surface diffusion,

and R_{BLD} is the rate for lateral diffusion in solution. When vesicles are immobilized on the surface, R_{SD} can be assumed to be zero and thus N in eq. 2.6 can be rewritten as

$$N(\xi,\nu) = \frac{(\nu + \xi^2 R_{BLD}/R_R)^{1/2} + (R_R/R_{BND})^{1/2}}{(1+\nu)(\nu + \xi^2 R_{BLD}/R_R)^{1/2} + (\nu)(R_R/R_{BND})^{1/2}} \tag{2.7}$$

For reaction-limited case, in which $R_R << R_{BND}$ and $R_R << R_{BLD}$, $G(t)$ and $N(v)$ are expressed as

$$N(\nu) = \frac{1}{1+\nu} \tag{2.8}$$

$$G(t) = G(0)L^{-1}_{\nu \to R_R t}\frac{1}{1+\nu}\cdot\frac{\int |J'(\xi)|^2 d^2\xi}{\int |J'(\xi)|^2 d^2\xi} = G(0)e^{-R_R t} \tag{2.9}$$

For diffusion-limited case, where $R_R >> R_{BND}$ and $R_R >> R_{BLD}$, $N(v)$ becomes

$$N(\nu) = \frac{\nu^{1/2} + (R_R/R_{BND})^{1/2}}{(1+\nu)\nu^{1/2} + \nu(R_R/R_{BND})^{1/2}} = \frac{\nu^{1/2} + (R_R/R_{BND})^{1/2}}{\nu^{2/3} + \nu^{1/2} + \nu(R_R/R_{BND})^{1/2}} \tag{2.10}$$

Let $\nu^{1/2} \equiv X$ and $\sqrt{R_R/R_{BND}} = \sqrt{A}$, N becomes

$$N = \frac{X + \sqrt{A}}{X^3 + \sqrt{A}X^2 + X} \tag{2.11}$$

N can be rewritten as five partial fractions,

$$N = \frac{\frac{1}{\sqrt{A-4}}}{x-(\frac{-\sqrt{A}+\sqrt{A-4}}{2})} - \frac{\frac{1}{\sqrt{A-4}}}{x-(\frac{-\sqrt{A}-\sqrt{A-4}}{2})} + \frac{\sqrt{A}}{x} + \frac{\frac{-A-\sqrt{A^2-4A}}{2\sqrt{A-4}}}{x-(\frac{-\sqrt{A}+\sqrt{A-4}}{2})} + \frac{\frac{A-\sqrt{A^2-4A}}{2\sqrt{A-4}}}{x-(\frac{-\sqrt{A}-\sqrt{A-4}}{2})} \quad (2.12)$$

α_1 and α_2 are then introduced and defined as follows

$$\alpha_1 \equiv \frac{-\sqrt{A}+\sqrt{A-4}}{2}$$

$$\alpha_2 \equiv \frac{-\sqrt{A}-\sqrt{A-4}}{2}$$

After Laplace transform, *G(t)* is obtained as

$$\begin{aligned}\frac{G(t)}{G(0)} &= \frac{1}{2\sqrt{A-4}}[(2-A-\sqrt{A^2-4A})\alpha_1 \exp(\alpha_1^2 R_R t)\cdot erfc(-\alpha_1\sqrt{R_R t})] \\ &+ \frac{1}{2\sqrt{A-4}}[(A-\sqrt{A^2-4A}-2)\alpha_2 \exp(\alpha_1^2 R_R t)\cdot erfc(-\alpha_2\sqrt{R_R t})]\end{aligned} \quad (2.13)$$

Let $w(i\eta) = e^{\eta^2} erfc(\eta)$ and notice the following relations, $\alpha_1\alpha_2 = 1$, $\alpha_1 - \alpha_2 = \sqrt{A-4}$, and $\alpha_1 - \alpha_2 = \sqrt{A}$, which give *G(t)* as

$$\frac{G(t)}{G(0)} = \frac{1}{\alpha_1-\alpha_2}[-\alpha_2 w(-i\sqrt{\alpha_1^2 R_R t}) + \alpha_1 w(-i\sqrt{\alpha_2^2 R_R t})] \quad (2.14)$$

since $R_R >> R_{BND}$, therefore

$$\alpha_1 \sim 0$$
$$\alpha_2 \sim -\sqrt{\frac{R_R}{R_{BND}}} \tag{2.15}$$
$$\alpha_1^2 \sim [1/2\sqrt{\frac{R_R}{R_{BND}}}(-1+(1-2R_{BND}/R_R))]^2 = \frac{R_{BND}}{R_R}$$

$$\frac{G(t)}{G(0)} \approx w(-i\sqrt{R_{BND}t}) \tag{2.16}$$

To determine which regime the protein dissociation process in our system belonged to, observed dissociation constants (k_{obs}) were measured in various protein concentrations. Constant k_{obs} obtained at various concentrations revealed that protein dissociation in our single liposome-based kinetics setup was independent of protein concentrations (Figure 2.4), which implied the dissociation process was within reaction-limited regime. Based on the expression of *G(t)* in reaction-limited regime (eq. 2.9), this finding suggested the measured recovery rate constants mainly reflected protein dissociation rates, k_{off}.

2.6 Line Tension Measurement in Langmuir Trough and GUVs

2.6.1 Lipid monolayer setup

For monolayer experiment, a Langmuir trough (Kibron Inc., Helsinki, Finland) was filled with ~20 ml of pH7.4 phosphate saline buffer (phosphate 30 mM, NaCl 150mM, and DTT 1mM). Surface pressure was monitored using Wilhelmy method[77] and the FilmWare software, while surface area was controlled by a pair of motorized Teflon

barriers (Kibron Inc., Helsinki, Finland). The surface pressure was first calibrated with deionized water, followed by determination of a compression isotherm of phosphate buffer to ensure absence of contaminating surface-active components. Subsequently, approximately 10 nmole of lipid mixture containing 30% 1,2-dimyristoyl-sn-glycero-3-phosphocholine (DMPC), (69.8-X)% dihydrocholesterol (DChol), 0.2% Texas Red-DHPE and X% of 1,2-dimyristoyl-sn-glycerol (DAG) was applied to the air/subphase interface with a 10 μl glass syringe. The lipid monolayers were visualized with an IX71 microscope (Olympus, Center Valley, PA) equipped with EM-CCD camera (Hamamatsa, Bridgewater, NJ) with a long working distance objective (60× W/IR, NA 0.90, Olympus LUMPlanFL).

The monolayer was first compressed quickly (25 $Å^2$/molecule/minute) to the transition pressure (around 10.1 mN/m), and then allowed to stabilize for 10 min. The surface pressure was then reduced at 5 $Å^2$/molecule/minute to the surface pressures of interest. For each surface pressure, several >2000-frame movies were acquired. Each image was taken at pixel resolution of 256 × 256 and exposure time as 0.016 s/frame.

2.6.2 Image processing and data analysis

Image processing and data analysis were implemented in MATLAB[54,78]. Each grey scale image was first converted to binary through thresholding. Our code allowed selection of domain of interest with mouse clicks inside and outside of the domain, and

thus localization of "centers of mass" of domains frame by frame. The trace coordinates of domains for each image was converted from Cartesian coordinates, [x, y(x)], to polar coordinates [r, $r(\theta)$]. The radial deviation $\Delta r(\theta)=r(\theta)-\langle r(\theta)\rangle$, where $\langle r(\theta)\rangle$ is average radius, was then analyzed via fast Fourier transformed (FFT) to yield mode powers for every trace, ζ_n^2, from which the time-averaged mode powers, $\langle\zeta_n^2\rangle$, were obtained.

2.7 Examining Interactions between IgG and Silicone Oil

2.7.1 Langmuir-Blodgett trough experiment and fluorescence imaging

The compression isotherm and titration experiments were performed with a MicroTroughXS system (Kibron Inc., Helsinki, Finland). The fluorescence images were taken using an inverted fluorescence microscope (IX 71, Olympus, Center Valley, PA) equipped with an EM CCD camera (Hamamastu). A DualView system (DV2, Photometrics, Tucson, AZ) was mounted in front of CCD camera to facilitate simultaneous dual-color imaging. The excitation source was a continuous wavelength mercury lamp. For Texas Red or Sulforhodamine fluorescence, an excitation filter (540-580 nm) and emission filter (593-668 nm) were used. For BODIPY, the excitation filter (450-490 nm) and emission filter (500-550 nm) were used.

2.7.2 Compression isotherm measurement

The surface area of buffer was first compressed to 7000 mm^2, then 4.3 μL of 0.96 mg/mL silicone oil (Fisher) dissolved in chloroform was applied at the air/buffer

interface. After waiting 20 min for the organic solvent to evaporate, the barriers were relaxed to the full trough area, then compressed at 10 mm/min while the compression isotherm of the silicone oil was recorded. For SO/IgG-TR systems, 250-1000 μL of 0.020 mg/mL dye-labeled protein aqueous solution was injected into the subphase behind the barriers. Then the barriers were relaxed to full trough area and the system was allowed to equilibrate for 1 h for the protein to adsorb to the interface at near 0 mN/m surface pressure. The compression isotherm of silicone oil/protein mixture was obtained by compressing the barriers at 10 mm/min.

2.7.3 Titration experiment

The surface area of buffer was first compressed to 3000 mm^2, followed by the spreading of 0.5-10 μL of 0.96 mg/mL silicone oil in chloroform solution at the interface and solvent was allowed to evaporate for 20 min. Dye-labeled protein solution (250 μL, 0.02 mg/mL) was injected into the subphase every hour until the final concentration of protein in the solution reached 1.3 μg/mL. Fluorescence images were collected 1 h after the protein injection.

2.7.4 TEM imaging

SO or SO/IgG films at a given surface pressure were transferred onto clean cover glass via Langmuir-Schaefer approach and then dried in open air. Platinum replicas of transferred film were made by coating transferred samples with a thin layer of platinum

(2.3 nm) and carbon (7.3 nm)[79], followed by floating on a 10% hydrofluoric acid solution for 2-3 hr. After coverslips dissociated from replica, replica pieces were rinsed sequentially with an Ivory soap solution for 5 sec and a Clorax bleach solution for 30 min. The replica pieces were then rinsed with water before being mounted to formvar-coated grids. TEM images were acquired from JEM-1011 transmission electron microscope (JEOL USA, Peabody, MA). To determine sample thickness by TEM, images were taken at three different tilt angles of sample holder, including -20°, 0°, and +20°. Domain thickness was then estimated from the change of projected length at various tilt angles as described in Figure 2.5.

2.7.5 MALDI-TOF mass spectrometry

PDMS elastomers were cut into small pieces and swelled in toluene overnight while stirring. The solvent was evaporated under vacuum line to concentrate the extract. Then 10 μL chloroform was added into the tube to redissolve the extract. Dithranol was dissolved in chloroform at 0.25 M as the matrix, and silver trifluoroacetate dissolved at 1.25 M as the salt. The polymer/matrix/salt mixture was in volume ratio 2/1/1, and 1 μL of sample was applied onto MALDI plate and dried. MALDI-TOF MS measurements were performed with a Bruker Daltonics Ultraflex MALDI-TOF mass spectrometer, in a mass range from m/z 0-4,000.

2.7.6 Fluorometry

Steady-state fluorescence data were collected on a Varian Cary Eclipse fluorescence spectrometer. IgG-TR was dissolved in 10 mM phosphate buffer at 100 μg/mL, and diluted to concentrations ranging from 0.1-10 μg/mL in Eppendorf tubes. The solutions were frozen in liquid nitrogen and lyophilized under vacuum. 1.0 mL of SO was added to each tube to redissolve the protein. Solutions were sonicated to ensure protein was completely dissolved. The fluorescence intensity was measured using a 0.9 mL quartz cell (Starna Cells) at excitation wavelength 550 nm (excitation slit 5 nm) and collected at 580-700 range (emission slit 5 nm) at 20 °C, PMT voltage = 1000 V.

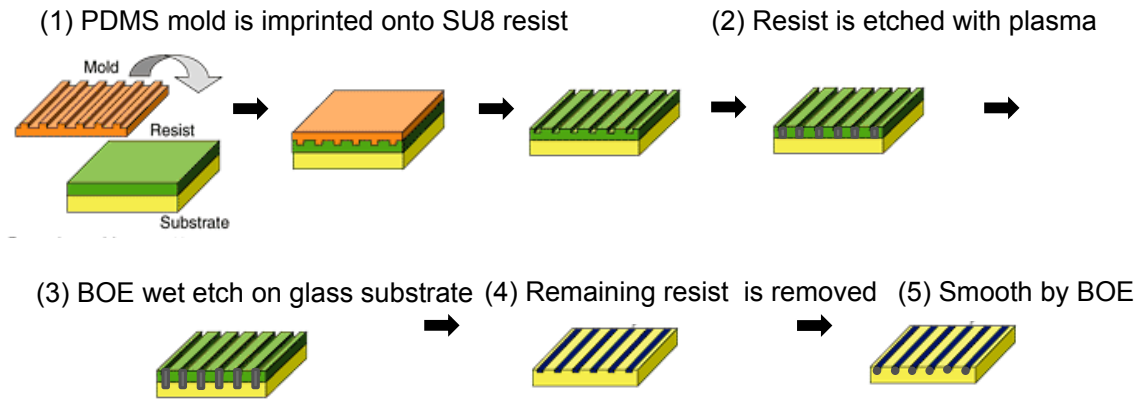

Figure 2. 1 Fabrication of wavy glass substrate.

PDMS mold with desire feature is first imprinted to SU8 2000 coated glass substrate. After crosslinking of SU8 2000, the resist is etched with CF_4 and O_2 plasma until the underlying glass substrate is partially exposed. The substrate is then immersed into BOE for wet etch, followed by removal of remaining SU8 2000. Finally, the wavy substrate was smoothed by BOE.

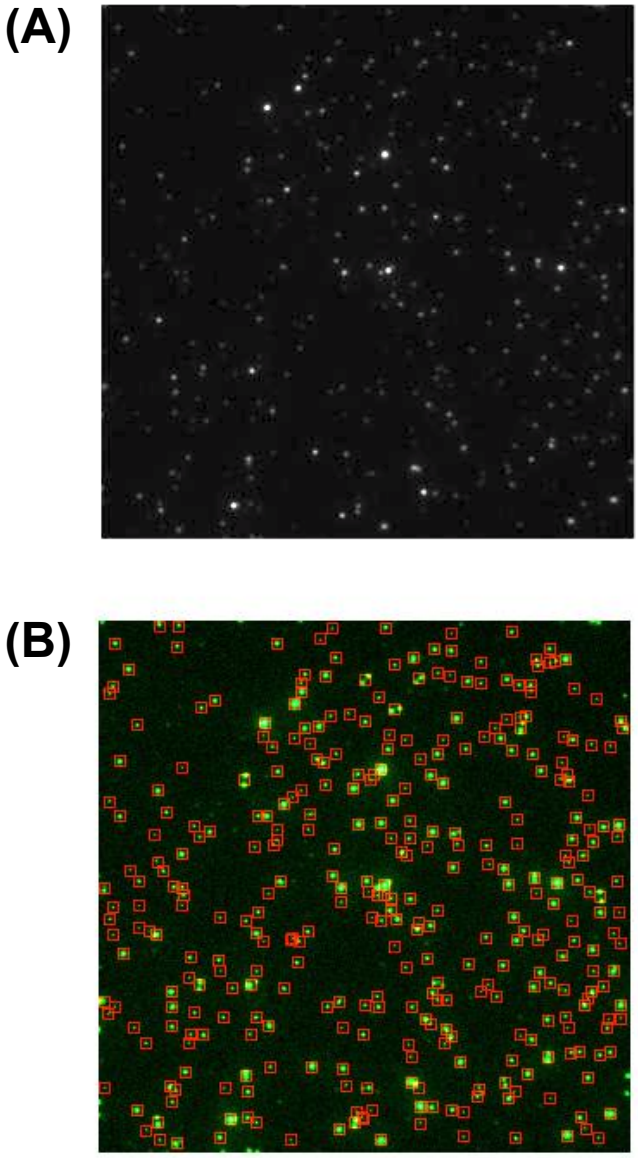

Figure 2. 2 Localization of single liposomes.

(A) Representative image acquired from SLiC assay setup. (B) Particle localization by MATLAB algorithm. Each red box encloses particle being identified by thresholding described in *2.5.4*.

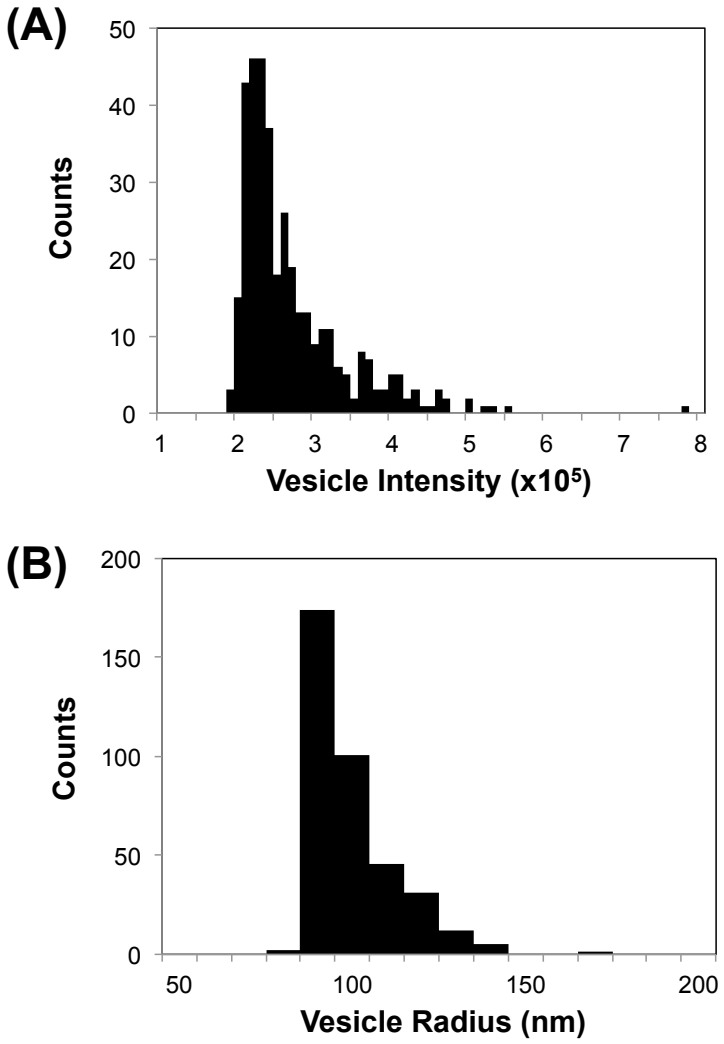

Figure 2. 3 The transformation from the fluorescence intensity distribution to size distribution.

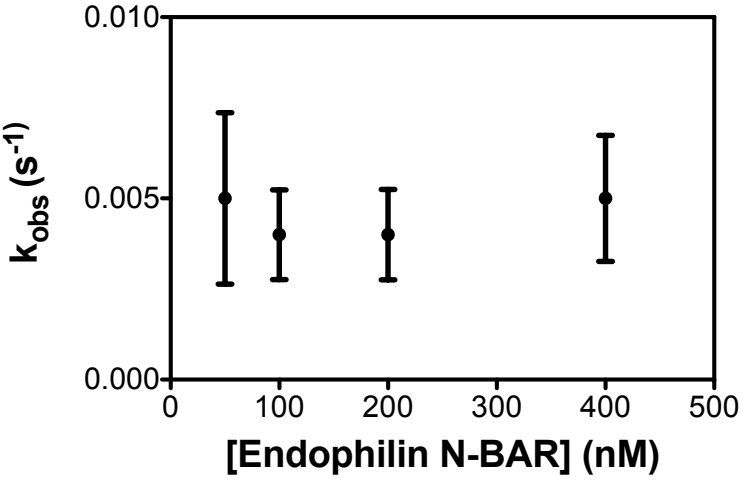

Figure 2. 4 The observed recovery rate through TIRF-FRAP approach.

TIRF-FRAP experiments were performed at various Endophilin N-BAR concentrations. Each data points were the average of at least 30 vesicles. Error bars represent standard deviations.

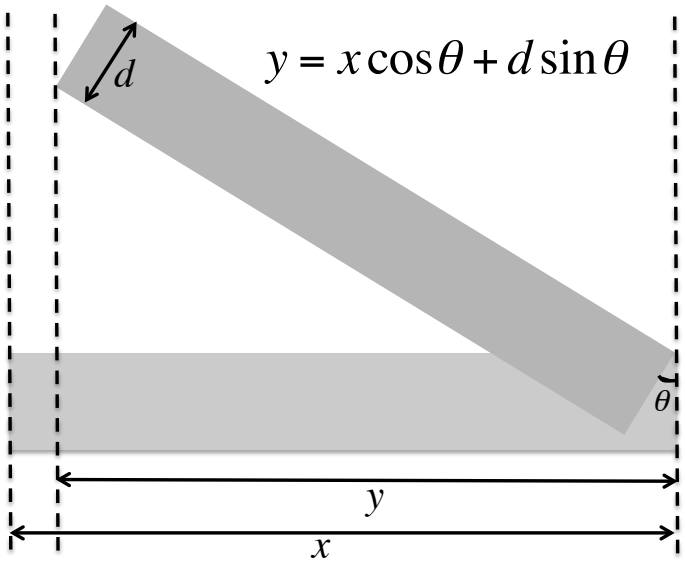

x: projected length before the tilt of sample holder
y: projected length after the tilt of sample holder
d: sample thickness
θ : tilt angle

Figure 2. 5 Determination of sample thickness by TEM.

The projected lengths of a sample before and after tilting of a sample holder allowed estimation of sample thickness.

CHAPTER 3: Curvature Sorting of Peripheral Proteins on Solid-Supported Wavy Membranes[f]

In order to study curvature sorting of peripheral proteins among regions of both positive and negative membrane curvature, a wavy glass substrate was fabricated via a combination of photolithography and wet etching to generate periodic topographic features with wavelength of about 1 μm and depth of 110 nm (Fig. 3.1A-B). The surface topography was characterized using atomic force microscopy (AFM) (Fig. 3.1C-D) which allowed computation of local surface curvatures (inset in Fig. 3.1D). The variation in surface area density caused by the projection of the wavy surface into the imaging plane[80] was estimated to be 0.3%. As becomes more obvious below, this effect is small compared to fluorescence patterns resulting from curvature partitioning. Wavy fluid membranes composed of 1,2-dioleoyl-sn-glycero-3-phosphocholine (DOPC) were obtained by the fusion of small unilamellar vesicles (SUVs) onto the glass surfaces.

3.1 Distribution of Peripheral Proteins on Wavy Membranes

[f] Parts of this chapter are reproduced by previously published work: Hsieh, W.-T., Hsu C.-J., Capraro B. R., Wu T., Chen C.-M., Yang S., Baumgart T. (2012). Curvature Sorting of Protein Domains on Solid-Supported Wavy Membranes. *Langmuir*, 28 (35), 12838–12843

We examined the lateral distributions of ENTH, N-BAR domains, and cholera toxin subunit B (CTB) on wavy membranes to evaluate the effect of signs of curvatures. Proteins bearing fluorescent tags were incubated with supported wavy membranes, and the spatial distribution was visualized via confocal fluorescence microscopy. ENTH domains exhibited preferential partitioning into positively curved membrane regions (Fig. 3.2A). For ENTH experiments, membranes consisted of 1% L-α-phosphatidylinositol 4,5-bisphosphate (PtdIns(4,5)P2) in a background of DOPC lipids. This curvature-dependent distribution was not observed for the fluorescent PtdIns(4,5)P2 analog BODIPY-TMR PtdIns(4,5)P2 embedded in the curved membranes (in the absence of ENTH), indicating that protein sorting was not influenced by the distribution of PtdIns(4,5)P2 (data not shown, but confer the work by Capraro et al.[71]). The N-BAR domains of both Endophilin and BIN1 (Bridging INtegrator 1[81]) preferentially distributed into positively curved membrane regions (Fig. 3.2B-C). For Endophilin and BIN1 experiments, membranes were composed of 5% 1,2-dioleoyl-sn-glycero-3-phospho-L-serine (DOPS) in a background of DOPC. The low content of negatively charged lipids was chosen in order to maintain a large fraction of mobile proteins and lipids (see below). In striking contrast, CTB was found to partition into negatively curved membrane regions (Fig. 3.2D). For CTB membranes consisted of a mixture of 1% GM1 and 99% DOPC.

In line with published results[23,82], two molecules used as controls, streptavidin (protein) and Texas-Red DHPE (lipid), were observed to be insensitive to membrane curvatures (Fig. 3.2E-F).

In order to quantify protein distributions with respect to membrane curvature, confocal images were normalized with respect to the average fluorescence intensity of the image frame. Averaging the normalized intensities in corresponding curvature regions substantially improved signal-to-noise ratios. It was found that protein density varied monotonically in the curvature range under investigation, yielding an increase of the normalized (relative to the average) fluorescence intensity from 0.79 (at the most negative curvature) to 1.46 (at the most positive curvature) for ENTH, 0.92 to 1.16 for Endophilin N-BAR, 0.91 to 1.17 for BIN1 N-BAR, and a decrease from 1.05 (at the most negative curvature) to 0.91 (at the most positive curvature) for CTB (left panel of Fig. 3.3). In contrast, streptavidin and Texas-Red DHPE showed little correlation with membrane curvature (right panel of Fig. 3.3).

Interestingly, quantitative analysis of protein fluorescence intensities revealed higher curvature sensitivity of ENTH domains compared to Endophilin N-BAR and BIN1 N-BAR (left panel of Fig. 3.3) despite the fact that for Endophilin two curvature sorting mechanisms (scaffolding and amphipathic helix insertion) might be simultaneously at work, whereas for ENTH likely only one sorting mechanism (amphipathic helix insertion) applies[25].

The negative curvature partitioning of CTB is in accordance with its crystal structure[23,83], which suggests negative (convex) curvature of the membrane binding interface of the protein. Patchy features observed in CTB fluorescence distributions (Fig. 2D) were attributed to aggregation of the CTB-GM1 complex, consistent with previously reported well-defined clusters observed in AFM studies[84].

3.2 Mobility of ENTH Domains on Wavy Membranes

The interpretation of fluorescence intensity distributions as resulting from thermodynamic equilibration requires the experimental demonstration that protein locations equilibrate on accessible time scales. To so do, we examined the lateral mobility of proteins on wavy membranes. The lateral diffusion of ENTH domains was investigated via fluorescence recovery after photobleaching (FRAP) measurements using our solid-supported wavy membrane and was compared to measurements in a tether-GUV system (Figure 3.4A-B). ENTH domains showed high (> 0.97) recovery fractions in both systems, with diffusion coefficients of 1.4 and 2.9 $\mu m^2/s$ in wavy membrane and tether-GUV system, respectively. Similar diffusion coefficients and recovery fractions were found for N-BAR domain proteins on wavy membranes (not shown).

3.3 Single Molecule Tracking on Wavy Membranes

Motivated by recent reports on concentration-dependent curvature sorting mechanisms[5,40], we next evaluated sorting behavior through single molecule tracking

experiments. In order to enable single molecule imaging, a low protein solution concentration of 0.05 nM was used. Single ENTH domains were observed to diffuse across both positive and negative curvature regions (Figure 3.4C). The spatial probability distribution (Figure 3.4D) shows that single ENTH protein domains were not preferentially localized in certain curvature regions, contrary to our observations from ensemble imaging experiments (left panel of Figure 3.3). In order to be able to compare membrane coverage fractions comparing single molecule and ensemble imaging experiments, membrane binding isotherms were measured, resulting in a dissociation constant of 290 nM for ENTH (Figure 3.5), comparable to a value measured via surface plasmon resonance[85]. Considering our protein solution concentration range for ensemble experiments, it follows that between 14 and 25% of available binding sites were covered (similar coverage fractions were determined for N-BAR domain proteins; not shown). This coverage range can be compared to a protein coverage fraction of ~0.01% for single molecule imaging experiments; i.e., the protein density in single molecule and ensemble imaging experiments differed by three orders of magnitude. Since single protein molecules in the present work were not observed to sense membrane curvature on low curvature surfaces contrary to our ensemble observations, there appears to be a threshold of protein surface coverage beyond which proteins start sensing membrane curvatures cooperatively on low curvature surfaces.

Solid-supported lipid bilayer membranes bear the potential for defect formation and subsequent protein immobilization in those defects. If defects were distributed preferentially in particular curvature regions, this could falsely suggest membrane-mediated curvature sensing of proteins. Single molecule imaging also allowed us to examine the locations of immobile molecules. No preferential binding of immobile proteins to particular geometries suggested negligible possibility of permanent trapping of molecules in specific curvature ranges (Figure 3.6). This observation further supports the notion that the fluorescence distributions reported here reflect protein distributions at thermodynamic equilibrium.

3.4 Comparisons between Wavy Membranes and GUV-tether Systems

Next, we compared curvature sensing between free floating and solid-supported membrane systems. The sensing ability of solid-supported wavy membranes was compared to a tether-GUV system, where a high curvature membrane was generated by pulling a tubule from a single GUV[27,71]. Note that membrane curvatures accessible in the tether-GUV system range from roughly 0.01 to 0.11 nm^{-1}, compared to -0.002 to 0.003 nm^{-1} on wavy membranes. For both ENTH and CTB, solid-supported wavy membranes were observed to possess higher sorting ability compared to tether-GUV system, resulting in higher slopes of normalized fluorescence intensities as a function of membrane curvature (Figure 3.7). One important difference between these two systems is that out-of-plane undulations that occur in freely suspended membranes are significantly

suppressed in bilayers strongly adhering to a solid substrate. It can be hypothesized that the membrane curvature stored in undulations leads to a renormalization of curvature sorting coefficients that would be found for a non-undulating membrane. However, future research will have to further explain differences in curvature sensitivity of proteins on solid supported versus freely suspended membranes.

3.5 Summary

In Chapter 3, we have fabricated a wavy membrane system which can be utilized as a platform for investigating the sorting of curvature-sensing molecules. The ability to establish continuous curvatures including negative and positive regimes on a single substrate allowed us to study molecules with a variety of curvature preferences. We demonstrated that ENTH and N-BAR domains prefer to partition into positive curvature areas, while CTB partitions into negative ones. Single molecule tracking results suggested that curvature sorting on substrates with low membrane curvature requires protein cooperativity. Due to its solid-substrate based nature, our system may also serve as curvature-differentiated patterned substrates to study the redistribution of cell surface receptors in live cells. Moreover, these wavy membranes could provide insights for studying cellular mechanical responses in different curvature regions.

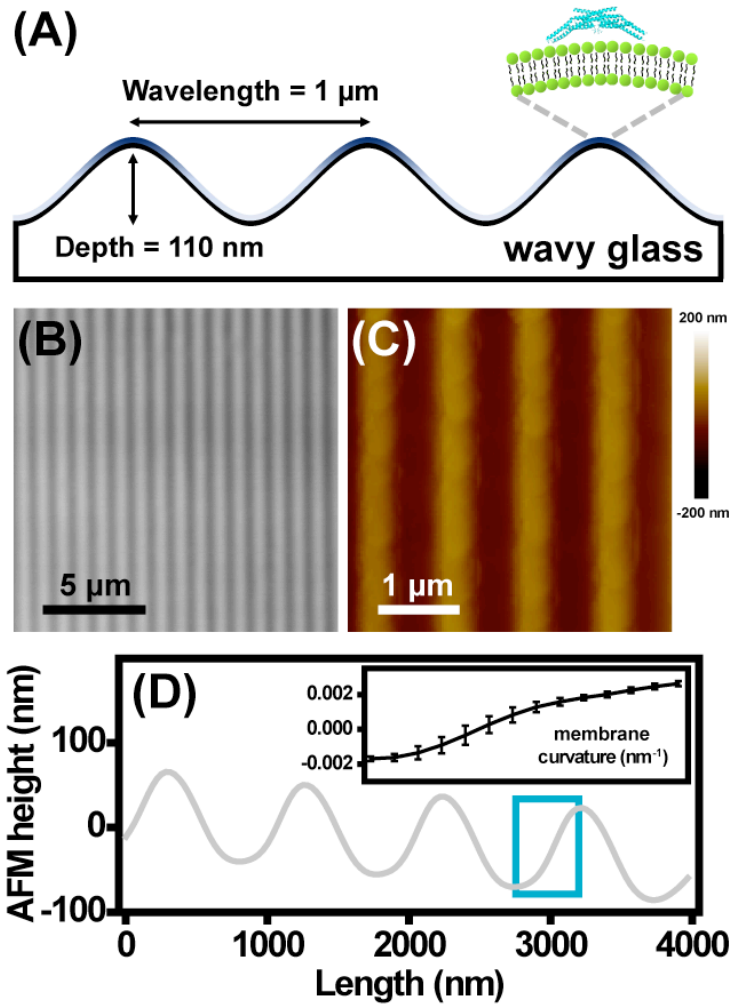

Figure 3. 1 Surface topography of wavy glass substrate.

Surface topography of a wavy glass surface. (A) Schematic cross-sectional view of the surface with a topography pattern with a wavelength of 1 µm and a depth of 110 nm supporting a fluid lipid bilayer membrane. (B) Transmitted light and (C) AFM images of a wavy glass surface with an average depth of 110 nm. (D) AFM height profile quantified from C. Note that the aspect ratio of the surface profile is adjusted for display purposes. The average curvature range within a half wavelength highlighted in the cyan box is shown in the inset. The error bars represent standard deviations from five regions with identical curvatures on a single substrate.

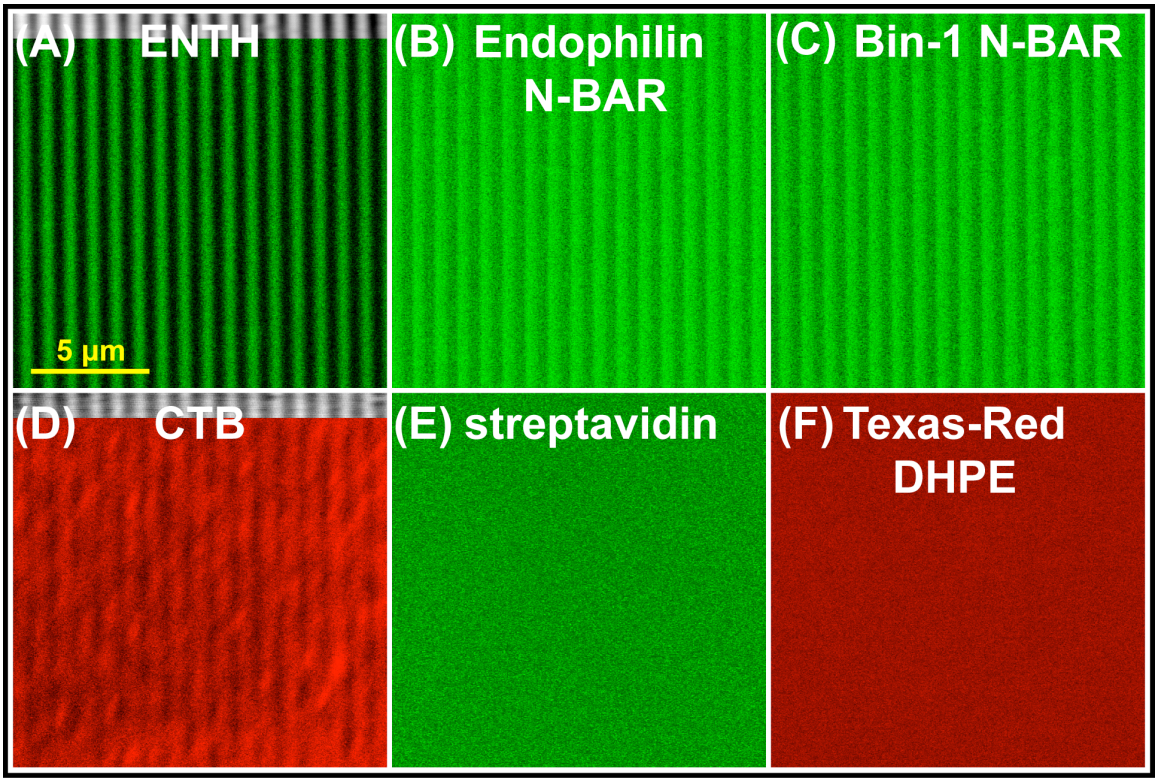

Figure 3. 2 Curvature-sensing proteins exhibit preferential partitioning on wavy membranes.

Proteins were incubated on fluid wavy membranes (containing a variety of negatively charged phospholipids or GM1 in a background of DOPC lipids) and visualized via confocal fluorescence microscopy. (A) Partitioning of ENTH-GFP into positive-curvature regions identified by transmitted light imaging (upper edge). Fluorescence distributions of (B) endophilin N-BAR-Alexa Fluor 488 and (C) BIN1 N-BAR-Alexa Fluor 488 showing enrichment in positive-curvature regions. (D) Preferential partitioning of CTB-Alexa Fluor 555 into negative-curvature regions identified via transmitted-light imaging (upper edge). No significant curvature preference was observed for (E) streptavidin-FITC bound tomembranes containing 1% cap-biotin PE and (F) 0.1% of lipid fluorophore Texas red DHPE in a wavy DOPC membrane.

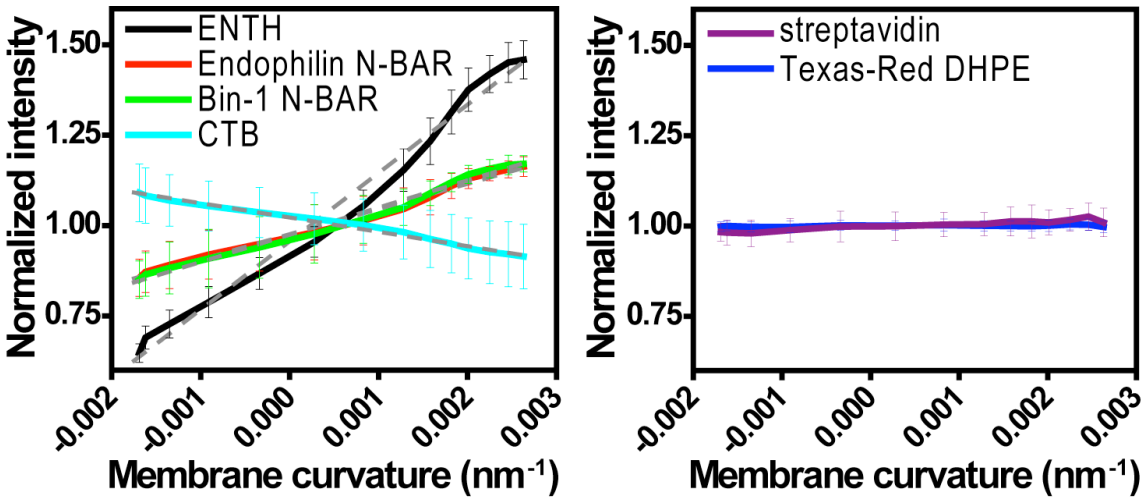

Figure 3. 3 Analysis of protein and lipid distributions with respect to membrane curvature.

Fluorescent images from confocal microscopy were normalized to the mean intensity of the image and analyzed as a function of membrane curvature. Left panel: ENTH (black), endophilin N-BAR (red), BIN1 N-BAR (green), and CTB (cyan). Right panel: streptavidin (purple) and Texas red DHPE (blue). Error bars represent standard deviations in at least six different regions on the substrate for three different bilayer preparations.

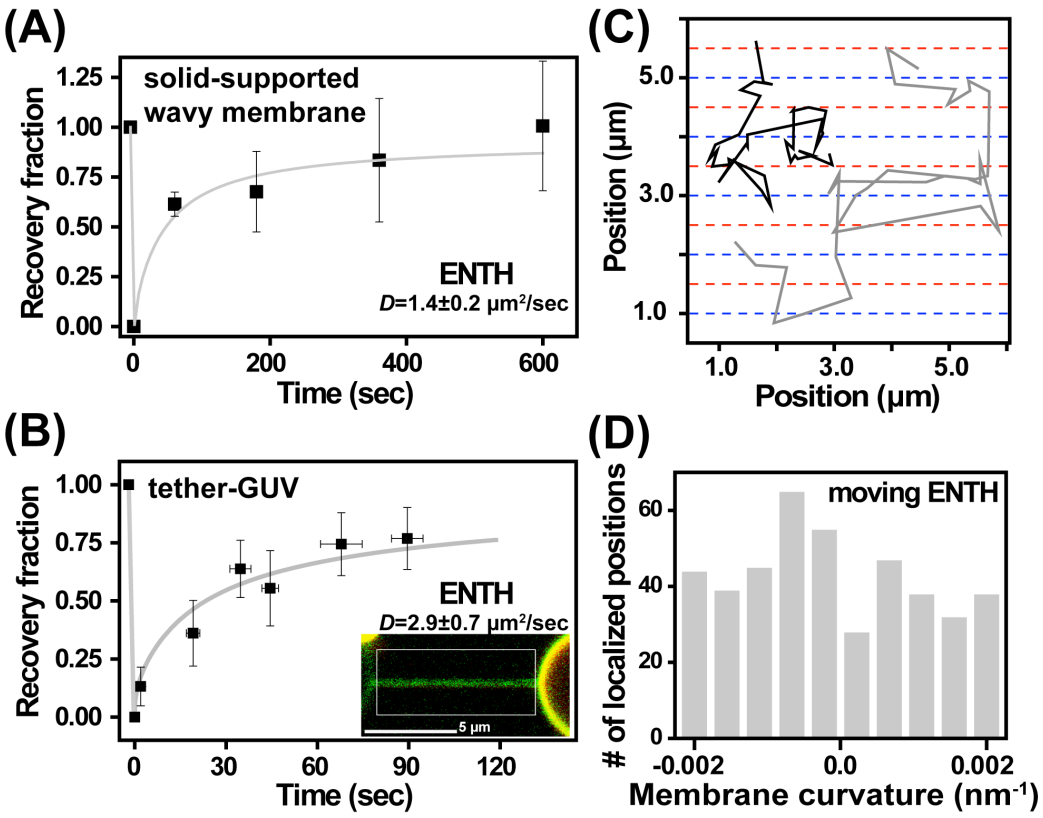

Figure 3. 4 ENTH domains exhibits lateral mobility in the wavy membrane and tether-GUV systems.

(A) The time-lapse recovery of ENTH fluorescence was examined from 2D photobleaching experiments. Error bars represent standard deviation from three bilayer preparations and fivemeasurements in total. (B) Time-lapse recovery fraction of ENTH fluorescence bound on the membrane tether generated from a single GUV containing Texas red DHPE (red) and ENTH-GFP (green). Error bars represent standard deviations from three tethers. Gray lines in A and B represent the best-fit curves. (C) Two representative trajectories of single ENTH domains on the wavy membrane. The ENTH domain was observed to diffuse across both the positive-curvature (red dashed lines) and negative-curvature regions (blue dashed lines) of the wavy membrane. (D) Spatial distribution of single moving ENTH domains on the wavy membrane with positive- and negative-curvature regions. More than 400 steps and 3 different wavy membranes were analyzed.

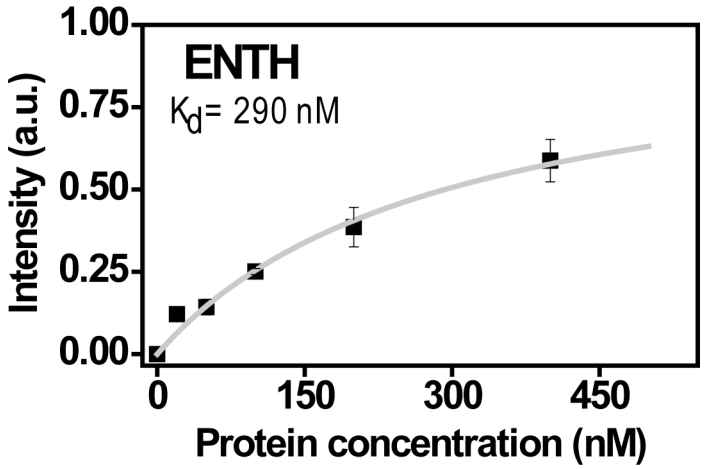

Figure 3. 5 Determination of dissociation constant and maximum coverage fraction of ENTH-GFP.

Protein density was examined by measuring fluorescence intensities on the supported membrane for a series of protein solution concentrations. The gray line shows a fit with a Langmuir adsorption model. Error bars represent standard deviations from five different regions on the substrate for two different bilayer preparations.

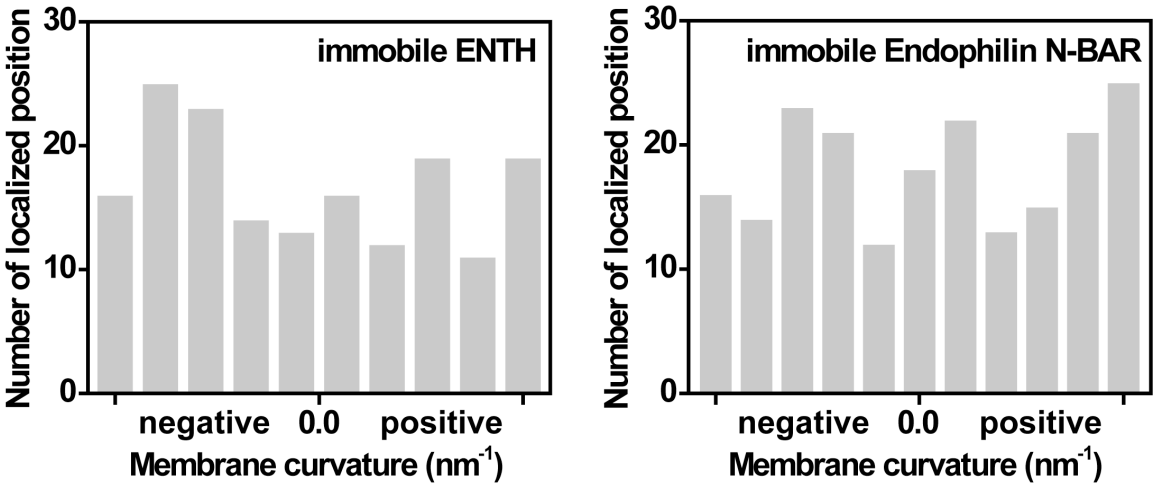

Figure 3. 6 Spatial distribution of immobile ENTH or Endophilin N-BAR on wavy membranes via single-molecule tracking.

Normalized probabilities of ENTH (left panel) and Endophilin N-BAR (right panel) were plotted against membrane curvatures. More than 150 molecules on three different wavy membranes were analyzed.

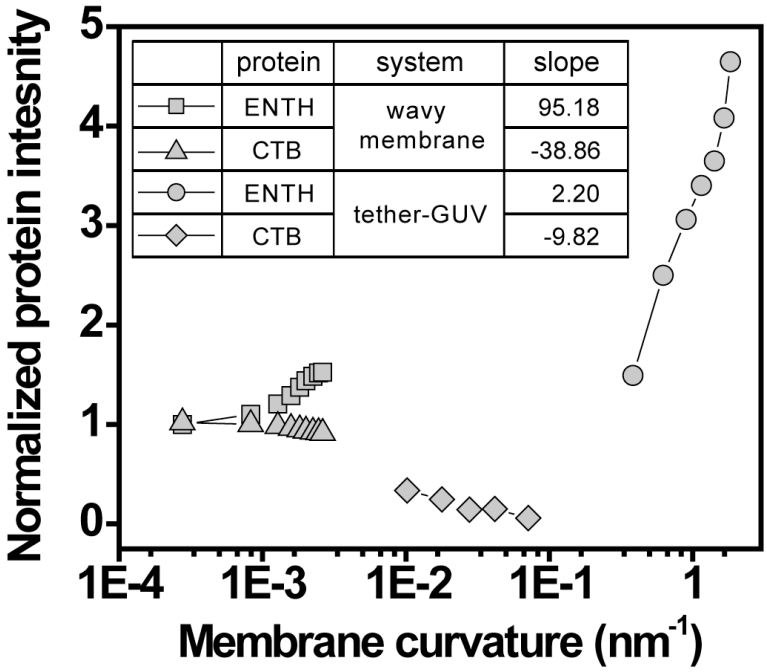

Figure 3. 7 Solid-supported wavy membrane has higher efficiency for curvature sorting compared to the tether-GUV system.

Normalized ENTH (squares) and CTB (triangles) intensities as a function of membrane curvature in a solid-supported wavy membrane were compared to the tether-GUV system (circles and diamonds; data reproduced from work of Capraro et al.[71] and Tian et al.[27], respectively). Experimental data points were normalized to the value found for zero curvature, and only the positive-curvature regime is represented in logarithmic form. The inset compares the slopes of linear sorting vs. curvature plots.

Chapter 4: Lipid Sorting by Ceramide Structure for the Cholera Toxin Receptor Ganglioside GM1[g]

To test the hypothesis that the structure of ceramide determines the routes from PM to ER, GM1 with the same oligosaccharides head group but the following acyl chain in the ceramide domain: C12:0, C16:0, C16:1 and C18:0 (Figure 4.1A). Except for C12:0, the species are natively existing ones. All structures were confirmed by mass spectrometry[34]. To evaluate the effect of lipid structure on lipid sorting, we examined the partitioning of GM1 variants in GUVs of compositions **1** to **5** (Figure 4.2A). The phase partitioning of variants was visualized by confocal microscopy using Texas red 1,2-dihexadecanoyl-sn-glycero-3-phosphoethanolamine (TR-DHPE) as a probe for the Ld phase (Figures 4.2B). At least fifty vesicles were imaged for each GM1 isoform ins each lipid composition, and phase partitioning of the ganglioside alone or when bound to CTB as a GM1-CTB complex was assigned to be primarily Lo, Ld, or nonpreferential (NPP) by quantitative image analysis as described in Chapter 2. As we expected, we found that phase partitioning of GM1 was lipid composition and ceramide structure dependent. In

---

[g] Parts of this chapter are reproduced from previously published work: Chinnapen, D. J.-F., Hsieh, W.-T., te Welscher, Y. M., Saslowsky, D. E., Kaoutzani, L., Brandsma, E., D'Auria, L., Park, H., Wagner, J. S., Drake, K.R., Kang, M., Benjamin, T., Ullman, M. D., Costello, C.E., Kenworthy, A.K., Baumgart, T., Massol, R.H., Lencer, W. I. (2012) A native lipid-sorting pathway from PM to ER for the unsaturated species of ganglioside GM1. *Developmental Cell*, 23 (3), 573-586.

the absence of crosslinking by CTB, we observed the C12:0-GM1 and C18:0 fluorophore-labeled species displayed no phase preference (NPP) under some conditions or partitioned under other conditions preferentially into the Ld or Lo phases, respectively (Figure 4.2). When these GM1 species were crosslinked by binding CTB, however, both partitioned almost exclusively in Lo domains under all conditions. In sharp contrast, when GM1-C16:1 species crosslinked by CTB, this lipid partitioned almost exclusively in Ld phase. Thus, GM1 with differing ceramides showed distinct phase-partitioning behaviors in GUVs.

The relocation of GM1 before and after CTB binding implied that the crosslinking of GM1 could drive phase partitioning shift from less determined phase preference to exclusively Ld or Lo phases. Interestingly, the phase preference of the GM1-CTB complex appeared to depend mainly on the potential of lipids to be associated with either Lo or Ld phases. C12:0- and C18:0-GM1 had potential to be associated with Lo phase and their CTB complex enhanced partitioning into Lo phase, whereas C16:1-GM1 had unsaturated ceramide and showed partitioning in Ld phase. This finding has implications for receptor activation in cells, which often involves crosslinking of ligands. It is appealing to speculate that the crosslinking of ligands could associate with membrane nanodomains and thus trigger a cascade of downstream reactions.

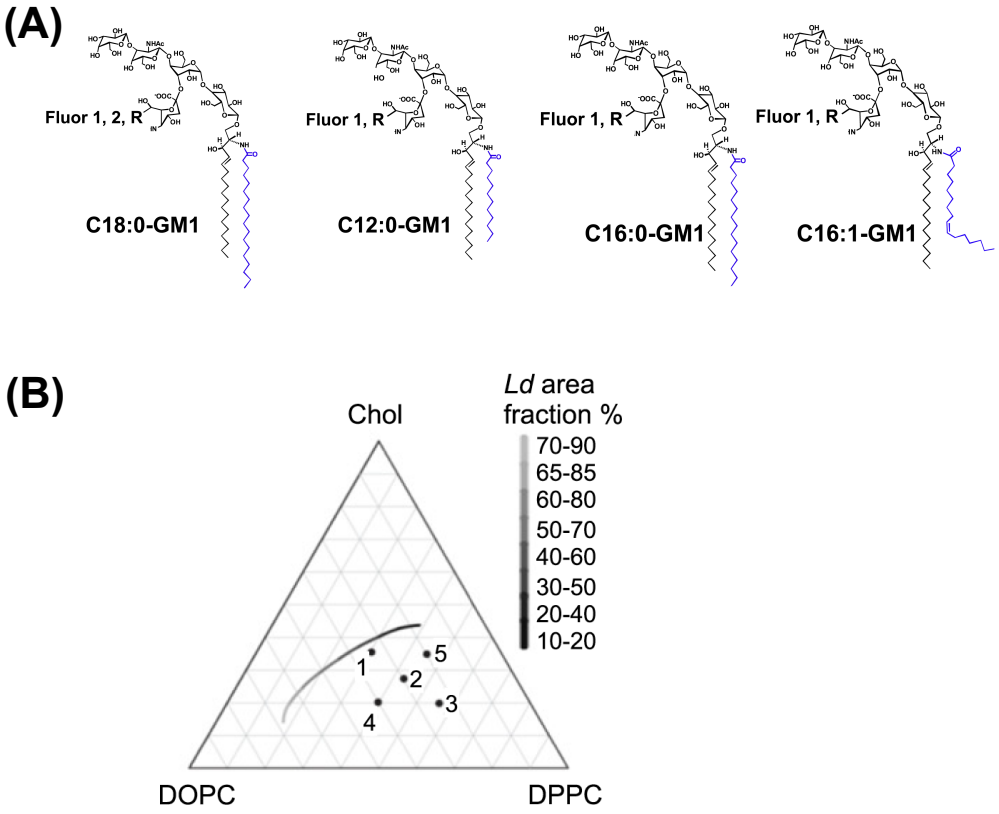

Figure 4. 1 Structures of GM1 variables and lipid compositions in the phase diagram.

(A) Structures of GM1 synthesized, where Fluor 1 and 2 represent Alexa Fluoro 567 and 647, respectively. (B) Partial ternary phase diagram showing the five GUV lipid-compositions, composition 1 to 5, used in these studies. The gray scale line shows the approximate position of a phase coexistence boundary[27,86] and referencing the domain area fraction of the Ld phase[27], which decreases with increasing DPPC content.

(A)

		UNCROSSLINKED		CTB CROSSLINKED		
	DOPC:Chol:DPPC	C12:0-Alexa-568	C18:0-Alexa-568	C16:1/CTB	C12:0/CTB	C18:0/CTB (bovine brain)
1	35:35:30	NPP (NPP/Ld=33/17)	NPP (Lo/NPP/Ld =1/43/6)	Ld	NPP (Lo/NPP/Ld =12/37/1)	Lo
2	30:27:43	Ld (Lo/NPP/Ld =1/19/30)	NPP (Lo/NPP/Ld =10/39/1)	Ld	Lo (Lo/NPP/Ld =38/11/1)	Lo
3	24:20:56	Ld (Lo/NPP/Ld =2/13/35)	Lo (Lo/NPP/Ld =25/19/7)	Ld (NPP/Ld=1/49)	Lo (Lo/NPP=48/2)	Lo
4	40:20:40	Ld (NPP/Ld=15/35)	Lo (Lo/NPP=31/19)	Ld (NPP/Ld=3/47)	Lo (Lo/NPP=37/15)	Lo
5	20:35:45	NPP (Lo/NPP/Ld =1/30/19)	NPP (Lo/NPP/Ld =1/31/18)	Ld (NPP/Ld=8/42)	Lo (Lo/NPP/Ld =26/22/2)	Lo

(B)

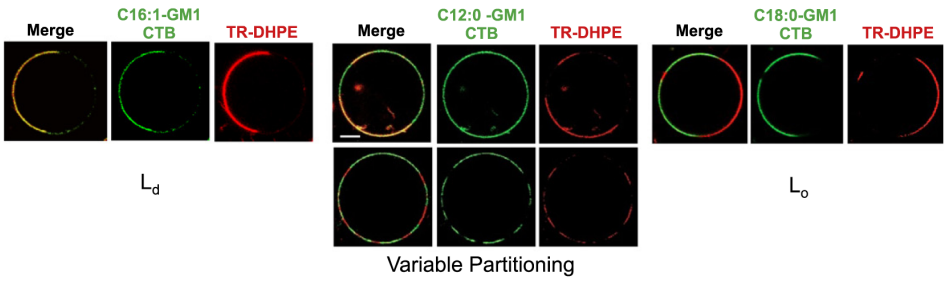

Figure 4. 2 Phase partitioning of GM1 before and after CTB binding.

(A) The summary of phase partitioning of Alexa 568-labeled GM1 and crosslinked GM1-CTB-A488 complexes in GUVs of different lipid compositions. For those compositions which do not show clear phase partitioning, the ratios for the number of vesicles with the observed phases are shown in the parentheses. (B) Representative confocal equatorial images of GUVs with DOPC:Chol:DPPC compositions 1 or 3 (details in (A)), where the red and green fluorescence come from TR-DHPE (marker of Ld phase) and GM1-CTB-A488 complexes, respectively. Left: GUV-composition-1: CTB-C16:1 GM1 complex shows Ld phase preference. Middle (top) GUV-composition-1: CTB-C12:0 GM1 complex shows variable phase partitioning. Middle (bottom) GUV-composition-3: CTB-C12:0 GM1 complex shows Lo phase preference. Right: GUV-composition-1: CTB-C18:0 GM1 complex shows Lo phase preference. Scale bar: 10 μm.

Chapter 5: Examining Curvature-Sensing by a Single Liposome-Based Kinetic Technique

5.1 Curvature-Sensing of Endophilin N-BAR and its Mutants in Equilibrium

To address the question how membrane curvature affects membrane binding kinetics of N-BAR domains (Figure 5.1A), we first set up single liposome curvature assay (SLiC assay)[82] and tested if we could employ this approach to obtain consistent equilibrium constants for Endophilin N-BAR (ENBAR) and its mutants with the values previously reported. We considered the following endophilin mutants: a construct with N-terminal helix deleted (ΔH0), with H1 helix insertion deleted (ΔH1i)[4], and with both H0 and H1i deleted (Ed2).

All experiments were performed on liposomes consisting of 99.8% DOPS (1,2-dioleoyl-sn-glycero-3-phospho-L-serine) and 0.2% DiD (1,1'-dioctadecyl-3,3,3',3'-tetramethylindodicarbocyanine perchlorate). The equilibrium constants were summarized in Figure 5.2, where the equilibrium constants were in line with the reported ones[4,14,17]. Interestingly, Endophilin N-BAR and its mutants all showed binding affinity increased with membrane curvatures, regardless of the presence of helices (the results were further confirmed by Chen Zhu through a second approach, tether-pulling assay)[87]. This finding supported the notion that both scaffolding and helix insertion contribute to curvature-sensitivity of Endophilin N-BAR.

With SLiC approach established, we were then able to follow membrane binding kinetics of proteins on single liposomes (Figure 5.1B). We first demonstrated a curvature-dependence of the membrane association process of ENBAR, while curvature-independence of dissociation process. We then set out to evaluate the contribution from N-terminal helix (H0) by examing ΔH0. We found that both association and dissociation processes of ΔH0 were independent of curvatures.

5.2 Curvature-Sensing of Endophilin N-BAR and its H0 Helix-Deleted Mutant in Membrane Association and Dissociation Processes

Membrane association was initiated by injection of proteins into tethered vesicles chamber; dissociation process was measured via TIRF-FRAP approach[75]. Protein association binding kinetics on a single vesicle was fitted as a single exponential growth, $I = A\ (1\text{-}\exp(\text{-}k_{obs\text{-}a}t) + I_0$. By plotting observed association rate constants ($k_{obs\text{-}a}$) with respect to vesicle sizes, curvature-dependence was shown given that smaller vesicles displayed faster rates compared to larger ones (Figure 5.3A). In contrast, observed dissociation rate constants ($k_{obs\text{-}d}$) from TIRF-FRAP showed a scattered distribution with respect to vesicle diameters (Figure 5.3B). Constant $k_{obs\text{-}d}$ obtained at different protein concentrations suggested first-order process in the reaction-limited regime, resulting in the fact that $k_{obs\text{-}d}$ can be interpreted as an apparent dissociation rate constant[75]. Assuming the membrane binding follows a simple reaction model, P+V↔PV, with k_{on} and k_{off} as forward and reverse rate constants, respectively, in the condition where protein

concentration is much higher than lipid concentration, the relation between observed association rate constant and protein dissociation and association rate constants can be shown to follow $k_{obs\text{-}a} = k_{on}[P] + k_{off}$ (pseudo first order approximation) Based on the fact that $k_{obs\text{-}a}$ was curvature-dependent (Figure 6A) and that k_{off} equal to $k_{obs\text{-}d}$ was curvature-independent, we hypothesized that k_{on} is also curvature-dependent. One explanation for this dependence is that smaller vesicles have higher density of packing defect for N-terminal helix insertion compared to larger ones. To test this hypothesis, binding kinetics of the ΔH0 mutant was determined. The results suggested curvature-independence of kinetics (Figure 5.3C and D) for both association and dissociation processes. Taken together, results obtained from kinetics measurements suggested curvature sensitivity of ENBAR was mainly contributed from faster association to curved membranes. Removal of H0 helix abolished curvature dependence of association process, which highlighted the dominant role of H0 helix in identification of lipid packing defects, supporting previous experimental[14,82] and theoretical[39] works.

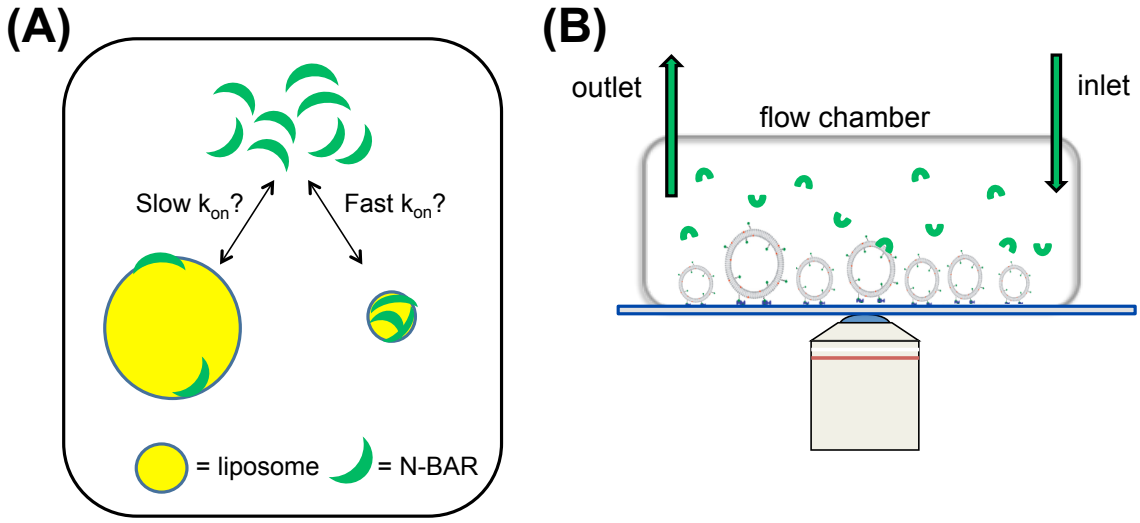

Figure 5. 1 Research scheme and experimental setup for single liposome-based kinetics measurement.

(A) Research scheme delineates the question how membrane curvature affects membrane binding kinetics of N-BAR domains. (B) To obtain varied membrane curvature and at the same time have easy access to time-resolved characterization, we combine a flow-based system and the recently developed tethered vesicle assay of Stamou et al[82]. We fabricated micro-flow chambers which only require small amounts of protein usage. Our system allows programmable injection of lipid vesicles and proteins. With this approach, we can follow membrane binding kinetics of proteins on single liposomes. Furthermore, membrane curvature information can be obtained from an analysis of fluorescence from lipid vesicles.

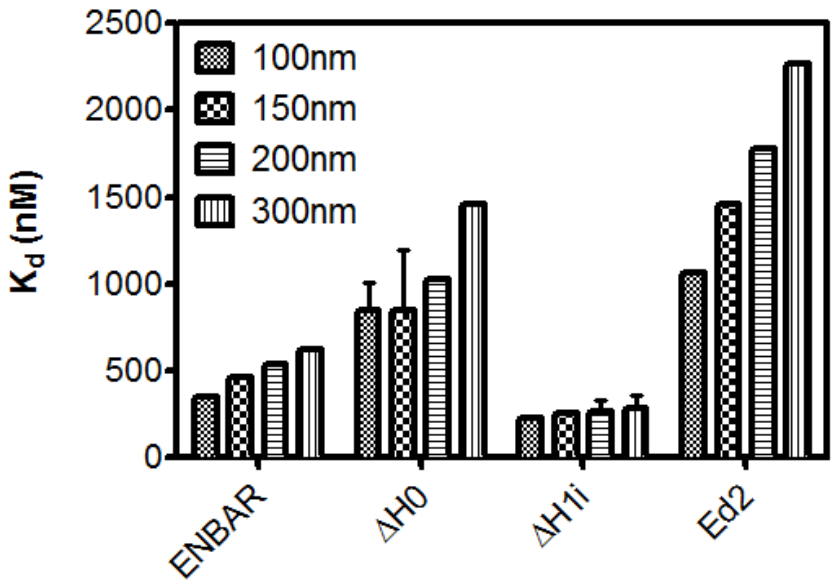

Figure 5. 2 Equilibrium constants for Endophilin N-BAR and its mutants.

Experiments were performed through SLiC assay on the polydisperse liposomes consisting of 100%DOPS and trace amount of fluorescent probe, DiD. The average diameters of liposome were first determined from dynamic light scattering, which was then correlated with the average fluorescence intensity of DiD and gave diameters of single liposomes (see Chapter 2 for details). Error bars represent standard deviations from three independent experiments.

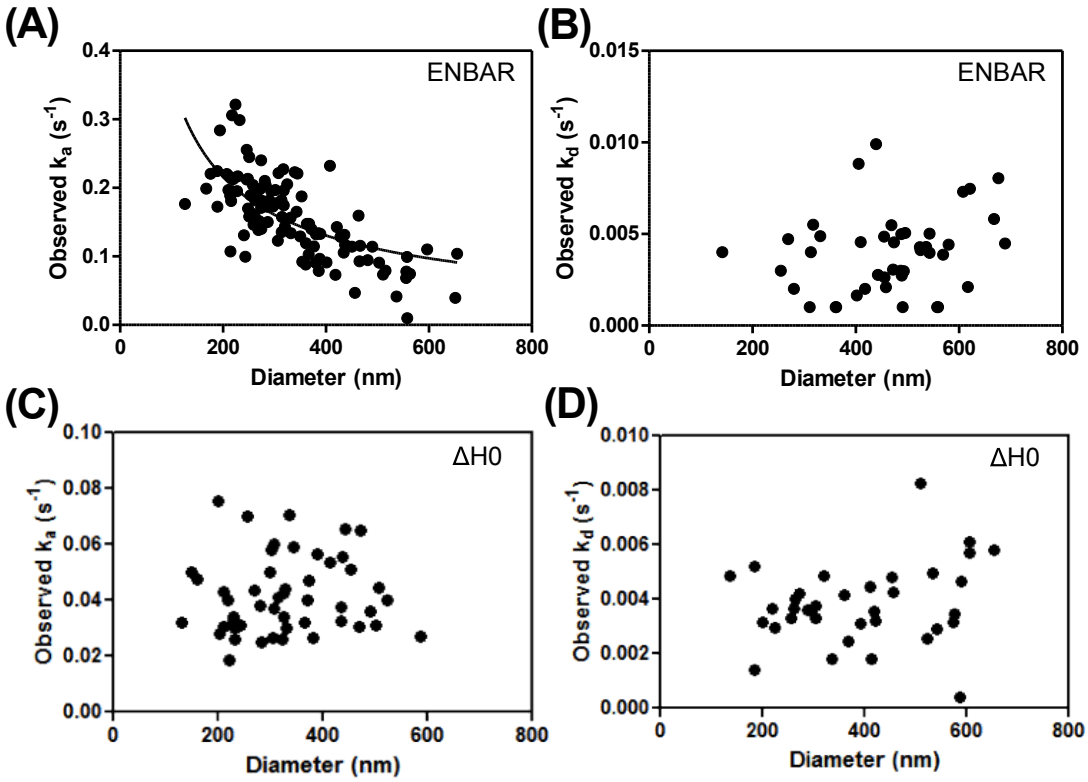

Figure 5. 3 Membrane binding kinetics of Endophilin N-BAR and its H0-deleted mutant.

Representative data measured through single liposome-based kinetic technique. Observed association (A) and dissociation (B) rate constants with respect to membrane curvatures for Endophilin N-BAR at concentration of 100 nM. Observed association (C) and dissociation (D) rate constants with respect to curvatures for ΔH0 at concentration of 100nM. The black line in (A) represents fitted curve with power law.

Chapter 6: Line Tension of Membrane Domains

6.1 Line Tension-Related Phenomena

Line tension has been widely explored at three-phase contact line of bulk phases[88–93]. One representative example containing three-phase contact line is a liquid droplet residing on solid surface surrounded by a gas phase. Line tension has also been found in two surface phase contact systems[88,90], where it is termed "boundary tension." Line tension occurring in two separated phase contact systems has been experimentally studied in polymers[94–97] and surfactants[98] monolayers. Line tension has also been investigated in biomembrane model systems including lipid monolayers[54,99–101] and bilayers[78,102–105]. Note that lipid bilayer line tension arises at the boundary between phase-separated lipid domains in otherwise continuous membranes and at membrane edges (pores). We focused here on the former phenomenon.

6.2 Line tension determination in biomembrane model systems

Methods of determining line tension at domain boundaries have previously been developed experimentally[54,78,95,100–103,106–110] and theoretically[111–113]. One of experimental monolayer line tension measurements is based on the fact that domains relax from deformed shape to circular shape when external perturbation is removed. Applied external perturbation, including flow shear[95,99,106] and optical tweezers[110], deform circular domains to ellipse-like shape or bola shape in monolayer. When the distortion is

removed, deformed domains relax to circular shape with a rate depending on line tension and viscosity of Langmuir film and underlying subphase[114].

Shape analysis of GUVs could also yield line tension[109,115]. Line tension has been examined by analyzing nucleation rate via atomic force microscopy[108]. Tian et al. recently measured line tensions of values via micropipette aspiration of dumbbell-shaped vesicles[103]. Another method relies on Fourier power spectra of thermal domain boundary fluctuation, observable near critical point. The mean-squared powers of each undulated mode can be related to line tension[54,55,78,101,102,116,117]. Theoretical models have related line tension to lipid phase height mismatch, spontaneous curvature, lateral tension, and elastic moduli[111,112]. Thermodynamic mean field model has also been developed to predict line tension[118].

6.3 Review of Line Tension Theories

To elucidate line tension along membrane domain boundaries, theoretical models for free energy of lipid membrane in terms of mechanical (e.g. elastic moduli of lipids) or chemical parameters (e.g. intermolecular forces between lipids) have been constructed[111–113,119–123]. For the former, free energy cost comes from the elastic deformation of the membrane. It has been proved experimentally that liquid ordered domains are thicker than liquid disordered domains in lipid systems with fluid phase coexistence[124–126]. If the orientation of the lipid is the same for both raft and the surroundings, the mismatch

between these two phases will result in a hydrophobic region exposed to water[111,112,127–129]. This step-like region is postulated to be smoothed out by the membrane deformation[111,112,119] (top panel in Figure 6.1). The fundamental deformation mechanisms include three main types, tilt, splay, and area compression[130]. Due to the much higher energy cost on area compression[111], it is suggested that lipids should deform mainly through tilt and splay, and little through area compression. With the assumption on bilayer model composed of two symmetric monolayers, line tension (γ) is yielded as a function of membrane splay elastic modulus (B), tilt modulus (K), and spontaneous curvature (J) (see detailed derivation in ref[111] and references therein):

$$\gamma = \frac{\sqrt{B_s K_s B_r K_r}}{\sqrt{B_r K_r} + \sqrt{B_s K_s}} \frac{\delta^2}{h_0^2} - \frac{1}{2} \frac{(J_s B_s - J_r B_r)^2}{\sqrt{B_r K_r} + \sqrt{B_s K_s}} \tag{6.1}$$

where s and r subscript indicate surrounding and raft, respectively; δ is the height mismatch between the two phases; $h_0 = (h_s + h_r)/2$, where h_s and h_r are the equilibrium thickness of surrounding and raft. This model quantifies the condition for raft formation and reveals how elastic parameters control domain coalescence.

Instead of expressing line tension by mechanical deformation, Brewster et al. considered the effective intermolecular interaction between the saturated and unsaturated lipids (bottom panel of Figure 6.1) and used mean-field approximation for the lattice populated with saturated and unsaturated lipids[113]. From their model, they demonstrated how hybrid lipids can act as line tension-active lipids to stabilize domain boundary.

Theories of domain line tension on Langmuir lipid monolayers have also been examined at a continuum level[55,56,99,131] and a molecule-scale level[107]. The shapes and sizes of domains in Langmuir monolayers are mainly regulated by two opposing forces, line tension acting at the domain boundary and dipole-dipole electrostatic repulsions between and within coexisted phases. Line tension minimizes the length of the interface thus favoring circular domains, while electrostatic repulsions oppose domain coalescence thus favoring noncircular domains. Note that the latter effect is absent in bilayer system due to the symmetry of the bilayer system. The following two sections demonstrate how we determined line tension of fluctuating domains on lipid monolayers and GUVs. In lipid monolayer section, experimental results based on Goldstein and Jackson's[55] and Lee and McConnell's[56,132] theories were examined.

6.4 Domain Fluctuation in Langmuir Monolayer: Comparison between Goldstein-Jackson and McConnell-Lee Theories

Competition between electrostatic force and line tension results in the domain shape fluctuations in lipid monolayer. McConnell and Lee examined critical domain radii at which domain becomes instable with respect to *n*-fold symmetry distortion[56,132] (ML theory). In parallel to their work, Goldstein and Jackson applied their approach in magnetic fluids to fluctuation spectrum for domain fluctuation in lipid monolayer (GJ theory).

To investigate line tension at domain boundaries, fluctuating domain shape is decomposed into Fourier series as a function of domain radius (R_0) and polar angle (θ):

$$R = R_0 + \sum_n \zeta_n \cos n\theta \tag{6.2}$$

The excess energy of the phase boundary (relative to a non-fluctuating domain) can thus be written up to the quadratic order in mode amplitude (ζ_n)

$$\Delta E_n = \frac{1}{2}\Omega_n \zeta_n^2 \tag{6.3}$$

where Ω_n is a restoring force constant which is related to the line tension (γ) and difference in dipole density (μ) between coexisting phases.

Goldstein and Jackson expressed the force constant as:

$$\Omega_n = \frac{\pi\gamma}{R_0}\beta_n \tag{6.4}$$

$$\text{where } \beta_n = [1 - \frac{1}{2}N_B \ln(\frac{8R_0}{eh})](n^2 - 1) - \frac{1}{4}N_B(1 - 4n^2)\sum_{j=2}^{n}\frac{1}{2j-1} \tag{6.5}$$

and h is the thickness of the monolayer film. Bond number, N_B, is a dimensionless parameter defined as the ratio between dipole density difference and line tension, $2\mu^2/\gamma$.

An alternative expression for the force constant by Stone and McConnell[133] is

$$\Omega_n = \frac{\pi\mu^2(n^2-1)}{R_0}\ln\frac{R_n}{R_0} \tag{6.6}$$

$$\text{where } R_n = \frac{e^{Z_n}\Delta}{8}e^{\gamma/\mu^2} = \frac{e^{Z_n}\Delta}{8}e^{2/N_B} \tag{6.7}$$

Here, R_n is domain radius above which domain becomes instable with respect to the transition to the *n*-fold symmetry shape[56]. Z_n is the exponent independent of physical variables and the values and the derivation can be found in McConnell 1990[132] and Lee and McConnell 1993[56]. Δ is the separation distance between adjacent dipoles, and thus can be determined from area-surface pressure isotherms. In order to provide a comparison between the two theories, N_B from GJ theory is incorporated into eq. 6.7.

The restoring force constants in eq. 6.4 and 6.6 define the condition for the stability of circular ground-state shape toward the transition to ground states of n-fold symmetry. With increasing Bond number, the first instable mode is found for *n*=2; therefore, we can find the critical Bond number beyond which the circular domain becomes instable is (eq. 6.8-1 for GJ theory and eq. 6.8-2 for ML theory):

$$N_B^*(2) = \frac{2}{\ln(8R_0/h) - 11/6} \tag{6.8-1}$$

$$N_B^*(2) = \frac{2}{\ln(8R_0/\Delta) - Z_2} \tag{6.8-2}$$

where Z_2 is 10/3. Note that the results examined in this Chapter were from the stable circular domains with N_B values below the critical Bond number defined in eq. 6.8.

From eq. 6.3, 6.4 and 6.6, together with the assumption of thermal equipartitioning, an energy of 1/2 k_BT per fluctuation mode, and Fourier expansion for $\zeta_n = a_n + ib_n$ in ref[54,78], the expression for the mode amplitude is yielded as

$$< \zeta_n^2 >= \frac{2k_BTR_0}{\pi\gamma\beta_n} \tag{6.9-1}$$

$$< \zeta_n^2 >= \frac{2k_BTR_0}{\pi\mu^2\alpha_n} \tag{6.9-2}$$

where $\alpha_n = (n^2 - 1)\ln(\frac{R_n}{R_0})$ (6.10)

For comparison between two theories, we used the experimental data acquired from the composition of 30 mol% dihydrocholesterol (DChol) and 70 mol% 1,2-dimyristoyl-*sn*-glycero-3-phosphocholine (DMPC) doped with 0.5 mol% rhodamine labeled 1,2-dihexadecanoyl-*sn*-glycero-3-phosphoethanolamine. The film thickness (h) was assumed to be constant (10 angstrom) for various surface pressures[54], for which we benefited from the fact that the values for γ and μ do not depend sensitively on film thickness[55]. The separation distance between dipoles (Δ) can be obtained from the surface pressure-area isotherm and thus depended on the surface pressure investigated. By the

image processing method described in Chapter 2 (2.6), we were able to fit the dimensionless ratio β_2/β_n (or α_2/α_n) to the experimentally determined mode power ratios $<\zeta_2^2>/<\zeta_n^2>$ by varying fitting parameter, N_B. N_B was then plotted with respect to n_{max} in the mode sets $[n] = [2,\ldots, n_{max}]$, and the largest mode set prior to drop-off in the magnitude of N_B was taken for further analysis. From the linear fit of $<\zeta_n^2>$ to $1/\beta_n$ (eq. 6.9.1) or $1/\alpha_n$ (eq. 6.9.2), γ_{GJ} (γ in GJ theory) or μ_{ML} (μ in ML theory) can be determined, which then gave value of μ_{GJ} or γ_{ML} from N_B.

Figure 6.2 showed μ^2 and γ with respect to surface pressure by GJ and ML theories. Both methods demonstrated decreasing μ^2 and γ with increasing surface pressure. However, γ from ML has systematically smaller value (16% as an average from mode number 3 to 15) than that from GJ. Compared to γ, μ^2 in ML is more consistent (within ± 5%) with that from GJ. To obtain more insight, we examined to what extent additional parameters contribute to these differences.

First, we evaluated the contribution from domain radius. Results of small domain with radius of 6.28 μm and large domain with that of 12.07 μm at surface pressure of 8 mN/m were demonstrated in Figure 6.3. For both domains, μ^2 was consistent between two theories (within ±8% for large one; ±11% for small one). As for γ, ML theory showed lower values compared to those of GJ theory: an average of mode number 3 to mode number 15 gave 12% and 15% for large and small domains, respectively. Corresponding to these results, larger N_B (14% for large and 15% for small domain) from ML theory was

also observed. Systematic comparison on line tension as a function of radius is displayed in Figure 6.4, where $(\gamma_{GJ}-\gamma_{ML})/\gamma_{ML}$ against radii was plotted and no clear trend is observed in the radii under investigation (from 6 to 12 μm). To see if the film thickness (h) in GJ and separation distance (Δ) in ML theory affects this deviation, mode power spectra with fixed domain radii and Bond number were displayed in Figure 5. For the surface pressure range we investigated, Δ increases from 10.33 angstrom in 9.685 mN/m to 10.51 angstrom in 7.83 mN/m. This small range only contributes overall 0.4% difference in mode power spectra. Therefore, we set out to investigate variation of the parameter, h, from 1 to 3 nm (Figure 5a), and R_0, ranged from 4 to 6 μm (Figure 5b). We found that with increasing h or decreasing R_0, mode power ratios from GJ theory approached those from ML theory. Together with that R_0 was determined from experiments, while h was assumed as 1 nm in our analysis, this comparison suggests the sharp cutoff, h, is the main parameter that contributed to the variations in line tension and dipole density difference obtained from two theories.

6.5 Domain Fluctuation in GUVs

By means of fluid domain flicker spectroscopy, we next examined line tension of domain between Lo and Ld phases in GUVs with lipid mixture of molar ratio of DiPhyPC (1,2-diphytanoyl-*sn*-glycero-3-phosphocholine)/ DPPC (1,2-dipalmitoyl-sn-glycero-3-phosphocholine) / Chol (cholesterol) = 25:20:55, mixture for which the phase diagram has been determined[134]. Line tension (γ) of each mode was obtained by thermal

energy equipartitioning (eq. 6.11). Note that this equation is equivalent to eq. 6.9.1 with μ=0 (thus $N_B = 0$) in β_n. According to the principle that mode amplitude follows Gaussian distribution in equipartitioning theorem[68], $P_n(|u_n|) \propto \exp(-(\gamma\pi R_0(n^2-1)|u_n|^2 / k_B T))$. The variance for this Gaussian is given by eq. 6.11:

$$< |u_n|^2 >= \frac{2k_B T}{\gamma\pi R_0(n^2-1)} \tag{6.11}$$

Figure 6a to 6d showed mode power distribution for the mode 2 to 5, which can be well fit by exponential decay. By linear fit of the plot of the variance versus $1/(n^2\text{-}1)$, the line tension can then be obtained (Figure 6.6E).

In previously published work by Esposito et al.[78], it was found that the line tension of domains increased with the illumination time in GUVs composed of DOPC/DPPC/cholesterol mole ratios of 1:1:1, which might be caused by photo-induced lipid decomposition through an unknown mechanism[135]. In this contribution, we found that the replacement of DOPC with DiPhyPC reduced dramatically the effect of photo-induced lipid decomposition on line tension due to the saturation of acyl chains in DiPhyPC. However, the photo-effect was not completely avoided and the use of neutral density filters was still recommended to slow down photo-oxidation. Interestingly, in the case of DiPhyPC containing compositions, we observed that the line tension was gradually decreased with time (Figure 6.7A). This behavior was opposite to what was

previously observed in DOPC containing compositions[78], where line tension was observed to increase significantly during illumination (Figure 6.7B). This effect was easily detected at the critical points where patterns were highly sensitive to compositional changes (Figure 6.7B): in the case of DOPC containing patterns evolved quickly into larger domains, whereas DiPhyPC containing patterns slowly shrank to the fractal.

6.6 Factors Influencing Line Tension

To elucidate how the size and morphology of membrane domains are modulated, the factors that might affect line tension have received considerable interests[95,96,113,118,136,137]. In-depth analysis on this aspect does not only provide physic chemistry insight, but also give us hints on how proteins or/and various lipids regulate membrane domains in vivo.

6.6.1 Critical point

Line tension decreases when approaching critical points, where phase coexistence disappears. The relationship between the line tension and critical point follows eq. 6.12 for GUVs and eq. 6.13 in Langmuir monolayers, where T and π indicate temperature and surface pressure, respectively; subscript c indicate critical point; critical exponent ν is equal to 1 for both cases.

$$\gamma = m(T_c - T)^{\nu} \tag{6.12}$$

$$\gamma = m(\pi_c - \pi)^{\nu} \tag{6.13}$$

6.6.2. *Linactants*

Results from experiments, simulation[138], and theoretical calculation suggest proteins[136,137], hybrid lipids[113,118], oxidative product from cholesterol[100], and amphiphiles bearing two different functional group or chain length at tails[138] can reduce line tension. In analogy to surfactants as surface-active agents at oil-water interfaces, these line active agents are proposed to be termed as "linactants"[95,139]. Trabelsi et al.[95] found that semifluorinated phosphonic acid (phosphonic acid with hydrophobic chains composed of hydrocarbon and fluorocarbon blocks) reduced line tension between hydrocarbon-rich (pentadecanoic acid-rich) and fluorocarbon-rich (perfluoroundecanoic acid-rich) phases in Langmuir monolayer: for more efficient single-tailed linactant, it could reduce line tension by 20% at a mole fraction of 8×10^{-4}. They further investigated line-activity efficiency dependence on molecular structures[26], and found longer hydrophobic chains and longer fluorocarbon blocks are more efficient linactants.

Peptides also act as linactants. Nicolini et al. investigated the association of fluorescent lipidated N-Ras protein in lipid domains, and found an interfacial adsorption at the boundary between Lo and Ld phases[136], as might lead to line tension decrease. Antimicrobial peptides, e.g. Bax-derived peptide[136] and magainin2[140], are common in lipid/protein pore formation at pathogens' membranes. The induction of pores results in

bilayer-pore interline, where the line tension might be reduced by releasing stress of curvature[136].

Theoretical models developed by Brewster et al. suggested that hybrid lipids, with one saturated chain preferring to partition in the ordered phase and one partially unsaturated chain preferring to partition in the disordered phase, can act as a linactant[44]. They further investigated how the molecular interaction, the molecular volume, and area per head group determined the domain size, and found that domain size increased with cholesterol concentration[51]. Simulation work by Schäfer et al. indicated that hybrid saturated/unsaturated chain lipids and cone-shaped lysolipids partitioned at domain boundaries and can lower the line tension[138].

Motivated by the features of linactants mentioned above and the references related to the mechanical parameters which would affect line tension, we investigated the line activity of phospholipids with cone shape, diacylglycerol (14:0 DG, 1,2-dimyristoyl-*sn*-glycerol, abbreviated as DAG), in monolayer consisting of 30%Chol and 70%DChol. In cell, diacylglycerol is the product from the hydrolysis of phosphatidylinositol 4, 5-biphosphate (PIP2), serving as a second messenger signaling lipid[141]. The results in Figure 6.8 indicated that increasing percentage of DAG decreased line tension. Together with previous simulation work by Schäfer et al.[138], this finding suggested that both inverted cone-shaped (DAG in this contribution) and upright cone-shaped (lysolipids in Schäfer et al.'s work) lipids could decrease line tension. One possible mechanism could

be that the cone-shaped lipids are attracted to the domain boundary to minimize the energy cost due to thickness mismatch between phases[138]. Note that the transition pressure was determined to be constant under all DAG concentrations investigated. This observation has implications for the potential function of DAG in reducing line energy of clusters in vivo. Motivated by the effect of DAG on line tension, we examined the fluorescent lipid, Texas Red dihexadecanoyl-sn-glycero-3-phosphoethanolamine (TR-DHPE), which has been widely used as a fluorescence marker in model membrane systems. The head group of Texas Red moiety renders TR-DHPE inverted cone-shape. Interestingly, we observed that the presence of TR-DHPE had opposite effect on line tension compared to DAG. Furthermore, it was observed that the transition pressure increased with the increasing percentage of TR-DHPE (+1.4 mN/m for TR-DHPE at 1 mol%), which suggested that the phase boundary was shifted by TR-DHPE. Indeed, the previously published work by Veatch et al.[142] also revealed that the presence of fluorescent probe, DiC12[h], had a significant increase (+6 C° for DiIC12 at 0.5 mole%) on miscibility transition temperature in GUVs composed of 1:1 DOPC/DPPCd62 and 30%Chol. This finding suggested that the inclusion of fluorescent probes might alter

[h] DiIC12 is the abbreviation of the fluorescent probe, 1,1'-didodecyl-3,3,3',3'-tetramethylindocarbocyanine perchlorate.

composition of coexisting domains, resulting in changes in phase boundaries and interfacial energy.

6.7 Summary

In this Chapter, we have reviewed current approaches on measuring line tension and theoretical models for line tension at lipid domain boundaries. The comparison of the line tension and dipole density difference obtained by Goldstein-Jackson and McConnell-Lee theories suggested the more accurate thickness of lipid monolayer can be deduced by correlating the results from both theories. We have also found that line tension can be modulated by trace amount of diacylglycerol and Texas Red-DHPE.

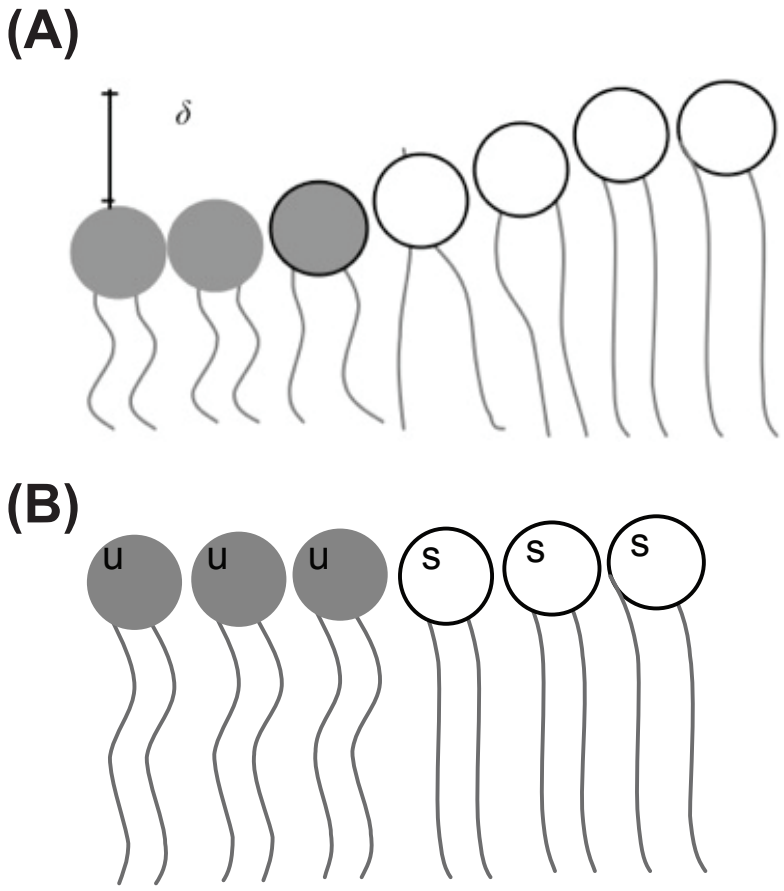

Figure 6. 1 The schematic membrane cross-section.

The cartoon demonstrates the models from (A) mechanical aspect: membrane deforms through the lipid splay or tilt to smooth out the height mismatch between raft and surrounding; (B) chemical aspect: the intermolecular interactions between and within saturated and unsaturated lipid phase determine the line tension along phase boundary.

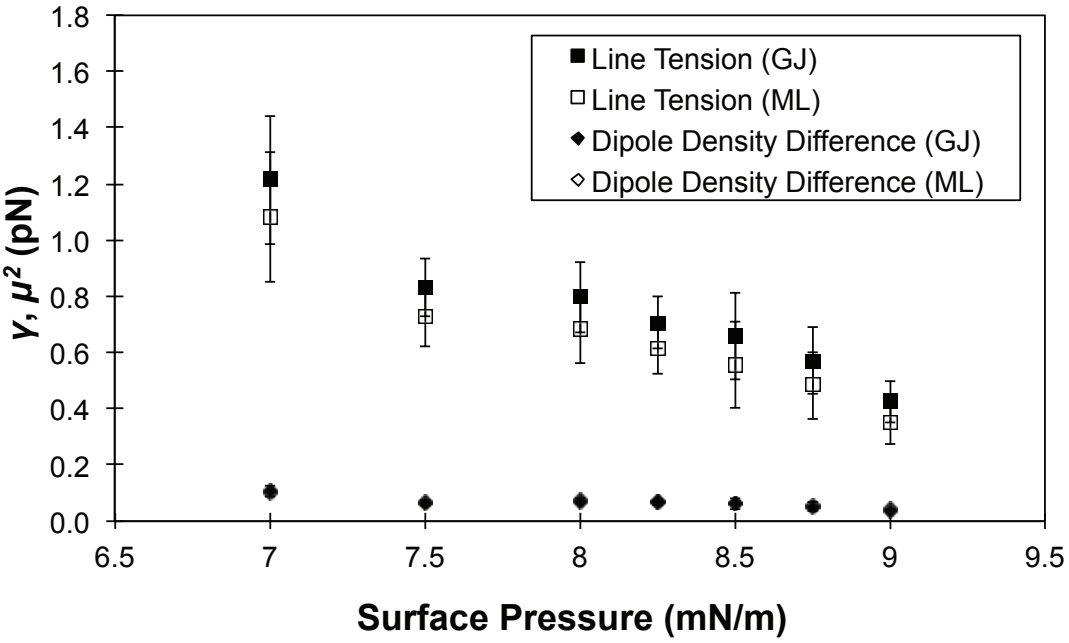

Figure 6. 2 Line tension and dipole density difference from GJ and ML theories.

Line tension and dipole density difference were obtained from the composition of 30 mol% DChol and 70 mol% DMPC from surface pressure of 7 to 9 mN/ m in Langmuir monolayer. Each point is analyzed from at least five different domains. For each surface pressure, several > 2000-frame movies are obtained. Individual domain is then tracked frame by frame, followed by trace analysis, from which $<\zeta_n^2>$ can be obtained.

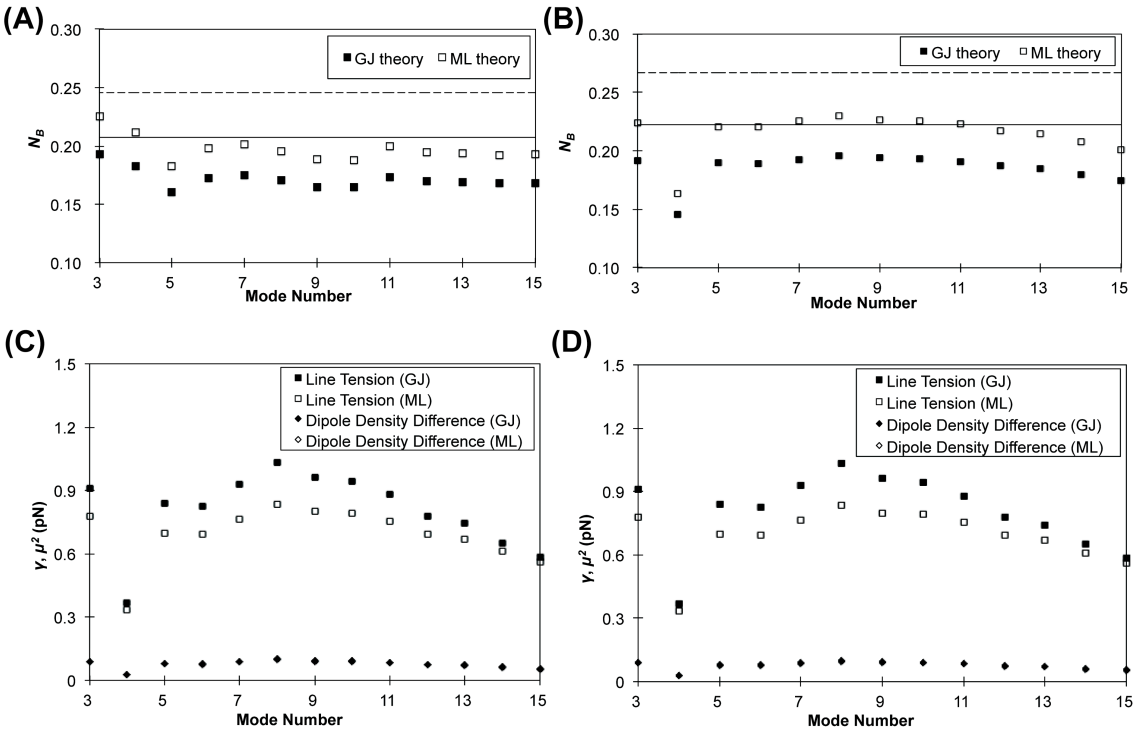

Figure 6. 3 N_B, γ, and μ^2 from mode number 2 to 15 from Goldstein-Jackson and McConnell-Lee theories.

Bond number (A, B), line tension, and dipole density difference (C, D) for domain radii of 12.07 μm (A, C) and 6.28 μm (B, D) at mode number from 2 to 15. (A, B) Dashed and solid straight lines in A and B represents $N^*_B(2)$ (see eq. 6. 8) from ML and GJ theories, respectively. (C, D)

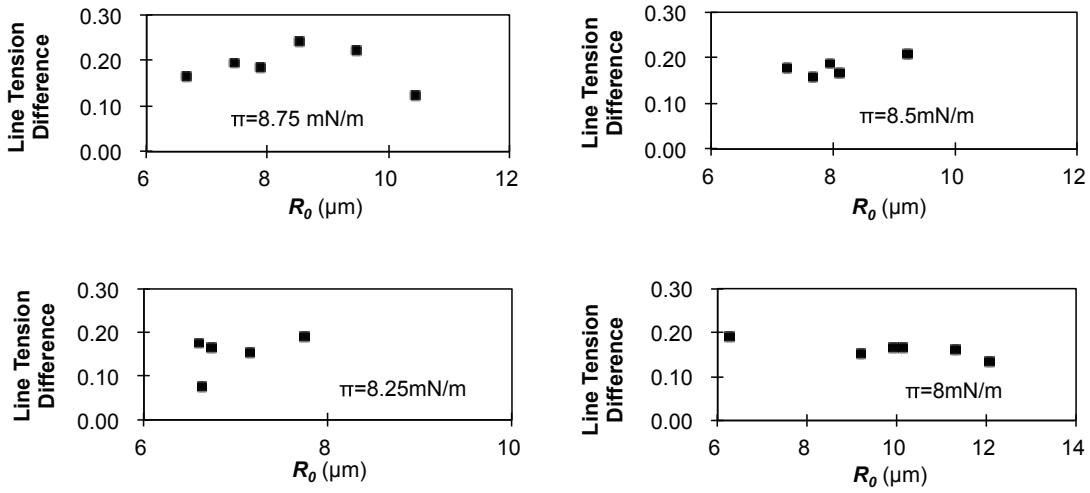

Figure 6. 4 Domain radius shows negligible contribution to the line tension difference from Goldstein-Jack and McConnell-Lee theories.

In order to evaluate the effect of radius on the comparison between GJ and ML theories, line tension difference, $(\gamma_{GJ}-\gamma_{ML})/\gamma_{ML}$, is plotted against domain radii at different surface pressure (π).

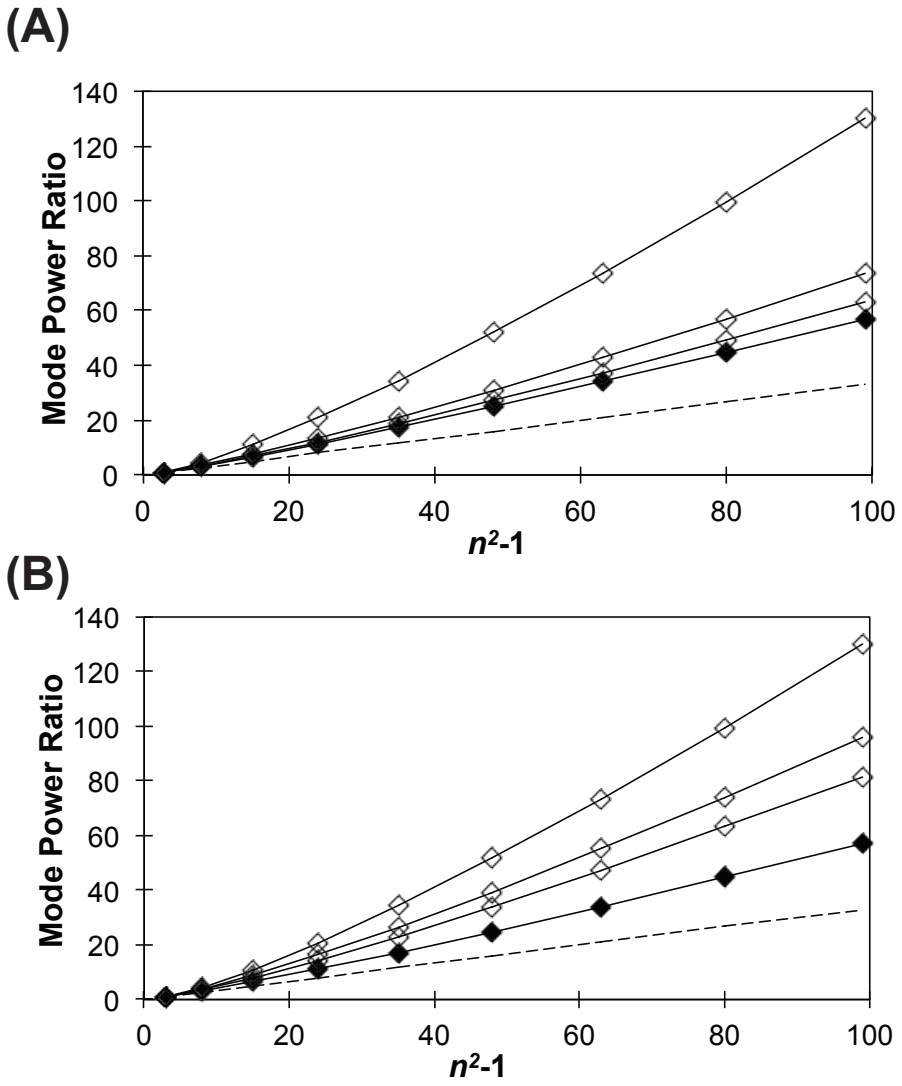

Figure 6. 5 Mode power ratio, $<\zeta_2^2>/<\zeta_n^2>$ against mode number index.

(A) Mode power ratio dependence on h: for ML theory (black diamond; R_0 = 6.53 μm, N_B = 0.21, Δ = 1 nm) and GJ theory (white diamond; R_0 = 6.53 μm, N_B = 0.21, h = 1, 2, and 3 nm from top to bottom). (B) Mode power ratio dependence on R_0: for ML theory (black diamond; R_0 = 6.53 μm, N_B = 0.21, Δ = 1 nm) and GJ theory (white diamond; N_B = 0.21, h = 1 nm, R_0 = 6.53, 5, and 4 μm from top to bottom). The black dashed line indicates the condition without dipolar interactions.

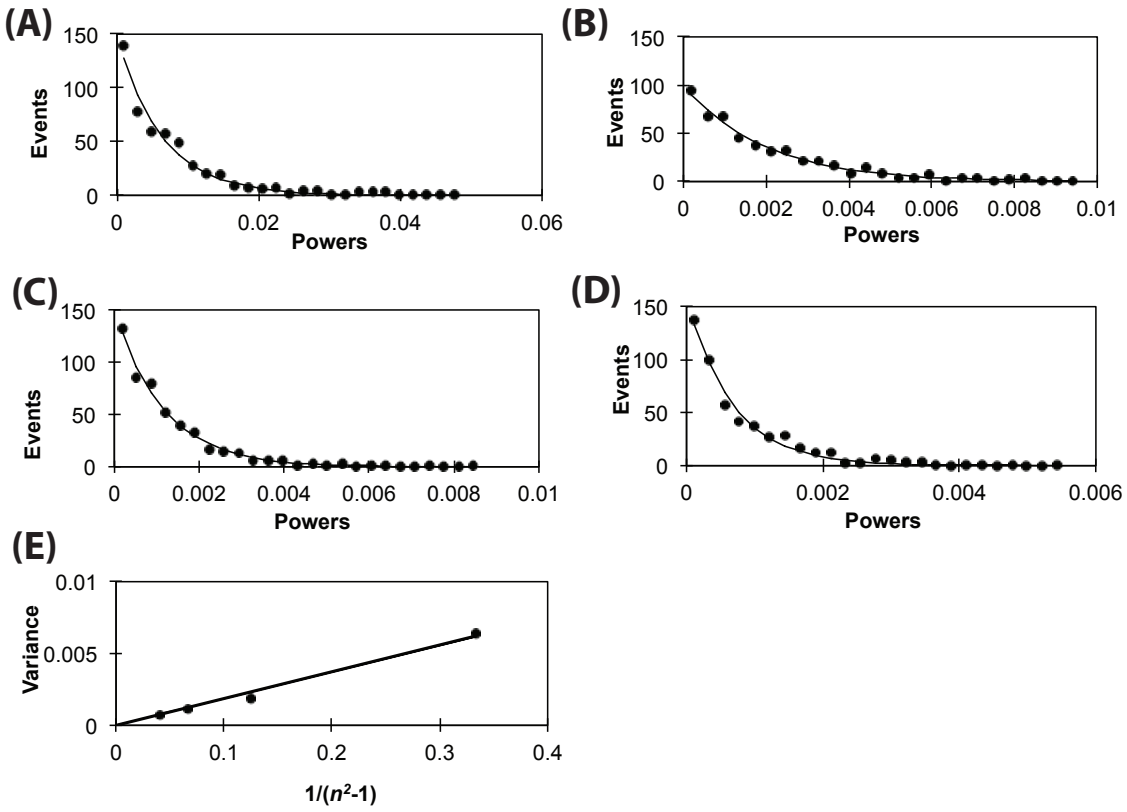

Figure 6. 6 Fourier mode power probability distribution analysis of a fluctuating domain.

Fourier mode power probability distribution analysis of a fluctuating domain with a radius of 4.05 μm at 23.6°C in GUV. (A-D) Probability distributions of mode powers from mode number (n) 2 to 5 are well fit by an exponential decay, indicating an underlying Gaussian distribution of mode amplitudes. (E) The plot of the distribution width (variance) in (A) to (D) versus 1/ (1-n^2). The slope is related to line tension (see eq. 6.11); in this experiment, line tension of 0.56 pN is obtained.

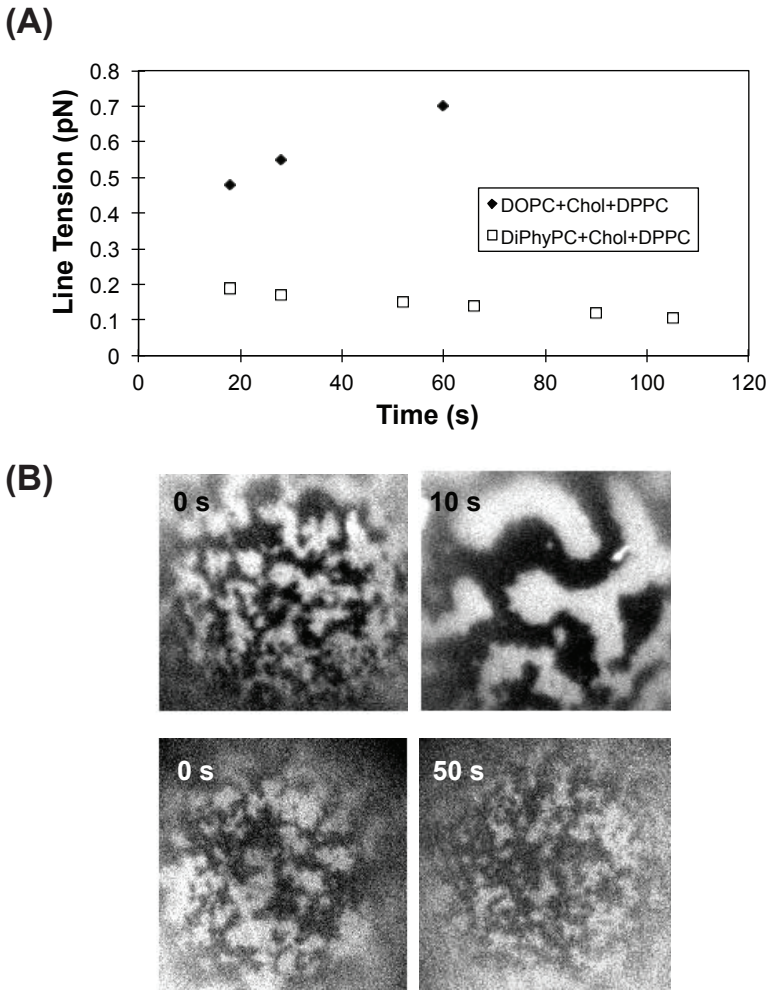

Figure 6. 7 Photo-oxidation effect on fluctuating domains.

(A) Line tensions measured in a single domain for two different compositions are plotted against observation time. Vesicles were illuminated continuously, and every 500 frames were analyzed to obtain an averaged line tension for that interval. Line tension is observed to increase with time for domain in DOPC containing GUV (DOPC:Chol:DPPC= 33:37:30, solid diamond) and slowly decreases against time for that in DiPhyPC containing GUV (DiPhyPC:Chol:DPPC=28:50:22, open squares. Both compositions were doped with 0.2 mol% Texas Red-DPPE. (B) Snapshots of domain shapes for two compositions in different time points.

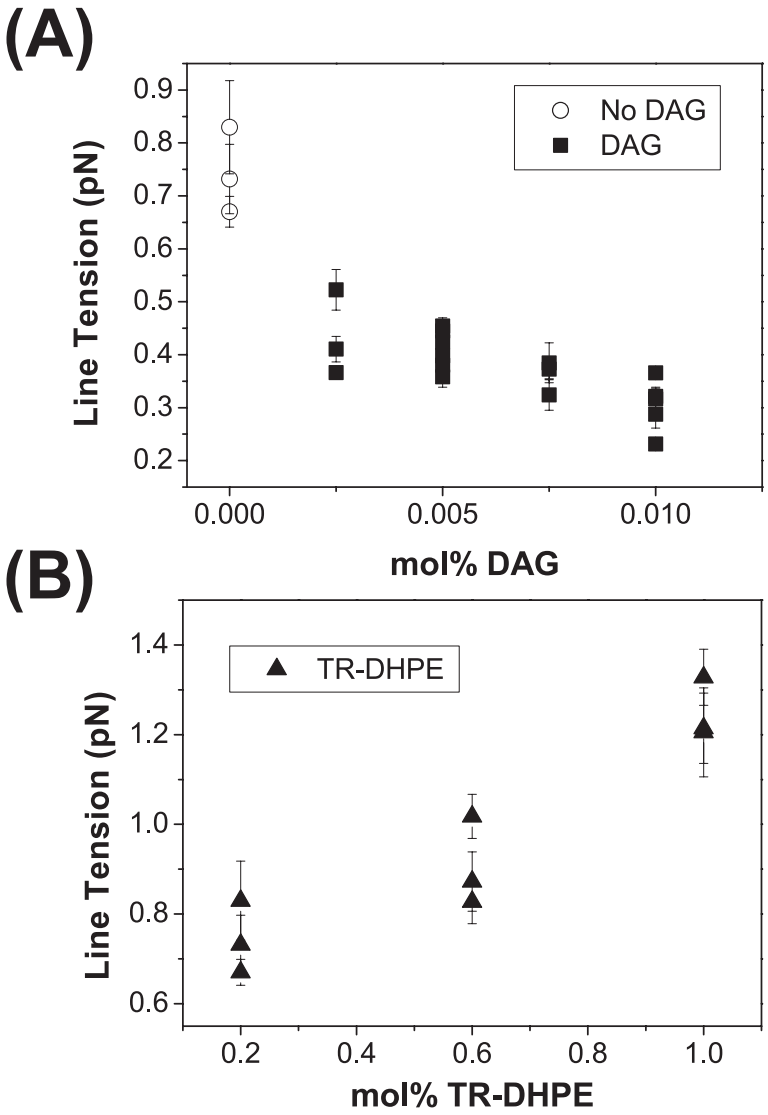

Figure 6. 8 Effect of the presence of linactants to the line tension.

(A) The increasing percentage of DAG was observed to decreases the line tension of domains. Lipid composition: 30%DChol, (69.8-X)%DMPC, 0.2%TR-DHPE, and X% DAG. (B) The increasing percentage of TR-DHPE was found to increase the line tension of domains. Lipid

composition: 30%DChol, (70-X)%DMPC, and X% TR-DHPE. Each data point in (A) and (B) was the average of at least six different domains from single monolayes at surface pressure of 8mN/m. Different data points were obtained from independent monolayer setups. Error bars represents standard error of mean.

Chapter 7: Interactions between Silicone Oil and Immunoglobulin G at Air/Water Interfaces

Despite the prevailing application of PDMS in biomedical devices, there are few studies that explore the interaction between SO and biopolymers from a physical-chemical perspective. A few reports have studied the interaction between SO and proteins in deposited films consisting of the two components, but limited structural information could be extracted[59,61]. Another approach is to use Langmuir monolayers to investigate thin-film structures at the air-water (A/W) interface. Bernardini et al. used this approach coupled with Brewster Angle Microscopy (BAM) to study the mixed film of PDMS and polymethylmethacrylate (PMMA) and found that at low percentage of PMMA, it serves as a contrast enhancer which highlights the layering transition of PDMS at the A/W interface[143].

Previously, Liao et al. used PDMS elastomer to create a chamber with a flat air-water (A/W) interface for optical imaging of fluorescently labeled proteins[144]. Protein behavior was described that occurred in aqueous protein solution at neutral pH and on timescales of minutes to a few hours. More recently, we discovered that under acidic conditions (pH = 5.0) and reduced protein concentration (μg/mL), circular domains formed at the A/W interface in 1 h (Figure 7.1A). At neutral pH, the circular domains formed more slowly, on time scales ~12 h. Such phenomena, not observed in a water droplet but seen reproducibly in the PDMS chamber, led us to hypothesize that the

circular domains were initiated by oligomers leaching from PDMS elastomer into aqueous solution, with potential for protein interaction at the A/W interface. MALDI-TOF mass spectrometric analysis of toluene-extracted residues from the PDMS chamber confirmed the presence of oligomers (Figure 7.1B). Although PDMS degradation has been generally considered to be a slow process, it has been known to be affected by UV irradiation, pH, and temperature[145]. Acidic conditions could catalyze hydrolysis of high molecular weight linear PDMS[146], thus releasing oligomers into solution that subsequently adsorb at the A/W interface and compete with surface-active proteins. In this Chapter, we investigated the role of PDMS at the A/W interface under controlled conditions.

Thin film structures of PDMS and the protein immunoglobulin G (IgG) were formed at the A/W interface in order to elucidate the interaction between the two components. Using the Langmuir monolayer approach, we could control the amount of PDMS spread at the A/W interface and the amount of protein injected into the subphase. IgG was chosen as the model protein for the reason that it is the most abundant antibody isotype in human serum. To track the distribution of proteins in the interfacial film with optical microscopy, IgG was labeled with Texas Red (see Chapter 2 for details). Combining surface pressure measurements, in situ fluorescence imaging and topography studies of films transferred onto a glass surface by transmission electron microscopy

(TEM), the structures of PDMS and mixed PDMS/protein films were investigated and a mechanistic interaction model was proposed.

7.1 Surface Pressure-Surface Concentration Isotherm of Silicone Oil

Surface pressure (π)–surface concentration (C_{surf}) isotherm measurements were performed on SO and SO/IgG mixtures. The π- C_{surf} isotherm of PDMS wass shown in Figure 7.2. In line with previously published results[147–149], two marked increases in surface pressure were observed in our experiment. Two critical surface concentrations, determined from the local maximum of first derivative of π with respect to C_{surf}, were identified as C_1 and C_2. From the first derivative of the π-C_{surf} isotherm, two critical surface concentrations of PDMS were identified as C_1 and C_2, which are the local maxima. The π-C_{surf} isotherm of PDMS was then divided into four regions, and corresponding conformational models of PDMS chains have been proposed in the literature[149,150], summarized in Figure 7.3. In region I, C_{surf} was low and polymer chains were well spaced. In region II, as C_{surf} increased, the chains were compacted and came in contact. They then adopted more ordered conformations with the more hydrophilic oxygen atoms immersed in the subphase and hydrophobic silicone-methyl groups sticking into the air.

While most researchers agree on the chain conformation model of regions I and II, more controversy surrounds regions III and IV. Earlier studies using reflected infrared

spectroscopy proposed the helix model, which states that upon further compression from region III to IV, the helices slide on each other, which leads to the second increase in surface pressure[149,151]. The helical structures of PDMS chains in regions III and IV are similar to the structures found by X-ray diffraction and NMR of PDMS crystals[152,153]. On the other hand, Lee et al. found that the ellipticity of PDMS film at the A/W interface changed abruptly from region III to region IV, not exhibiting a continuous transition as suggested by the helix model. Instead, the step increase in ellipticity indicated the formation of a multilayer structure[154]. This alternative model of chain conformation was further strengthened by Kim et al., who found that the vibrational sum frequency intensity in region IV was not diminished as would be expected for standing helices. Thus, they identified the Si-O chain conformation in regions III and IV as a horizontal folding model on top of the monolayer[150]. Depending on whether the chain adopts helical structure or horizontal folding, C_2 resembles the transition of chain conformation from helices to standing helices or from single-folded layer to folded multilayer. Using C_1 and C_2 as the measurement of conformational transition, we then studied how the two values are changed with addition of protein.

7.2 Surface Pressure-Surface Concentration Isotherm for SO/IgG

Figure 7.4A showed the π-C_{surf} isotherms of SO with Texas Red-labeled immunoglobulin G (IgG-TR) added to the subphase. SO was first spread at the air-buffer interface at 0.4 mg/m^2, where surface pressure remained 0 mN/m. Protein was then

injected into the subphase and allowed to adsorb to the A/W interface. After a 1-h equilibration, the interfacial layer was compressed at 10 mm/min, while surface pressure measurements were performed (see Chapter 2 for details). Each trace shown was the average of three parallel experiments. Comparing π vs. [IgG-TR] in four different regions in Figure 7.4B, increasing concentration of IgG-TR in the subphase lead to pronounced increase of π in regions II and IV, and moderate increase in region I. In contrast, the surface pressure in region III remained constant over the range of IgG-TR concentrations studied. Furthermore, we extracted the C_{surf} of SO (C_1 and C_2), as well as the surface pressure at these transition points to evaluate the effect of IgG-TR on the phase transition of SO. Increasing subphase concentration of IgG-TR was observed to shift C_1 and C_2 to smaller values (Figure 7.4C), while transition surface pressure (π_{trans}) increased with increasing concentration of IgG-TR (Figure 7.4D). The trend in decreasing C_1 and C_2 values suggested that IgG-TR in the interfacial layer reduced available area for SO, and thus decreased the amount of SO at the interface that is necessary to make the conformational transitions.

7.3 Fluorescence Images of Domains in Region IV

In parallel with the isotherm study, we used fluorescence microscopy in the Langmuir trough to study phase changes at the A/W interface. Domains were only found in region IV during compression. Figure 7.5 showed the fluorescence intensity of the interfacial layer quantified as total interface fluorescence intensity (I_{inter}), which is average

intensity of each pixel times the total surface area of the film during the compression. Dash lines indicated the four regions defined by the surface pressure. The intensity curve remained flat in regions I-III, and then jumped significantly in region IV, a four-fold increase. We determined that the fluorescence intensity was not proportional to the concentration of IgG-TR in silicone oil, as the quantum yield reached a maximum at ~5 μg/mL IgG-TR. Thus, the amount of protein at the interface in region IV exceeded that in regions I-III by more than four-fold. The large error bars shown in Figure 7.5 reflected significant heterogeneity at the A/W interface in region IV.

Combining the compression isotherm with fluorescence imaging could provide information about PDMS-protein interactions at the A/W interface. The compression experiment measured how protein and SO in the mixed film interact with each other when the intermolecular distance was decreased by film compression, while fluorescence imaging indicated the distribution of proteins in the interfacial film. IgG-TR partitioned into the interfacial layer in region I, occupying available surface area between loosely packed silicone chains. The moderate increase of surface pressure in region I could be explained by minimal contact between PDMS chain and protein. In region II, proteins and SO came into close contact with each other, thus competing for the available surface area. Due to the fact that Si-O chains were highly flexible and able to reorient themselves to occupy the surface area, they pushed proteins into the sub-layer and formed a PDMS monolayer at the interface in region III. This was demonstrated by the result that surface

pressures of SO/IgG-TR mixtures were close to that of pure SO film in region III. The protein likely remained in the sub-layer that is close to the interface, as the total fluorescence intensity from IgG-TR remained steady throughout regions I-III. The increase of surface pressure and fluorescence intensity in region IV suggested that upon further compression, a change in silicone chain conformation promoted the localization and interaction of proteins at the interface, especially in the circular domains.

To test the hypothesis that the circular domains identified by fluorescence imaging in SO/IgG-TR mixtures in region IV are formed by SO and then labeled by preferential adsorption of protein, we carried out a titration experiment, where SO was first spread at the interface at C_{surf} = 3.2 mg/m^2, where π increased to 9.0 mN/m. Then IgG-TR was injected into the subphase, and later adsorbed to the SO film. We used free BODIPY, which favorably stains hydrophobic moieties[155,156], to trace the distribution of SO at the A/W interface. Indeed, in region IV, the circular domains were observed with BODIPY in the SO film (Figure 7.6A). Similar domain structure of PDMS (Mw = 10,000) film on water was reported by Mann et. al using Brewster Angle Microscopy[157]. The domains should correspond to specific locations with standing helices or multilayers. Indeed, we found that after injection of IgG-TR into the subphase, proteins preferentially localized to the circular domains at the interface (Figure 7.6B). In Figure 7.6C, the overlaid images of BODIPY and IgG-TR showed that IgG-TR tended to localize at the outer edge of SO circular domains. With further increase in the amount of IgG-TR

injected into the subphase, the domain features were lost and the interface became more homogenous and dominated by TR fluorescence (Figure 7.6D). This indicated that increased partitioning of protein in the interfacial layer could disrupt the PDMS film.

The cause of the preferential adsorption of IgG-TR to circular domains is not clear to us yet, but we hypothesize that it may be due to increased hydrophobicity of the domains. It has been known that hydrophobic surfaces favor protein adsorption by the change in free energy[158]. On films made of polymer blends, proteins have been observed to adsorb preferentially to the most hydrophobic regions[159]. For PDMS film in region IV, where the circular domains were highly compacted polymer chains, increased hydrophobicity in the domain should favor protein adsorption. We also used a more hydrophilic dye Sulforhodamine 101 in comparison to BODIPY to trace the distribution of SO at the A/W interface. The rationale of using the two different dyes is that if the SO film phase separates into patches of different hydrophobicity, this might be shown in the distribution of dyes in the film. To our surprise, both dyes were excluded from the domains in SO films in region IV, which could result from the high density of the polymer chains in the domain which prevents other molecules' binding.

7.4 Characterization of Micro-Structures of Domains

To further characterize the micro-structures of domains observed in region IV, SO and SO/IgG-TR domains were transferred on solid substrate and imaged by transmission

electron microscopy (TEM). Films were transferred to glass coverslips through Langmuir-Schaefer approach and air-dried. The transferred samples were first imaged by fluorescence microscopy. To facilitate TEM imaging, samples were coated with platinum and carbon from ~80° tilted angle, followed by separating coverslip from platinum replica (details in Chapter 2). From fluorescence microscopy, elliptical instead of circular domains were observed after transfer (Figure 7.7A), likely caused by distortion during the transfer step. Bright spots inside the domains of transferred SO film possibly resulted from the aggregation of dye molecules (Sulforhodamine 101) during the drying process. Fluorescence images of transferred SO/IgG-TR film also revealed branched features inside circular domains in SO/IgG-TR film indicating inhomogeneous adsorption of IgG-TR to the domains (Figure 7.7B), which was also suggested in Figure 7.6B recorded prior to transfer. The TEM images shown in Figures 7.7C and 7.7D for SO and SO/IgG-TR domains, respectively, implied that the single domains have three-dimensional structures. Moreover, different intensities implied height differences between domains and the peripheral area. Using a geometric estimation of TEM images captured under different tilted angles of the sample holder[160], the height of domains in SO film was estimated to be 200±150 nm, while that of SO/IgG-TR was estimated to be 300±170 nm. No previous reports have studied the domain height compared to the peripheral area. However, by ellipsometry and neutron reflectivity, Mann et al. have reported the overall film thickness of SO to be ~1.4 nm[147,157], which is significantly thinner than the domain height we have

estimated from TEM images. Ellipsometry and neutron reflectivity allowed in-situ measurements of film thickness, but the readout should be the average thickness over the domains and the peripheral area, and may not reflect the heterogeneity introduced by widely spaced, single domains. Future research will be required to explain further this discrepancy.

From the compression isotherm, fluorescence imaging and TEM imaging of transferred film, we propose the following mechanistic model of SO/IgG-TR interaction at the A/W interface as follows: In region I, proteins adsorb to the free surface area between randomly oriented silicone chains. As the silicone chains start to adopt more ordered structure in region II, proteins are less exposed to air, as they are squeezed out of the monolayer at the interface by ordering silicone chains. In region III, proteins stay in the sub-layer beneath the film formed by silicone chains. In region IV, as heterogeneity in the film of standing helix structure or multilayer domains is increased by further compression, proteins preferentially adsorb to circular SO domains that form.

7.5 Domain Fluctuation in Human Serum Albumin/Polydimethylsiloxane Systems

In addition to static information on line tension in model biomembrane systems described in Chapter 6, we were also interested in extending the analysis to protein and polymers film. Moreover, monitoring domain fluctuation as a function of time could provide further information on underlying environments, e.g. viscosity of domain and

underlying fluid.[75] To this end, we employed the model system containing Texas Red-labeled human serum albumin (HSA) blended with PDMS oligomers. This system was found to form circular fluctuating domains at air-water interface in Langmuir trough (see details in early this Chapter and Figure 7.1A).

We first investigated the line tension of domains by flicker spectroscopy[78] as mentioned in Chapter 6 (Figure 7.8). No upward deviation from 1/3 in amplitude ratio against n^2-1 was found, which suggested the electrostatic interaction in this system could be neglected (Figure 7.8D).

Several models have been proposed to explain the relaxation time of domain fluctuation. Stone and McConnell discussed the scenario at which membrane viscosity can be neglected[133], and only underlying fluid dominates domain dynamics. This gives expression for relaxation time as,

$$\tau_n^{\text{fluid}} = \frac{2\pi R^2 \eta_f}{\lambda} \frac{n^2 - 1/4}{n^2(n^2 - 1)} \tag{7.1}$$

where η_f represents the viscosity of the underlying fluid and λ stands for the line tension of domains. In the opposite scenario discussed by Mann et al.[161], membrane viscosity dominates the relaxation time,

$$\tau_n^{\text{membrane}} = \frac{4\eta_m R}{n\lambda} \tag{7.2}$$

where η_m represents the viscosity of membrane. Recently, Camley et al. developed a theoretical expression considering both membrane viscosity and underlying fluid viscosity,

$$\tau_n = \frac{\eta_m R}{\lambda} \frac{1}{n^2(n^2-1)} [\int_0^\infty dx \frac{J_n^2(x)}{x^2(x+\Lambda)}]^{-1} \quad (7.3)$$

where $J_n(x)$ is a Bessel function of the first kind and $\Lambda = 2R\eta_f/\eta_m$. Before examining the viscosity of HSA/PDMS film, we first developed a MATLAB algorithm applying theory by Camley et al. and validated our algorithm by reproducing the plot in Figure 2 of their published work[162]. The relaxation times in Figure 7.9 demonstrated the relaxation times by assuming line tension as 0.1 pN, domain radius as 2.5 μm and water viscosity as 0.01 poise.

By fitting time autocorrelation function of amplitude with exponential decay (Figure 7.10A), the decay time as a function of mode number was obtained. Plots in Figure 7.10B suggested that membrane viscosity significantly affects relaxation time. By line tension obtained from static analysis (Figure 7.8), film viscosity of 8.3×10^{-5} s.p. was determined.

7.6 Summary

In summary, we have systematically investigated the interactions in SO/IgG-TR films from a physical-chemical perspective. This study could shed light on the complex

interplay between IgG-TR and SO, and should apply to other proteins and SO interactions in general. Our study indicated that by keeping the surface concentration of SO under the limit required to form domain structures in region IV (~1.6 mg/m^2), one could significantly reduce the amount of protein going to the interface, thus reduce the protein loss and denaturation at the interface. Moreover, the viscosity of HSA/PDMS film was determined through flicker spectroscopy approach. This work also provided a cautionary tale about the use of PDMS in biotechnology applications, particularly involving proteins. Clearly, leaching of PDMS oligomers can have a profound effect on protein surface behavior under some conditions.

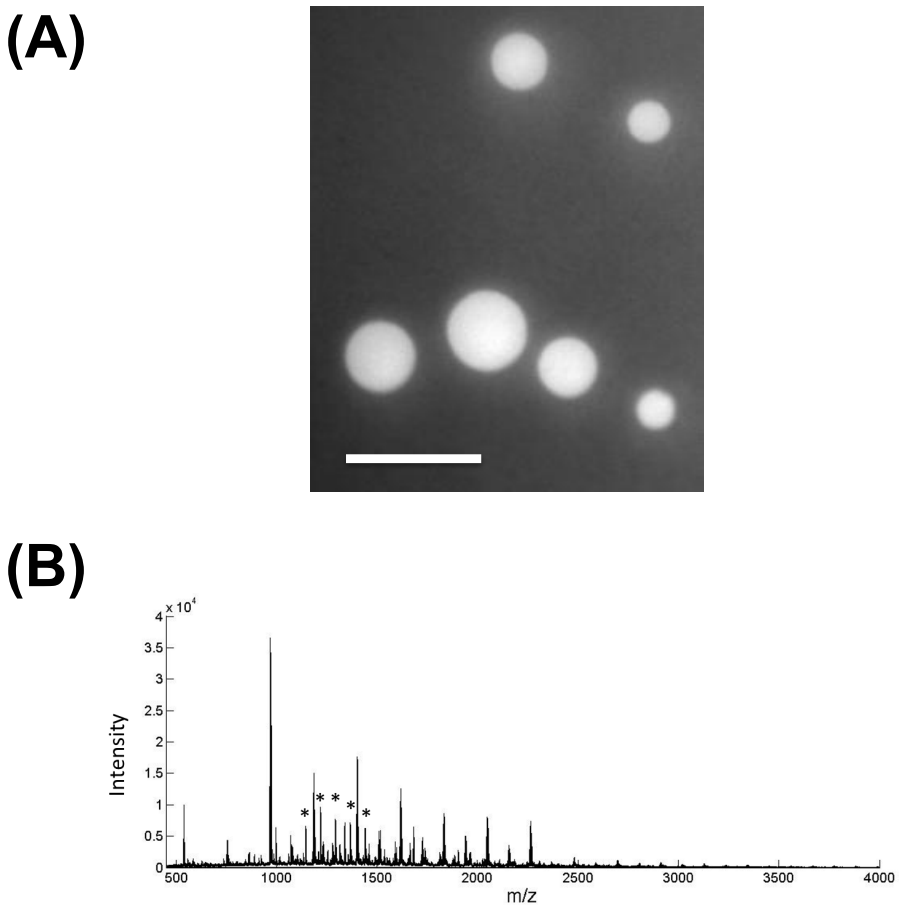

Figure 7. 1 Domains observed at A/W interface for PDMS chamber.

(A) Domains formed around 1 hr after addition of Texas Red labeled human serum albumin (2 μg/ml) in PDMS chamber. Buffer: 10 mM acetic acid/ sodium acetate buffer pH 5.0. (B) MALTI-TOF spectrum of extracted residues from PDMS elastomer extracted by toluene. Asterisks mark the peaks of PDMS where Δm/z between neighboring peaks is 74.

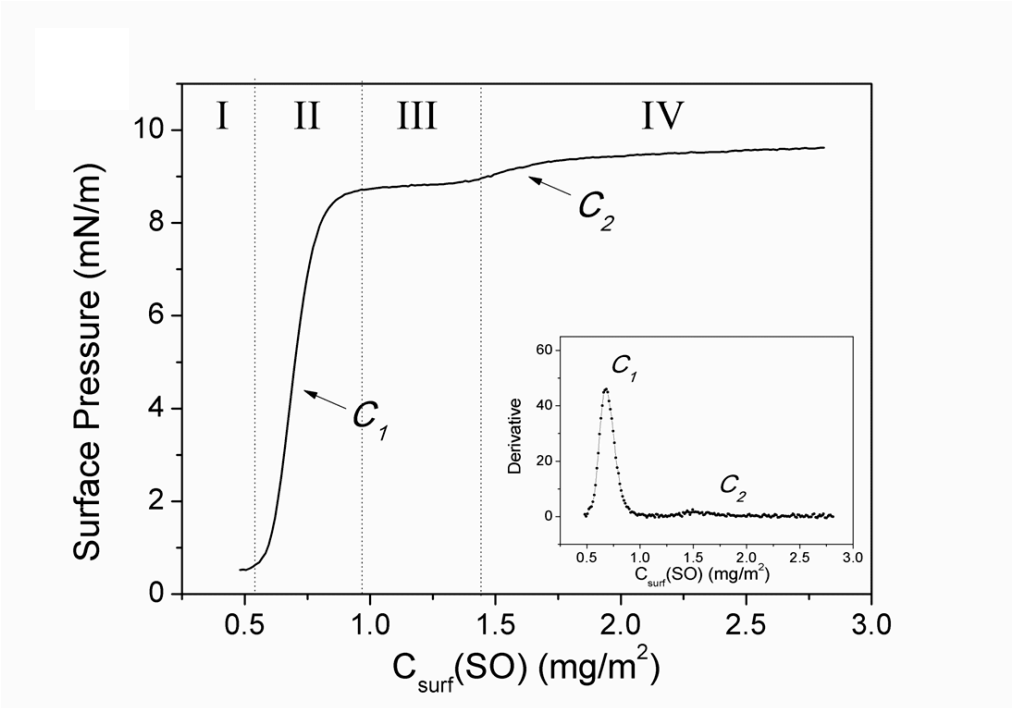

Figure 7. 2 Surface pressure-surface concentration isotherm of silicone oil.

The isotherm showed is the average of four repeats. Dashed line divides the curve into four regions, I-IV, corresponding to different proposed conformations. Insert shows the first derivative of the isotherm, where C_1 and C_2 correspond to the local maxima in regions II and IV.

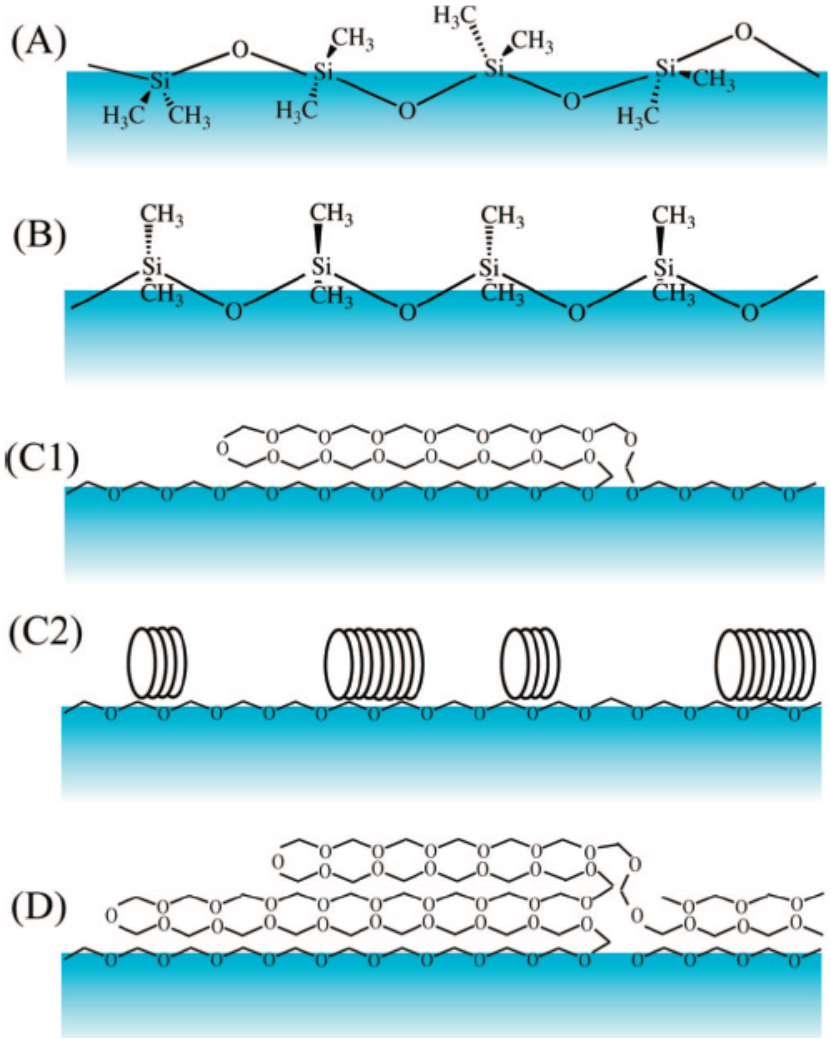

Figure 7. 3 Proposed models of conformation of silicone chains at the A/W in four regions.

Image source: Kim et al., 2008, Langmuir, 24, 10155-10160.

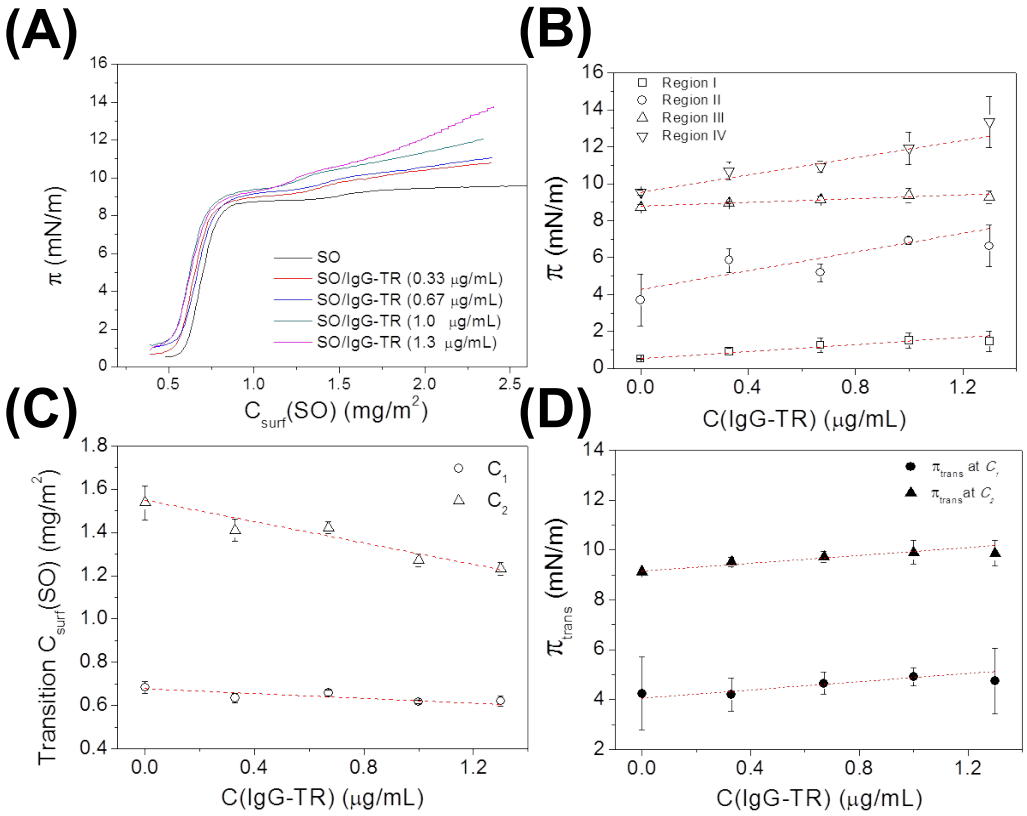

Figure 7. 4 The effect of IgG-TR on silicone oil film.

(A) Surface pressure of SO (spread at the AWI) / IgG-TR (injected into subphase) systems. Each trace of SO/IgG-TR is the average of three repeats. (B) Surface pressure at fixed surface concentration of SO in regions I-IV changed by subphase concentration of IgG-TR. Region I: 0.50 mg/m^2, region II: 0.67 mg/m^2, region III: 1.0 mg/m^2, region IV: 2.3 mg/m^2. (C) Transition surface concentration of SO changed by subphase concentration of IgG-TR. (D) Transition surface pressure at C_1 and C_2. Dashed lines are the linear fit.

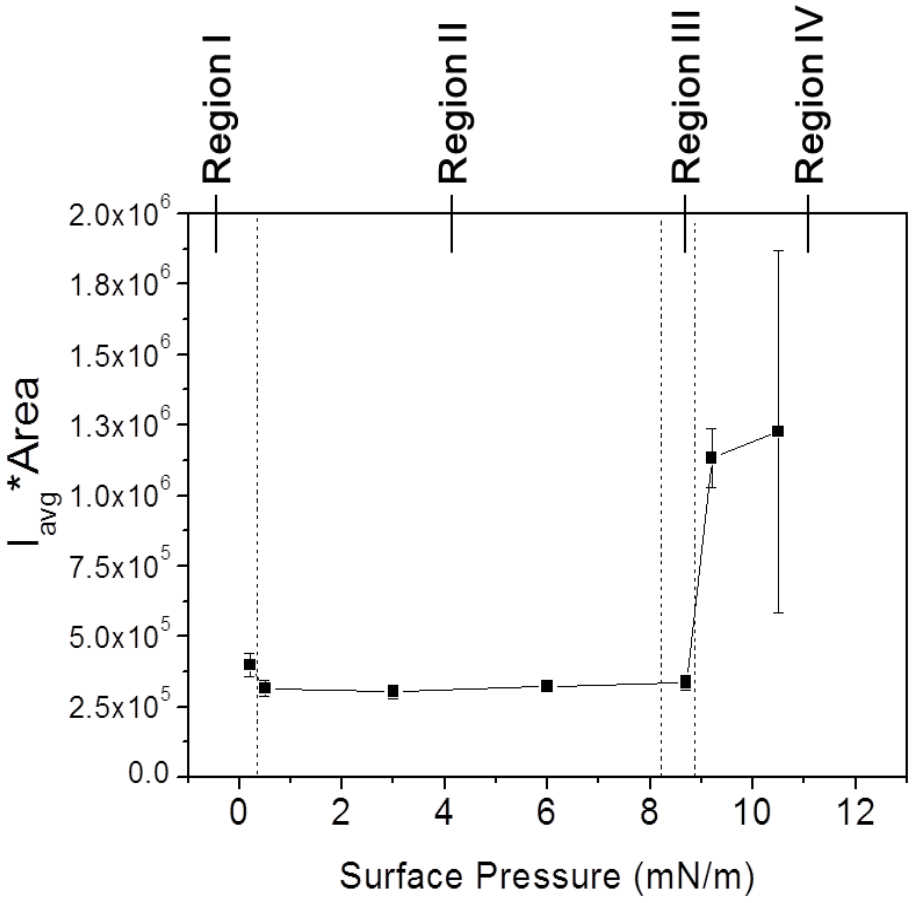

Figure 7. 5 Change in fluorescence intensity of IgG-TR at different regions.

Change of fluorescence intensity of IgG-TR at the interface with compression of SO/IgG-TR (3.3 $\times 10^{-4}$ mg/mL) mixed film.

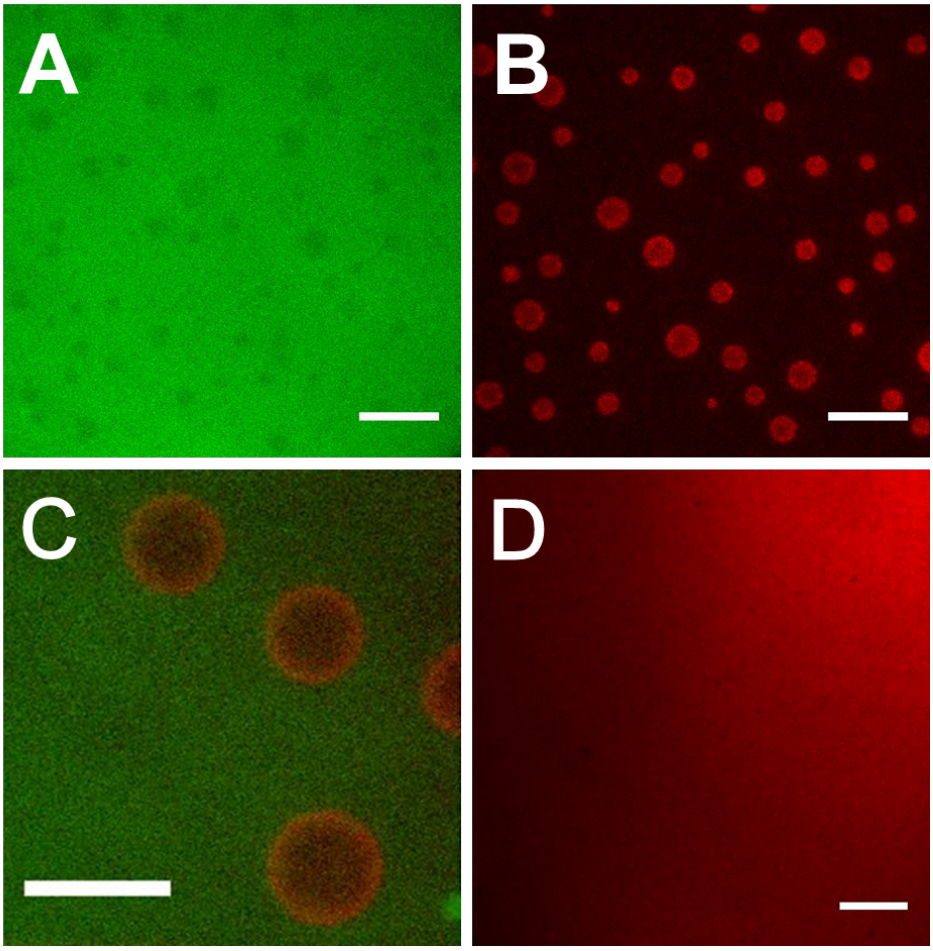

Figure 7. 6 Fluorescence image of domains at region IV.

Fluorescence images of SO only and SO/IgG-TR layer at the A/W interface. (A) SO-only in region IV: C_{surf}(SO) = 3.2 mg/m^2, π_{trans} = 8.9 mN/m. (B) SO and IgG-TR injected into subphase: C_{surf}(SO) = 3.2 mg/m^2, [IgG-TR] = 0.33 μg/mL, π_{trans} = 9.0 mN/m. (C) Zoomed-in micrograph of domains with BODIPY and TR images overlaid. (D) SO and IgG-TR injected into subphase: C_{surf}(SO) = 3.2 mg/m^2, [IgG-TR] = 1.3 μg/mL, π_{trans} = 10.1 mN/m. Scale bar: 20 μm.

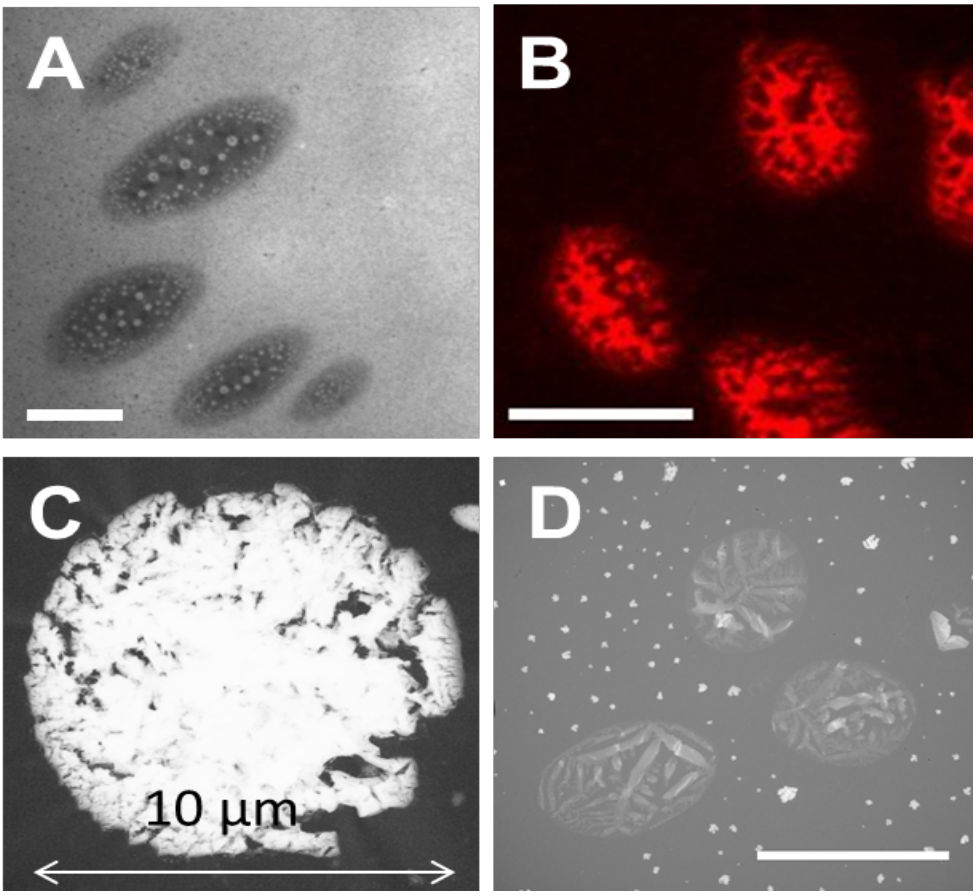

Figure 7. 7 Topographic analysis from transferred SO and SO/IgG films at region IV.

Fluorescence image of (A) transferred SO film with Rhodamine 101 staining, (B) transferred SO/IgG-TR film. TEM image of (C) platinum replica of transferred SO sample, (D) platinum replica of transferred SO/IgG-TR sample. Scale bar in (A), (B) and (D): 20 µm.

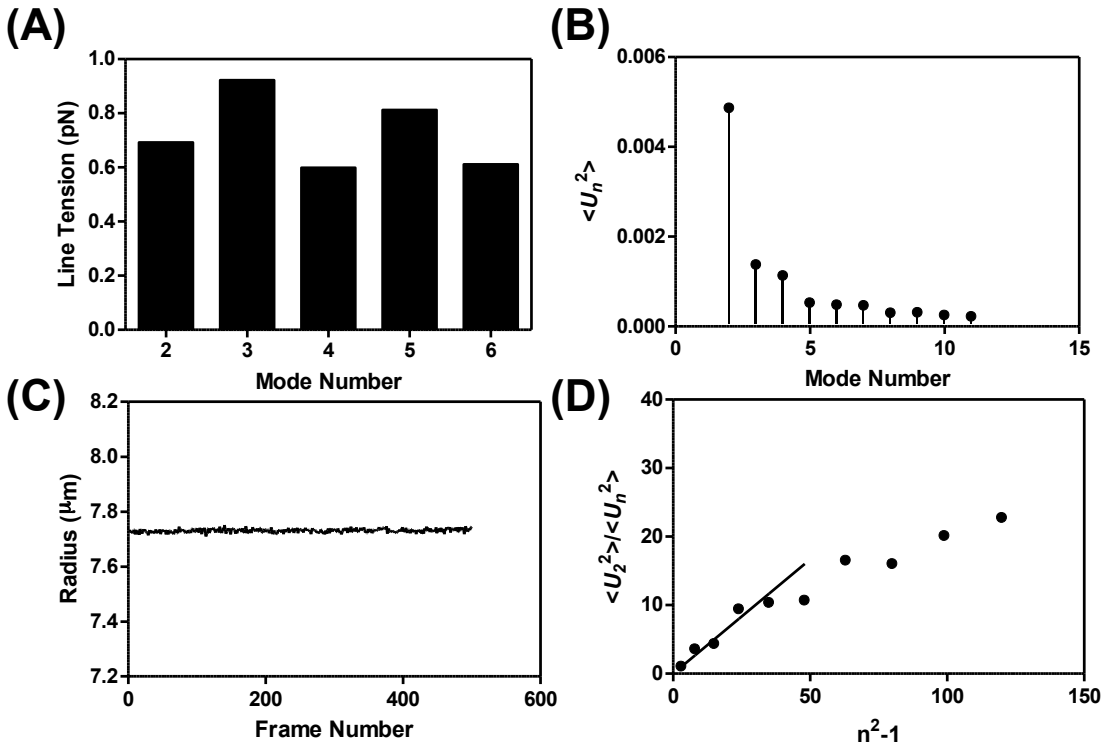

Figure 7. 8 Line tension and domain fluctuation amplitude for HSA/PDMS domain.

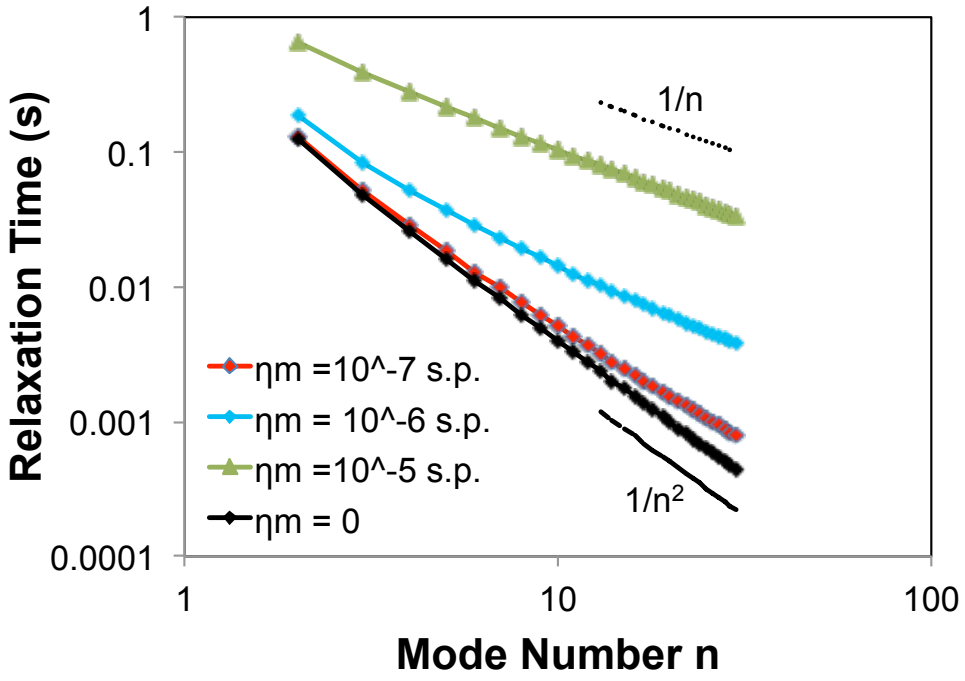

Figure 7. 9 Calculated relaxation time as a function of mode number with assumed line tension and domain radius.

Reproduced work of Camley et al.[162] demonstrated that relaxation times decrease with mode number. This plot displayed that, with higher membrane viscosity, the relation between relaxation time closer to 1/n, the model developed by Mann et al.[106], while close to $1/n^2$, model proposed by Stone et al.[133], when membrane viscosity is neglected.

(A)

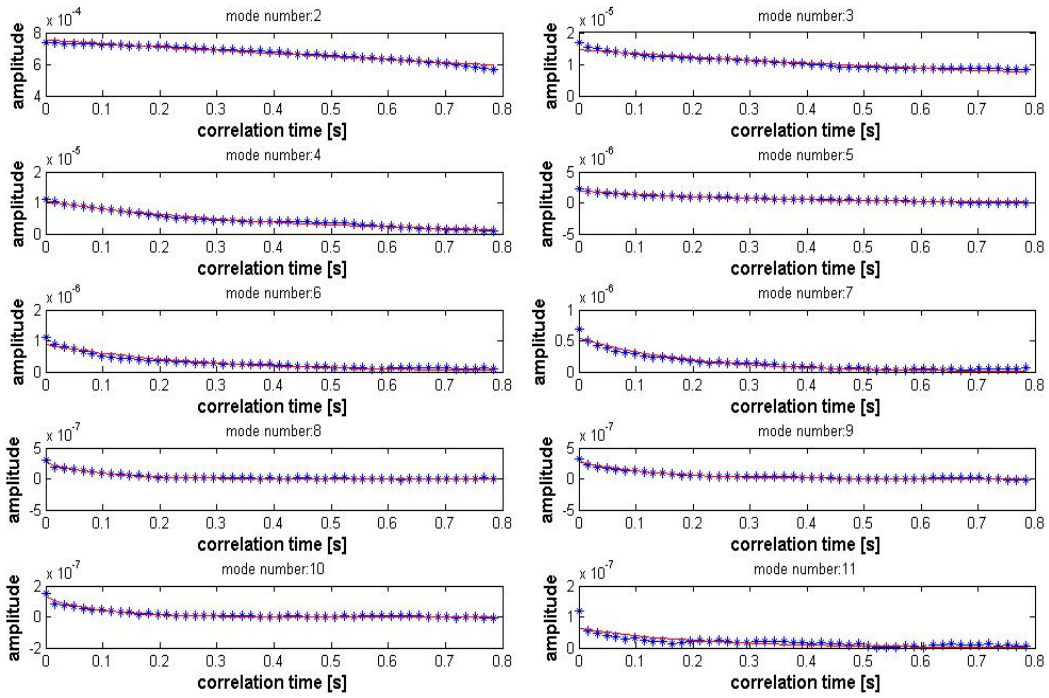

(B)

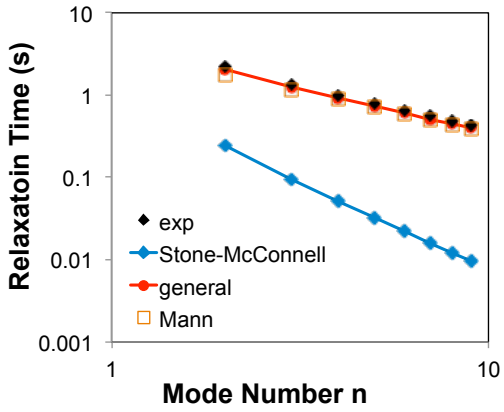

Figure 7. 10 Relaxation time as a function of mode number n.

Chapter 8: Future Work and Outlook

8.1 Two-Dimensional Macroscopic Protein Domains Induced by the Interplay between Lipid-Lipid and Protein-Protein Interactions

It has been suggested that lipids and proteins are not homogeneously distributed in cell membranes; they can segregate into dynamic micro/nanodomains, serving as centers for signal transduction, membrane trafficking, and cytoskeletal organization[163]. In Chapter 4, we supported this notion by representing that the phase behaviors could be determined by different structures of ceramide domain in ganglioside GM1. In Chapter 6, we further discussed the line tension of lipid domains in lipid monolayer and GUVs and examined the potential molecules which could modulate line tension. The prevailing studies for membrane inhomogeneity as a regulation center are based on coexistence of lipids phases in model membranes, e.g. lipid monolayer and GUVs, or biomembranes, e.g. giant plasma membrane vesicles[49] (GMPVs) and plasma membrane spheres[164] (PMS), where fluorescent lipid can be used as a marker for specific liquid phases. However, it remains unanswered whether two-dimensional protein domains themselves can be created by the interactions between membrane-anchored proteins.

Signaling proteins are often found to be linked in tandem in a single polypeptide[165], e.g. multiple SH3 (src homology 3) domains in adaptor protein Gads bind to its binding partner, PRM (proline-rich motif) of SLP76 upon T-cell activation[166];

adaptor protein Grb2 containing two SH3 domains can associate with PRM of SOS, involved in cell growth and differentiation[166].

Utilizing the binding pairs, SH3 and PRM, which were recently reported to form phase-separated micro-droplets in solution[167], with histidine tags allowing efficient binding to lipid membranes containing nitrilotriacetic acid (NTA) lipids, we demonstrated that macroscopic protein domains appeared in giant unilamellar vesicles (GUVs).

Two-dimensional macroscopic protein domains induced in GUVs

To evaluate the domains induced by multivalent proteins, we first ensured that the lipid composition under investigation gives homogeneous membrane. The result in Figure 8.1 demonstrated that Texas-Red DHPE distributed homogeneously on GUVs consisting of 5% NTA-DOGS (18:1 1,2-dioleoyl-sn-glycero-3-[(N-(5-amino-1-carboxypentyl) iminodiacetic acid)succinyl (Ni)] and 95% DOPC (Figure 8.1A and B). We then tested the specificity of membrane binding of SH3(5)_histag and PRM(5). SH3(5) and PRM(5) did not show membrane binding in GUV without NTA-DGS present (Figure 8.1D and E). When 5% of NTA-DGS was present, SH3(5)_histag appeared to bind to GUVs homogeneously, whereas PRM(5) did not show binding due to the absence of histidine tag (Figure 8.2).

When PRM(5) and SH3(5)_histag were both present, PRM(5) was recruited to membrane, possibly through the interactions between PRM and SH3 domains. Interestingly, the micrometer-sized circular domains appeared under certain conditions (Figure 8.3). The overlapping fluorescence images from PRM(5) and SH3(5)_histag channels suggested that these domains were enriched in both SH3(5) and PRM(5).

This phase behavior was observed to depend on protein concentrations in bulk (Figure 8.3). The phase diagram in Figure 8.3 demonstrated that increasing concentration of proteins is prone to form domains. Higher than 85% of GUVs displayed inhomogeneity in protein concentration around 200 nM. Moreover, the critical concentration for domain formation seems to depend on the valency of proteins. In the protein pairs of PRM(3) and SH3(5)_histag, less than 50% of vesicles displayed inhomogeneity in protein concentrations of 500 nM.

We next investigated the kinetics of domain formation at the protein concentration of 200 nM. Once the vesicles were settled down in the imaging chamber, protein mixture was injected and protein binding was monitored with respect to time. The domain was found to form at around 10 min.

In future work, we will quantitatively assess domain formation kinetics. Additionally, it will be interesting to investigate whether theses two-dimensional macroscopic protein domains can also form in physiological temperature. Overall, we

have demonstrated that the interplay between lipid-protein and protein-protein interactions can induce macroscopic protein domains on model membranes.

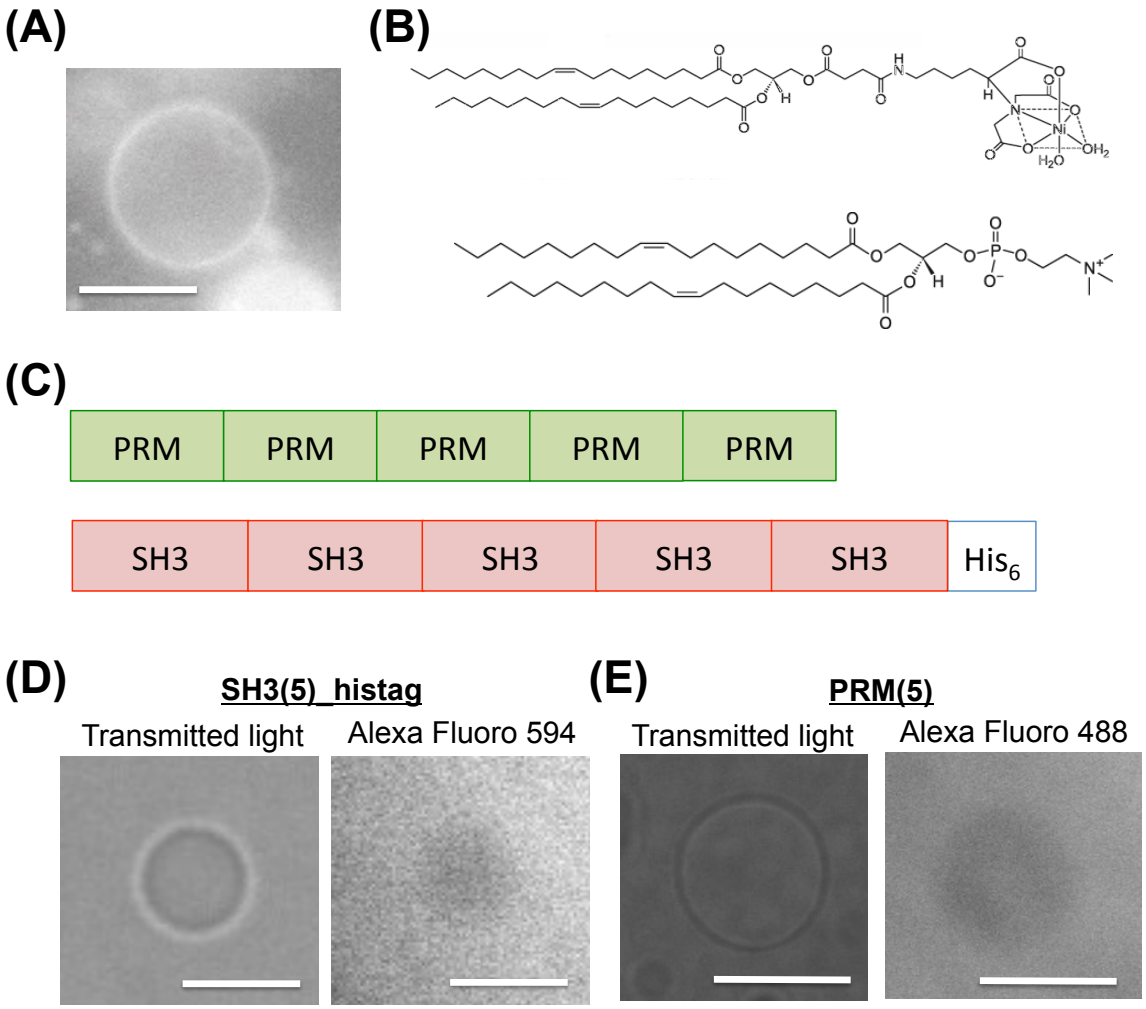

Figure 8. 1 Experimental design and control experiments.

(A) Texas Red-DHPE distributed homogeneously on GUVs containing 5% NTA-DGS and 95% DOPC. (B) Structures of 18:1 NTA-DGS (top) and DOPC (bottom). Ni^{2+} loaded NTA moiety allowed for chelating with histidine. (C) Cartoon demonstrates the multivalent proteins in this study. (E and F) PRM(5) and SH3(5) alone did not bind to DOPC only GUVs, suggesting no non-specific binding between proteins and DOPC.

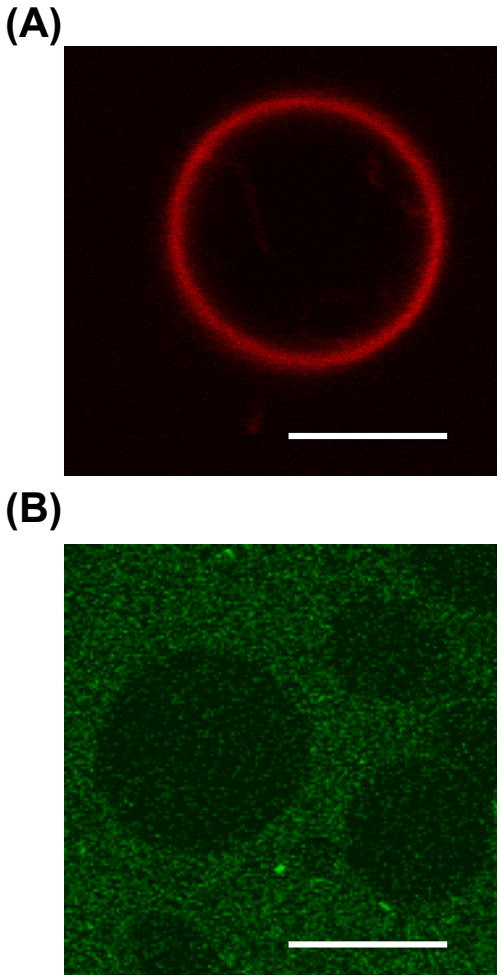

Figure 8. 2 Confocal images of GUVs incubated with only SH3(5)_histag or PRM(5).

(A) Alexa Fluoro 594-labeled SH3(5)_histag showed homogeneous binding to GUVs containing 5% NTA-DGS. (B) In contrast, Alexa Fluoro 488-labeled PRM(5) did not bind to GUVs with the same composition. Scale bar: 10 μm.

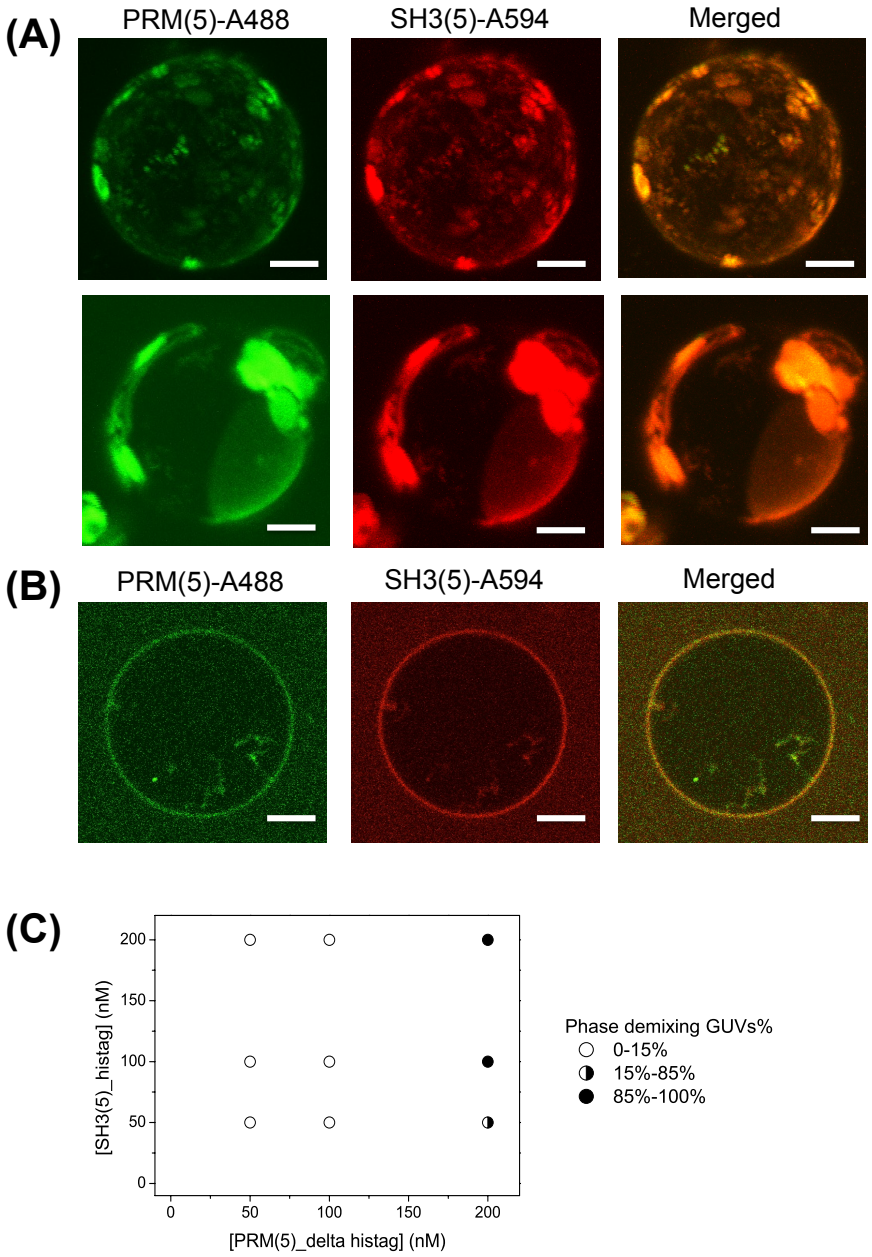

Figure 8. 3 Phase behavior is protein concentration-dependent.

(A) 3D stacking image of GUV demonstrated protein domain formation at [PRM(5)] = 200nM and [SH3(5)_histag] = 200 nM. (B) Confocal equatorial image showed homogeneous binding of

proteins at [PRM(5)] = 100nM and [SH3(5)_histag] = 200nM. (C) Phase diagram demonstrated the phase behavior depends on protein concentrations. Scale bar: 5 μm.

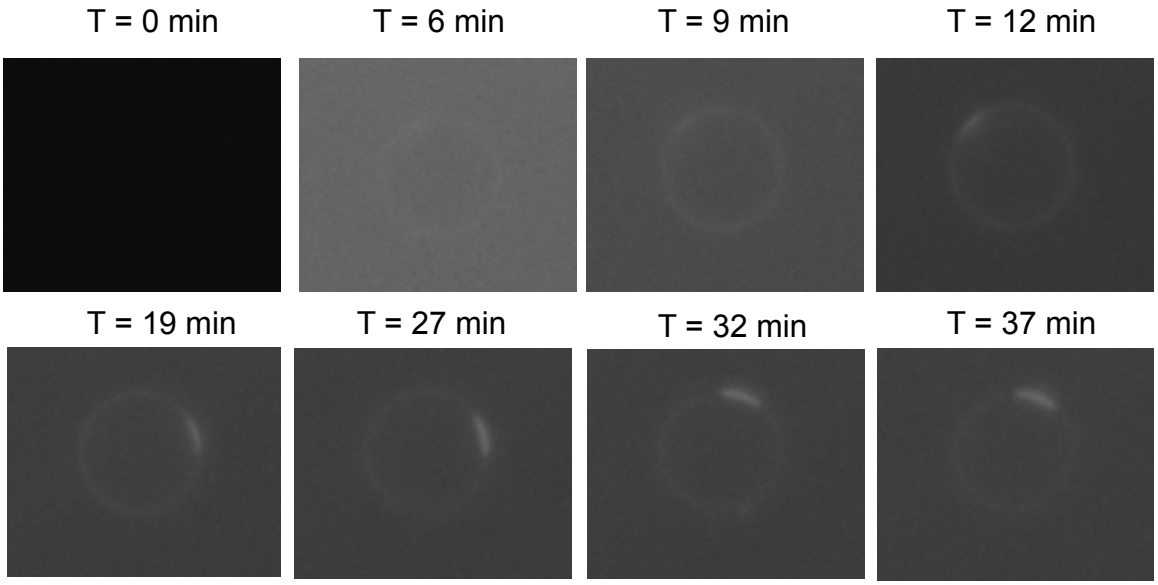

Figure 8. 4 Time course of formation of protein domain.

Time course of protein binding and the following domain formation of SH3(5) and PRM(5).

REFERENCES

(1) McMahon, H. T.; Gallop, J. L. *Nature* **2005**, *438*, 590–596.

(2) Baumgart, T.; Capraro, B. R.; Zhu, C.; Das, S. L. In *Annual Review of Physical Chemistry, Vol 62*; 2011; Vol. 62, pp. 483–506.

(3) Antonny, B. In *Annual Review of Biochemistry, Vol 80*; 2011; Vol. 80, pp. 101–123.

(4) Masuda, M.; Takeda, S.; Sone, M.; Ohki, T.; Mori, H.; Kamioka, Y.; Mochizuki, N. *Embo Journal* **2006**, *25*, 2889–2897.

(5) Sorre, B.; Callan-Jones, A.; Manzi, J.; Goud, B.; Prost, J.; Bassereau, P.; Roux, A. *Proceedings of the National Academy of Sciences of the United States of America* **2012**, *109*, 173–178.

(6) Gallop, J. L.; Jao, C. C.; Kent, H. M.; Butler, P. J. G.; Evans, P. R.; Langen, R.; T McMahon, H. *EMBO JOURNAL* **2006**, *25*, 2898–2910.

(7) Heinrich, M. C.; Capraro, B. R.; Tian, A. W.; Isas, J. M.; Langen, R.; Baumgart, T. *Journal of Physical Chemistry Letters* **2011**, *1*, 3401–3406.

(8) Verstreken, P.; Kjaerulff, O.; Lloyd, T. E.; Atkinson, R.; Zhou, Y.; Meinertzhagen, I. A.; Bellen, H. J. *Cell* **2002**, *109*, 101–112.

(9) Fugier, C.; Klein, A. F.; Hammer, C.; Vassilopoulos, S.; Ivarsson, Y.; Toussaint, A.; Tosch, V.; Vignaud, A.; Ferry, A.; Messaddeq, N.; Kokunai, Y.; Tsuburaya, R.; De la Grange, P.; Dembele, D.; Francois, V.; Precigout, G.; Boulade-Ladame, C.; Hummel, M. C.; De Munain, A. L.; Sergeant, N.; Laquerriere, A.; Thibault, C.; Deryckere, F.; Auboeuf, D.; Garcia, L.; Zimmermann, P.; Udd, B.; Schoser, B.; Takahashi, M. P.; Nishino, I.; Bassez, G.; Laporte, J.; Furling, D.; Charlet-Berguerand, N. *Nature Medicine* **2011**, *17*, 720–U112.

(10) Nicot, A. S.; Toussaint, A.; Tosch, V.; Kretz, C.; Wallgren-Pettersson, C.; Iwarsson, E.; Kingston, H.; Garnier, J. M.; Biancalana, V.; Oldfors, A.; Mandel, J. L.; Laporte, J. *Nature Genetics* **2007**, *39*, 1134–1139.

(11) Rikhy, R.; Kumar, V.; Mittal, R.; Krishnan, K. S. *Journal of Neuroscience* **2002**, *22*, 7478–7484.

(12) McMahon, H. T.; Boucrot, E. *Nature Reviews Molecular Cell Biology* **2011**, *12*, 517–533.

(13) Capraro, B. R.; Yoon, Y.; Cho, W.; Baumgart, T. *Journal of the American Chemical Society* **2010**, *132*, 1200–1.

(14) Bhatia, V. K.; Madsen, K. L.; Bolinger, P.-Y.; Kunding, A.; Hedegård, P.; Gether, U.; Stamou, D. *The EMBO journal* **2009**, *28*, 3303–14.

(15) Heinrich, M. C.; Capraro, B. R.; Tian, A.; Isas, J. M.; Langen, R.; Baumgart, T. *The Journal of Physical Chemistry Letters* **2010**, *1*, 3401–3406.

(16) Gallop, J. L.; Jao, C. C.; Kent, H. M.; Butler, P. J. G.; Evans, P. R.; Langen, R.; McMahon, H. T. *The EMBO journal* **2006**, *25*, 2898–910.

(17) Peter, B. J.; Kent, H. M.; Mills, I. G.; Vallis, Y.; Butler, P. J. G.; Evans, P. R.; McMahon, H. T. *Science (New York, N.Y.)* **2004**, *303*, 495–9.

(18) Ford, M. G. J.; Mills, I. G.; Peter, B. J.; Vallis, Y.; Praefcke, G. J. K.; Evans, P. R.; McMahon, H. T. *Nature* **2002**, *419*, 361–366.

(19) Ramamurthi, K. S.; Losick, R. *Proceedings of the National Academy of Sciences of the United States of America* **2009**, *106*, 13541–13545.

(20) Shapiro, L.; McAdams, H. H.; Losick, R. *Science* **2009**, *326*, 1225–1228.

(21) Romer, W.; Berland, L.; Chambon, V.; Gaus, K.; Windschiegl, B.; Tenza, D.; Aly, M. R. E.; Fraisier, V.; Florent, J.-C.; Perrais, D.; Lamaze, C.; Raposo, G.; Steinem, C.; Sens, P.; Bassereau, P.; Johannes, L. *Nature* **2007**, *450*, 670–675.

(22) Ewers, H.; Romer, W.; Smith, A. E.; Bacia, K.; Dmitrieff, S.; Chai, W. G.; Mancini, R.; Kartenbeck, J.; Chambon, V.; Berland, L.; Oppenheim, A.; Schwarzmann, G.; Feizi, T.; Schwille, P.; Sens, P.; Helenius, A.; Johannes, L. *Nature Cell Biology* **2010**, *12*, 11–U36.

(23) Tian, A.; Baumgart, T. *Biophysical Journal* **2009**, *96*, 2676–2688.

(24) Safouane, M.; Berland, L.; Callan-Jones, A.; Sorre, B.; Romer, W.; Johannes, L.; Toombes, G. E. S.; Bassereau, P. *Traffic* **2010**, *11*, 1519–1529.

(25) Boucrot, E.; Pick, A.; Camdere, G.; Liska, N.; Evergren, E.; McMahon, H.; Kozlov, M. *Cell* **2012**, *149*, 124–136.

(26) Sorre, B.; Callan-Jones, A.; Manneville, J.-B.; Nassoy, P.; Joanny, J.-F.; Prost, J.; Goud, B.; Bassereau, P. *Proceedings of the National Academy of Sciences of the United States of America* **2009**, *106*, 5622–6.

(27) Tian, A.; Baumgart, T. *Biophysical Journal* **2009**, *96*, 2676–2688.

(28) Subramaniam, A. B.; Lecuyer, S.; Ramamurthi, K. S.; Losick, R.; Stone, H. A. *Advanced Materials* **2010**, *22*, 2142–2147.

(29) Sanii, B.; Smith, A. M.; Butti, R.; Brozell, A. M.; Parikh, A. N. *Nano Letters* **2008**, *8*, 866–871.

(30) Parthasarathy, R.; Yu, C. H.; Groves, J. T. *Langmuir* **2006**, *22*, 5095–5099.

(31) Chinnapen, D. J. F.; Chinnapen, H.; Saslowsky, D.; Lencer, W. I. *Fems Microbiology Letters* **2007**, *266*, 129–137.

(32) Fujinaga, Y.; Wolf, A. *Molecular biology of …* **2003**, *14*, 4783–4793.

(33) Wolf, a a; Jobling, M. G.; Wimer-Mackin, S.; Ferguson-Maltzman, M.; Madara, J. L.; Holmes, R. K.; Lencer, W. I. *The Journal of cell biology* **1998**, *141*, 917–27.

(34) Chinnapen, D. J.-F.; Hsieh, W.-T.; Te Welscher, Y. M.; Saslowsky, D. E.; Kaoutzani, L.; Brandsma, E.; D'Auria, L.; Park, H.; Wagner, J. S.; Drake, K. R.; Kang, M.; Benjamin, T.; Ullman, M. D.; Costello, C. E.; Kenworthy, A. K.; Baumgart, T.; Massol, R. H.; Lencer, W. I. *Developmental cell* **2012**, *23*, 573–86.

(35) Mukherjee, S.; Soe, T. T.; Maxfield, F. R. *The Journal of cell biology* **1999**, *144*, 1271–84.

(36) Taylor, M. J.; Lampe, M.; Merrifield, C. J. *PLoS biology* **2012**, *10*, e1001302.

(37) Taylor, M. J.; Perrais, D.; Merrifield, C. J. *PLoS biology* **2011**, *9*, e1000604.

(38) Capraro, B. R.; Shi, Z.; Wu, T.; Chen, Z.; Dunn, J. M.; Rhoades, E.; Baumgart, T. *The Journal of biological chemistry* **2013**.

(39) Cui, H. S.; Lyman, E.; Voth, G. A. *Biophysical Journal* **2011**, *100*, 1271–1279.

(40) Zhu, C.; Das, S. L.; T., B. *Biophysical Journal* **2012**, *102*, 1837–1845.

(41) Yoon, Y.; Zhang, X.; Cho, W. *Journal of Biological Chemistry* **2012**, *287*, 34078–34090.

(42) Semrau, S.; Schmidt, T. *Soft Matter* **2009**, *5*, 3174–3186.

(43) Pike, L. J. *Biochemical Journal* **2004**, *378*, 281–292.

(44) Simons, K.; Ikonen, E. *Nature* **1997**, *387*, 569–572.

(45) Samsonov, A. V; Mihalyov, I.; Cohen, F. S. *Biophysical Journal* **2001**, *81*, 1486–1500.

(46) Dietrich, C.; Volovyk, Z. N.; Levi, M.; Thompson, N. L.; Jacobson, K. **2001**.

(47) Subramaniam, S.; McConnell, H. M. *Journal of Physical Chemistry* **1987**, *91*, 1715–1718.

(48) Kaiser, H.-J.; Lingwood, D.; Levental, I.; Sampaio, J. L.; Kalvodova, L.; Rajendran, L.; Simons, K. *Proceedings of the National Academy of Sciences of the United States of America* **2009**, *106*, 16645–50.

(49) Baumgart, T.; Hammond, A. T.; Sengupta, P.; Hess, S. T.; Holowka, D. A.; Baird, B. A.; Webb, W. W. *Proceedings of the National Academy of Sciences of the United States of America* **2007**, *104*, 3165–3170.

(50) Lipowsky, R. *Journal De Physique Ii* **1992**, *2*, 1825–1840.

(51) Garcia-Saez, A. J.; Chiantia, S.; Schwille, P. *Journal of Biological Chemistry* **2007**, *282*, 8.

(52) Vind-Kezunovic, D.; Nielsen, C. H.; Wojewodzka, U.; Gniadecki, R. *Biochimica Et Biophysica Acta-Biomembranes* **2008**, *1778*, 2480–2486.

(53) Esposito, C.; Tian, A.; Melamed, S.; Johnson, C.; Tee, S.-Y.; Baumgart, T. *Biophysical journal* **2007**, *93*, 3169–81.

(54) Heinrich, M. C.; Levental, I.; Gelman, H.; Janmey, P. A.; Baumgart, T. *The journal of physical chemistry. B* **2008**, *112*, 8063–8.

(55) Goldstein, R. E.; Jackson, D. P. *Journal of Physical Chemistry* **1994**, *98*, 9626–9636.

(56) Lee, K. Y. C.; McConnell, H. M. *Journal of Physical Chemistry* **1993**, *97*, 9532–9539.

(57) McDonald, J. C.; Duffy, D. C.; Anderson, J. R.; Chiu, D. T.; Wu, H. K.; Schueller, O. J. A.; Whitesides, G. M. *Electrophoresis* **2000**, *21*, 27–40.

(58) Skorpik, C.; Menapace, R.; Gnad, H. D.; Paroussis, P. *Retina-the Journal of Retinal and Vitreous Diseases* **1989**, *9*, 8–14.

(59) Paguirigan, A. L.; Beebe, D. J. *Integrative biology : quantitative biosciences from nano to macro* **2009**, *1*, 182–195.

(60) Yang, C. S.; Chen, K. H.; Hsu, W. M.; Li, Y. S. *Eye* **2008**, *22*, 282–288.

(61) Jones, L. S.; Kaufmann, A.; Middaugh, C. R. *Journal of Pharmaceutical Sciences* **2005**, *94*, 918–927.

(62) Bee, J. S.; Randolph, T. W.; Carpenter, J. F.; Bishop, S. M.; Dimitrova, M. N. *Journal of Pharmaceutical Sciences* **2011**, *100*, 4158–4170.

(63) Thirumangalathu, R.; Krishnan, S.; Ricci, M. S.; Brems, D. N.; Randolph, T. W.; Carpenter, J. F. *Journal of Pharmaceutical Sciences* **2009**, *98*, 3167–3181.

(64) Suh, K. Y.; Kim, Y. S.; Lee, H. H. *Advanced Materials* **2001**, *13*, 1386–1389.

(65) Zhang, Y.; Lin, C.-T.; Yang, S. *Small* **2010**, *6*, 768–775.

(66) Saragih, A. S.; Ko, T. J. *International Journal of Advanced Manufacturing Technology* **2009**, *42*, 474–481.

(67) Sanii, B.; Smith, A. M.; Butti, R.; Brozell, A. M.; Parikh, A. N. *Nano Letters* **2008**, *8*, 866–871.

(68) Cremer, P. S.; Boxer, S. G. *Journal of Physical Chemistry B* **1999**, *103*, 2554–2559.

(69) Mornet, S.; Lambert, O.; Duguet, E.; Brisson, A. *Nano Letters* **2005**, *5*, 281–285.

(70) Soumpasis, D. M. *Biophysical Journal* **1983**, *41*, 95–97.

(71) Capraro, B. R.; Yoon, Y.; Cho, W.; Baumgart, T. *Journal of the American Chemical Society* **2010**, *132*, 1200–1.

(72) Mayer, B. J. *Journal of Cell Science* **2001**, *114*, 1253–1263.

(73) Yuan, Z. M.; Huang, Y. Y.; Ishiko, T.; Kharbanda, S.; Weichselbaum, R.; Kufe, D. *Proceedings of the National Academy of Sciences of the United States of America* **1997**, *94*, 1437–1440.

(74) Patty, P. J.; Frisken, B. J. *BIOPHYSICAL JOURNAL* **2003**, *85*, 996–1004.

(75) Thompson, N. L.; Burghardt, T. P.; Axelrod, D. *Biophysical journal* **1981**, *33*, 435–54.

(76) Pearce, K.; Hof, M.; Lentz, B.; Thompson, N. *Journal of Biological Chemistry* **1993**, *268*, 22984–91.

(77) Kates, M. *Techniques of lipidology : isolation, analysis, and identification of lipids*; North Holland Publishing Co.: Amsterdam [etc.], 1972.

(78) Esposito, C.; Tian, A.; Melamed, S.; Johnson, C.; Tee, S.-Y.; Baumgart, T. *Biophysical journal* **2007**, *93*, 3169–81.

(79) Ruben, G. C. *Micron (Oxford, England : 1993)* **1998**, *29*, 359–96.

(80) Sanii, B.; Smith, A. M.; Butti, R.; Brozell, A. M.; Parikh, A. N. **2008**, 1–11.

(81) Ge, K.; Minhas, F.; Duhadaway, J.; Mao, N. C.; Wilson, D.; Buccafusca, R.; Sakamuro, D.; Nelson, P.; Malkowicz, S. B.; Tomaszewski, J.; Prendergast, G. C. *International Journal of Cancer* **2000**, *86*, 155–161.

(82) Hatzakis, N. S.; Bhatia, V. K.; Larsen, J.; Madsen, K. L.; Bolinger, P. Y.; Kunding, A. H.; Castillo, J.; Gether, U.; Hedegard, P.; Stamou, D. *Nature Chemical Biology* **2009**, *5*, 835–841.

(83) Chinnapen, D. J. F.; Chinnapen, H.; Saslowsky, D.; Lencer, W. I. *Fems Microbiology Letters* **2007**, *266*, 129–137.

(84) Wang, R.; Shi, J.; Parikh, A. N.; Shreve, A. P.; Chen, L. H.; Swanson, B. I. *Colloids and Surfaces B-Biointerfaces* **2004**, *33*, 45–51.

(85) Stahelin, R. V; Long, F.; Peter, B. J.; Murray, D.; De Camilli, P.; McMahon, H. T.; Cho, W. *The Journal of biological chemistry* **2003**, *278*, 28993–9.

(86) Veatch, S. L.; Keller, S. L. *Biophysical Journal* **2003**, *85*, 3074–3083.

(87) Hsieh, W.-T.; Baumgart, T. *Biophysical Journal* **2012**, *102*, 97a–98a.

(88) Toshev, B. V *Current Opinion in Colloid & Interface Science* **2008**, *13*, 100–106.

(89) Tarazona, P.; Navascues, G. *Journal of Chemical Physics* **1981**, *75*, 3114–3120.

(90) Koga, K.; Widom, B. *The Journal of chemical physics* **2007**, *127*, 064704.

(91) Schimmele, L.; Napiorkowski, M.; Dietrich, S. *Journal of Chemical Physics* **2007**, *127*, 28.

(92) Rowlinson, J. S.; Widom, B. *Molecular theory of capillarity*; Clarendon Press: Oxford, Oxfordshire, 1982; p. xi, 327 p.

(93) Vandecan, Y.; Indekeu, J. O. *Journal of Chemical Physics* **2008**, *128*, 5.

(94) Roberts, M. J.; Teer, E. J.; Duran, R. S. *Journal of Physical Chemistry B* **1997**, *101*, 699–701.

(95) Trabelsi, S.; Zhang, S.; Lee, T. R.; Schwartz, D. K. *Physical Review Letters* **2008**, *100*.

(96) Trabelsi, S.; Zhang, Z.; Zhang, S.; Lee, T. R.; Schwartz, D. K. *Langmuir* **2009**, *25*, 8056–8061.

(97) Mann, E. K.; Henon, S.; Langevin, D.; Meunier, J. *Journal De Physique Ii* **1992**, *2*, 1683–1704.

(98) Muller, P.; Gallet, F. *Physical Review Letters* **1991**, *67*, 1106–1109.

(99) Benvegnu, D. J.; McConnell, H. M. *Journal of Physical Chemistry* **1992**, *96*, 6820–6824.

(100) Benvegnu, D. J.; McConnell, H. M. *Journal of Physical Chemistry* **1993**, *97*, 6686–6691.

(101) Stottrup, B. L.; Heussler, A. M.; Bibelnieks, T. A. *Journal of Physical Chemistry B* **2007**, *111*, 11091–11094.

(102) Honerkamp-Smith, A. R.; Cicuta, P.; Collins, M. D.; Veatch, S. L.; Den Nijs, M.; Schick, M.; Keller, S. L. *Biophysical journal* **2008**, *95*, 236–46.

(103) Tian, A. W.; Johnson, C.; Wang, W.; Baumgart, T. *Physical Review Letters* **2007**, *98*.

(104) Veatch, S. L.; Cicuta, P.; Sengupta, P.; Honerkamp-Smith, A.; Holowka, D.; Baird, B. *ACS chemical biology* **2008**, *3*, 287–93.

(105) Puech, P. H.; Borghi, N.; Karatekin, E.; Brochard-Wyart, F. *Physical Review Letters* **2003**, *90*, 4.

(106) Mann, E. K.; Henon, S.; Langevin, D.; Meunier, J.; Leger, L. *Physical Review E* **1995**, *51*, 5708–5720.

(107) Hu, Y. F.; Meleson, K.; Israelachvili, J. *Biophysical Journal* **2006**, *91*, 444–453.

(108) Blanchette, C. D.; Lin, W. C.; Orme, C. A.; Ratto, T. V; Longo, M. L. *Langmuir* **2007**, *23*, 5875–5877.

(109) Baumgart, T.; Hess, S. T.; Webb, W. W. *Nature* **2003**, *425*, 821–824.

(110) Steffen, P.; Wurlitzer, S.; Fischer, T. M. *The Journal of Physical Chemistry A* **2001**, *105*, 8281–8283.

(111) Kuzmin, P. I.; Akimov, S. A.; Chizmadzhev, Y. A.; Zimmerberg, J.; Cohen, F. S. *Biophysical Journal* **2005**, *88*, 1120–1133.

(112) Akimov, S. A.; Kuzmin, P. I.; Zimmerberg, J.; Cohen, F. S. *Physical Review E* **2007**, *75*.

(113) Brewster, R.; Pincus, P. A.; Safran, S. A. *Biophysical Journal* **2009**, *97*, 1087–1094.

(114) Alexander, J. C.; Bernoff, A. J.; Mann, E. K.; Mann, J. A.; Wintersmith, J. R.; Zou, L. *Journal of Fluid Mechanics* **2007**, *571*, 191.

(115) Baumgart, T.; Das, S.; Webb, W. W.; Jenkins, J. T. *Biophysical Journal* **2005**, *89*, 1067–1080.

(116) Seul, M.; Sammon, M. J. *Physical Review Letters* **1990**, *64*, 1903–1906.

(117) Helrich, C. S.; Schmucker, J. A.; Woodbury, D. J. *Biophysical Journal* **2006**, *91*, 1116–1127.

(118) Brewster, R.; Safran, S. a *Biophysical journal* **2010**, *98*, L21–3.

(119) Akimov, S. A.; Kuzmin, P. I.; Zimmerberg, J.; Cohen, F. S.; Chizmadzhev, Y. A. *Journal of Electroanalytical Chemistry* **2004**, *564*, 13–18.

(120) Idema, T.; Van Leeuwen, J. M. J.; Storm, C. *Physical Review E* **2009**, *80*, 9.

(121) West, B.; Brown, F. L. H.; Schmid, F. *Biophysical Journal* **2009**, *96*, 101–115.

(122) Putzel, G. G.; Schick, M. *Biophysical Journal* **2008**, *95*, 4756–4762.

(123) Fournier, J. B. *European Physical Journal B* **1999**, *11*, 261–272.

(124) Lawrence, J. C.; Saslowsky, D. E.; Edwardson, J. M.; Henderson, R. M. *Biophysical Journal* **2003**, *84*, 1827–1832.

(125) Yuan, C. B.; Furlong, J.; Burgos, P.; Johnston, L. J. *Biophysical Journal* **2002**, *82*, 2526–2535.

(126) Gandhavadi, M.; Allende, D.; Vidal, A.; Simon, S. A.; McIntosh, T. J. *Biophysical Journal* **2002**, *82*, 1469–1482.

(127) Akimov, S. A.; Hlaponin, E. A.; Bashkirov, P. V; Boldyrev, I. A.; Mikhalyov II; Telford, W. G.; Molotkovskaya, I. M. *Biologicheskie Membrany* **2009**, *26*, 234–239.

(128) Bloom, M.; Evans, E.; Mouritsen, O. G. *Quarterly Reviews of Biophysics* **1991**, *24*, 293–397.

(129) Fattal, D. R.; Benshaul, A. *Biophysical Journal* **1993**, *65*, 1795–1809.

(130) Helfrich, W. *Zeitschrift Fur Naturforschung C-a Journal of Biosciences* **1973**, *C 28*, 693–703.

(131) McConnell, H. M. *Annual Review of Physical Chemistry* **1991**, *42*, 171–195.

(132) McConnell, H. M. *Journal of Physical Chemistry* **1990**, *94*, 4728–4731.

(133) Stone, H. A.; McConnell, H. M. *Proceedings of the Royal Society of London Series a-Mathematical and Physical Sciences* **1995**, *448*, 97–111.

(134) Veatch, S. L.; Gawrisch, K.; Keller, S. L. *Biophysical Journal* **2006**, *90*, 4428–4436.

(135) Ayuyan, A. G.; Cohen, F. S. *Biophysical journal* **2006**, *91*, 2172–83.

(136) Garcia-Saez, A. J.; Chiantia, S.; Salgado, J.; Schwille, P. *Biophysical Journal* **2007**, *93*, 103–112.

(137) Nicolini, C.; Baranski, J.; Schlummer, S.; Palomo, J.; Lumbierres-Burgues, M.; Kahms, M.; Kuhlmann, J.; Sanchez, S.; Gratton, E.; Waldmann, H.; Winter, R. *Journal of the American Chemical Society* **2006**, *128*, 192–201.

(138) Schäfer, L. V; Marrink, S. J. *Biophysical journal* **2010**, *99*, L91–3.

(139) Panda, A. K.; Nag, K.; Harbottle, R. R.; Possmayer, F.; Petersen, N. O. *Journal of Colloid and Interface Science* **2007**, *311*, 551–555.

(140) Illya, G.; Deserno, M. *Biophysical Journal* **2008**, *95*, 4163–4173.

(141) Reisenberg, M.; Singh, P. K.; Williams, G.; Doherty, P. *Philosophical transactions of the Royal Society of London. Series B, Biological sciences* **2012**, *367*, 3264–75.

(142) Veatch, S. L.; Leung, S. S. W.; Hancock, R. E. W.; Thewalt, J. L. *The journal of physical chemistry. B* **2007**, *111*, 502–4.

(143) Bernardini, C.; Stoyanov, S. D.; Cohen Stuart, M. A.; Arnaudov, L. N.; Leermakers, F. A. M. *Langmuir* **2011**, *27*, 2501–2508.

(144) Liao, Z. Z.; Lampe, J. W.; Ayyaswamy, P. S.; Eckmann, D. M.; Dmochowski, I. J. *Langmuir* **2011**, *27*, 12775–12781.

(145) Hillborg, H.; Gedde, U. W. *Ieee Transactions on Dielectrics and Electrical Insulation* **1999**, *6*, 703–717.

(146) Kaali, P.; Momcilovic, D.; Markström, A.; Aune, R.; Czel, G.; Karlsson, S. *Journal of Applied Polymer Science* **2010**, *115*, 802–810.

(147) Mann, E. K.; Langevin, D. *Langmuir* **1991**, *7*, 1112–1117.

(148) Lenk, T. J.; Lee, D. H. T.; Koberstein, J. T. *Langmuir* **1994**, *10*, 1857–1864.

(149) Mehta, S. C.; Somasundaran, P.; Maldarelli, C.; Kulkarni, R. *Langmuir* **2006**, *22*, 9566–9571.

(150) Kim, C.; Gurau, M. C.; Cremer, P. S.; Yu, H. *Langmuir* **2008**, *24*, 10155–10160.

(151) Hahn, T. D.; Hsu, S. L.; Stidham, H. D. *Macromolecules* **1997**, *30*, 87–92.

(152) Damaschun, G. *Kolloid-Zeitschrift and Zeitschrift Fur Polymere* **1962**, *180*, 65–&.

(153) Schilling, F. C.; Gomez, M. A.; Tonelli, A. E. *Macromolecules* **1991**, *24*, 6552–6553.

(154) Lee, L. T.; Mann, E. K.; Langevin, D.; Farnoux, B. *Langmuir* **1991**, *7*, 3076–3080.

(155) Karolin, J.; Johansson, L. B. A.; Strandberg, L.; Ny, T. *Journal of the American Chemical Society* **1994**, *116*, 7801–7806.

(156) Ludwig, D. B.; Trotter, J. T.; Gabrielson, J. P.; Carpenter, J. F.; Randolph, T. W. *Analytical Biochemistry* **2011**, *410*, 191–199.

(157) Mann, E. K.; Lee, L. T.; Henon, S.; Langevin, D.; Meunier, J. *Macromolecules* **1993**, *26*, 7037–7045.

(158) Patel, A. J.; Varilly, P.; Jamadagni, S. N.; Acharya, H.; Garde, S.; Chandler, D. *Proceedings of the National Academy of Sciences of the United States of America* **2011**, *108*, 17678–17683.

(159) Zema, J.; Rysz, J.; Budkowski, A.; Awsiuk, K. *Soft Matter* **2012**, *8*, 5550–5560.

(160) Von Heimendahl, M. *Micron (1969)* **1972**, *4*, 111–116.

(161) Mann, E.; Hénon, S.; Langevin, D.; Meunier, J.; Léger, L. *Physical review. E, Statistical physics, plasmas, fluids, and related interdisciplinary topics* **1995**, *51*, 5708–5720.

(162) Camley, B. a; Esposito, C.; Baumgart, T.; Brown, F. L. H. *Biophysical journal* **2010**, *99*, L44–6.

(163) Lingwood, D.; Simons, K. *Science* **2010**, *327*, 46–50.

(164) Lingwood, D.; Ries, J.; Schwille, P.; Simons, K. *Proceedings of the National Academy of Sciences of the United States of America* **2008**, *105*, 10005–10.

(165) Li, S. S. C. *Biochemical Journal* **2005**, *390*, 641–653.

(166) Zarrinpar, A.; Bhattacharyya, R. P.; Lim, W. A. *Sci. STKE* **2003**, *2003*, re8–.

(167) Li, P. L.; Banjade, S.; Cheng, H. C.; Kim, S.; Chen, B.; Guo, L.; Llaguno, M.; Hollingsworth, J. V; King, D. S.; Banani, S. F.; Russo, P. S.; Jiang, Q. X.; Nixon, B. T.; Rosen, M. K. *Nature* **2012**, *483*, 336–U129.